FERROELECTRIC NANOCOMPOSITE AND POLAR HYBRID SOL-GEL MATERIALS FOR EFFICIENT, HIGH ENERGY DENSITY CAPACITORS

A Dissertation
Presented to
The Academic Faculty

by

Yunsang Kim

In Partial Fulfillment
of the Requirements for the Degree
Doctor of Philosophy in the
School of Materials Science and Engineering

Georgia Institute of Technology
May 2014

FERROELECTRIC NANOCOMPOSITE AND POLAR HYBRID SOL-GEL MATERIALS FOR EFFICIENT, HIGH ENERGY DENSITY CAPACITORS

Approved by:

Dr. Joseph W. Perry, Advisor
School of Chemistry and Biochemistry
Georgia Institute of Technology

Dr. Rosario Gerhardt
School of Materials Science and Engineering
Georgia Institute of Technology

Dr. Anselm C. Griffin, Co-Advisor
School of Materials Science and Engineering
Georgia Institute of Technology

Dr. Zhiqun Lin
School of Materials Science and Engineering
Georgia Institute of Technology

Dr. Bernard Kippelen
School of Electrical and Computer Engineering
Georgia Institute of Technology

Date Approved: March 26, 2014.

ACKNOWLEDGEMENTS

I would like to express my deepest appreciation to everyone who has supported and helped me in one way or another during the course of my PhD study. First of all, I want to thank my advisor Prof. Perry for accepting, supporting, encouraging, and guiding me in every possible way. I am highly indebted to our capacitor subgroup members, John Tillotson, Dr. Mohanalingam Kathaperumal and Dr. O'Neil Smith for useful training and constructive discussions and suggestions. The Perry group has always been welcoming and warm to me, and I would really like to thank all of the current and past members for making me feel a part of Perry group.

I am grateful to many collaborators from different departments, including Dr. Sergio Paniagua, Dr. Canek Fuentes-Hernandez, Dr. Do Kyung Hwang, Dr. Jae Won Shim, Dr. Ye Cai, Amir Dindar, and Siyuan Zhang for their technical support and useful discussions. I also appreciate my committee members for their valuable time and comments, especially Dr. Kippelen for his generous permission to use electrical instrumentations. I thank the Center for Organic Photonics and Electronics (COPE) for the fellowship granted.

I want to emphasize my sincere gratitude to Dr. Ming-Jen Pan in Naval Research Laboratory for his help in many critical measurements. My PhD study would not possibly be brought into closure without his support.

Finally, I want to thank my families in Korea for their endless support and encouragement throughout my study. My girlfriend Yunjeong has helped me all along, and I feel really fortunate to have her by my side. None of this would be possible without their love.

TABLE OF CONTENTS

LIST OF TABLES AND SCHEME

LIST OF FIGURES

LIST OF SYMBOLS

ε_o	vacuum permittivity
ε_r	relative permittivity
ε_{eff}	effective permittivity
τ	time constant
χ	electric susceptibility
ϕ_B	the height of potential barrier under zero electric field
$\bar{\varphi}$	mean barrier height
Ψ	the profile of potential energy barrier
d	thickness
h	Planck's constant
k	permittivity
t	time
A	area
C	capacitance
D	displacement
E	electric field
I	current
J	current density
P	polarization
P	power
Q or q	electric charge
R	electrical resistance

T	temperature
U	total energy
V	potential difference
W	work
E_B	breakdown strength
E_{BD}	characteristic breakdown strength
J_c	conduction current
J_d	displacement current
P_F	cumulative failure probability distribution
T_c	Curie temperature
V_{rms}	root mean square of time-varying voltage
$f(E)$	Fermi-Dirac distribution function
$<E_B>$	average breakdown strength
U_{max}	maximum extractable energy density
U_{max}^{CD}	U_{max} from C-D method
U_{max}^{PE}	U_{max} from P-E method

LIST OF ABBREVIATIONS

3-D	three dimensional
% CDF	cumulative probability of failure
AFM	atomic force microscopy
Al	aluminum
I-V	current-voltage
ALD	atomic layer deposition
BSt	butylstyrene
BST	barium strontium titanate
BT	barium titanate
C-D	charge-discharge
CNEMDMS	2-cyanoethylmethyldimethoxysilane
CNETMS	2-cyanoethyltrimethoxysilane
CNPTES	3-cyanopropyltriethoxysilane
DC	direct current
FE-SEM	field-emission scanning electron microscope
FT-IR	Fourier transform infrared
ITO	indium tin oxide
J-E	current density-electric field
MIM	metal-insulator-metal
MMT	montmorillonite
MeoEtOH	2-methoxyethanol
MeOH	methanol
P-E	polarization-electric field

PFBPA	pentafluorobenzyl phosphonic acid
PAN	polyacrylonitrile
P(AN-*co*-AL)	poly(acrylonitrile-allylcyanide)
PMMA	poly(methyl methacrylate)
PP	polypropylene
PPO	poly(*p*-phenylene oxide)
PPS	polyphenylene sulfide
PS	polystyrene
PVB	polyvinyl butyral
PVDF	poly(vinylidene fluoride)
P(VDF-co-TrFE)	poly(vinylidene fluoride-*co*-trifluoroethylene)
P(VDF-*co*-CTFE)	poly(vinylidene fluoride-*co*-chlorotrifluoroethylene)
P(VDF-*co*-HFP)	poly(vinylidene fluoride-*co*-hexafluoropropylene)
P(VDF-*co*-TrFE-*co*-CTFE)	poly(vinylidene fluoride-*co*-trifluoroethylene-*co*-chlorotrifluoroethylene)
x-PP	crosslinked polypropylene
PZT	lead zirconate titanate
RC	resistor-capacitor
RMS	room mean square
TEM	transmission electron microscopy
TEOS	tetraethyl orthosilicate
TGA	Thermogravimetric analysis
XRD	x-ray diffraction

SUMMARY

The development of efficient, high-performance materials for electrical energy storage and conversion applications has become a must to meet an ever-increasing need for electrical energy. Among devices developed for this purpose, capacitors have been used for pulsed power applications that require large power density with millisecond-scale charge and discharge. However, conventional polymeric films, which possess high breakdown strength, are limited due to low permittivity and hence compromise the energy storage capability of capacitors. In order to develop high energy density dielectric materials for pulsed power applications, two hurdles must be overcome: 1) the appropriate selection of materials that possess not only large permittivity but also high breakdown strength, 2) the optimization of material processing to improve morphology of dielectric films to minimize loss during energy extraction process.

This thesis will present the development of novel dielectric material, with emphasis on the optimization of material and thin film processing toward improved morphology as ways to achieve high energy density at the material level. After first two chapters of introduction and experimental details, Chapter 3 will demonstrate the improvement of nanocomposite morphology *via* processing optimization and study its effect on the energy storage characteristics of nanocomposites thereof. Chapter 4 will investigate dielectric sol-gel materials containing dipolar cyano side groups, which are relatively a new class of material for pulsed power applications. Finally, Chapter 5 will discuss the effect of tunneling barrier layer on sol-gel films to mitigate charge carrier injection and associated conduction and breakdown phenomena, which would be significantly detrimental to the energy storage performance of dielectric sol-gel films.

CHAPTER 1

INTRODUCTION & LITERATURE SURVEY

1.1 Physics of Dielectric Materials

1.1.1 Theory of dielectric polarization and relaxation

The definition of dielectric is a nonconductor of direct electric current. The word dielectric consists of a prefix *dia* and *electric*. The prefix *dia* originated from Greek, meaning "through" or "across". Therefore, a dielectric refers to a material that permits the passage of electric field or flux. This also implies that a dielectric does not permit the passage of particles including electrons, meaning that it should not conduct an electric current. However, since there is no perfect material, a real dielectric material permits the passage of electrons and electric current to a certain level.

When dielectric materials are placed in an electric field, instead of permitting the flow of electric charges, they undergo dielectric and/or electric polarization, which refers to a phenomenon arising from the relative displacement of negative and positive charge carriers. Dielectric polarization can result from the orientation of existing dipoles toward the direction of an applied electric field or *via* the separation of mobile charge carriers at the interface between a dielectric material and an electrode surface. This phenomenon can also be considered as the redistribution of charges in a dielectric material in response to an external electric field.

The dielectric polarization is described by four mechanisms depending on the origin of polarization, which has different response times: electronic polarization, atomic or ionic polarization, orientational or rotational polarization, and interfacial or space charge polarization, which is particularly associated with mobile and trapped charges.

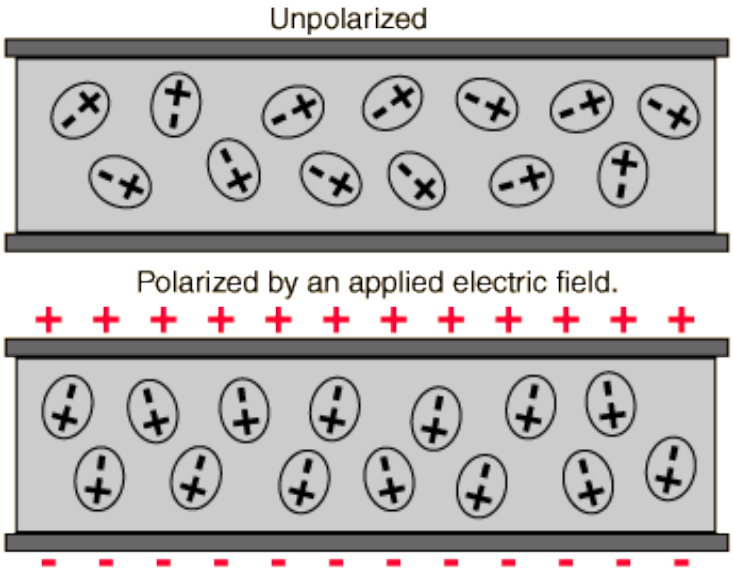

Figure 1.1 A dielectric medium showing orientation of charged particles creating polarization effects. Such a medium can have a higher ratio of electric flux to charge (permittivity) than empty space.

Electronic polarization refers to the polarization caused by the deformation or the translation of the originally neutral electron clouds of atoms or molecules by external electric field. This polarization is not permanent and is dissipated once an applied electric field is removed. Atomic or ionic polarization is related to the displacement of atoms or ions relative to each other under the influence of an electric field. This displacement leads to the separation of charges, resulting in the polarization. Orientational or rotational polarization occurs only in materials with dipolar molecules or particles possessing permanent dipole moment. Under the application of electric field, dipoles tend to reorient or rotate toward the direction of field in such a way that net dipole moment is generated. However, once the external field is removed, the net dipole moment would return to zero because thermal agitation tends to randomize oriented dipoles. This so called relaxation phenomenon is one of the important characteristics of dipolar molecules.

Both electronic and atomic polarizations are associated with elastic displacement of

electron clouds and lattice vibration within atoms or molecules. In contrast, orientational polarization is related to a rotational process, which brings about mechanical friction, so that it involves inelastic movement of molecules or particles. Therefore, orientational polarization has a relaxation process.

Interfacial or space charge polarization is associated with the migration of charge carriers (ions, holes or electrons) either injected from electrical contacts or formed at the interfaces in which materials brought together have different charge transport properties. Those trapped and accumulated charges distort the distribution of electric field, thereby affecting relative permittivity and breakdown strength of a material. Interfacial or space charge polarization becomes prominent at high fields in which the concentration of charge carrier in dielectric materials becomes high due to strong carrier injection. Additionally, interfacial or space charge polarization is important in heterogeneous or multiphase systems containing macro and microscopic junctions such as ceramic/polymer nanocomposites, multi-layered structure, and porous materials.

Aforementioned four types of dielectric polarization can be grouped into two major regimes: resonance and relaxation regime. Resonance regime refers to electronic and atomic or ionic polarizations, which are associated with vibrations of electrons, atoms or ions, respectively. In these polarizations associated with vibration a resonance will occur when the frequency of the excitation field is close to the natural frequency of the vibration of oscillation system. Relaxation regime is related to orientational/rotational and interfacial or space charge polarizations, which involve the movements of charges either by orientation/rotation or through the migration of charge carriers, respectively. A relaxation phenomenon occurs during a polarization or a depolarization process because the movement of charge carriers requires the time, which is quite long compared to the time scale in the vibration of electrons and atoms, to overcome the friction arising from a surrounding medium.

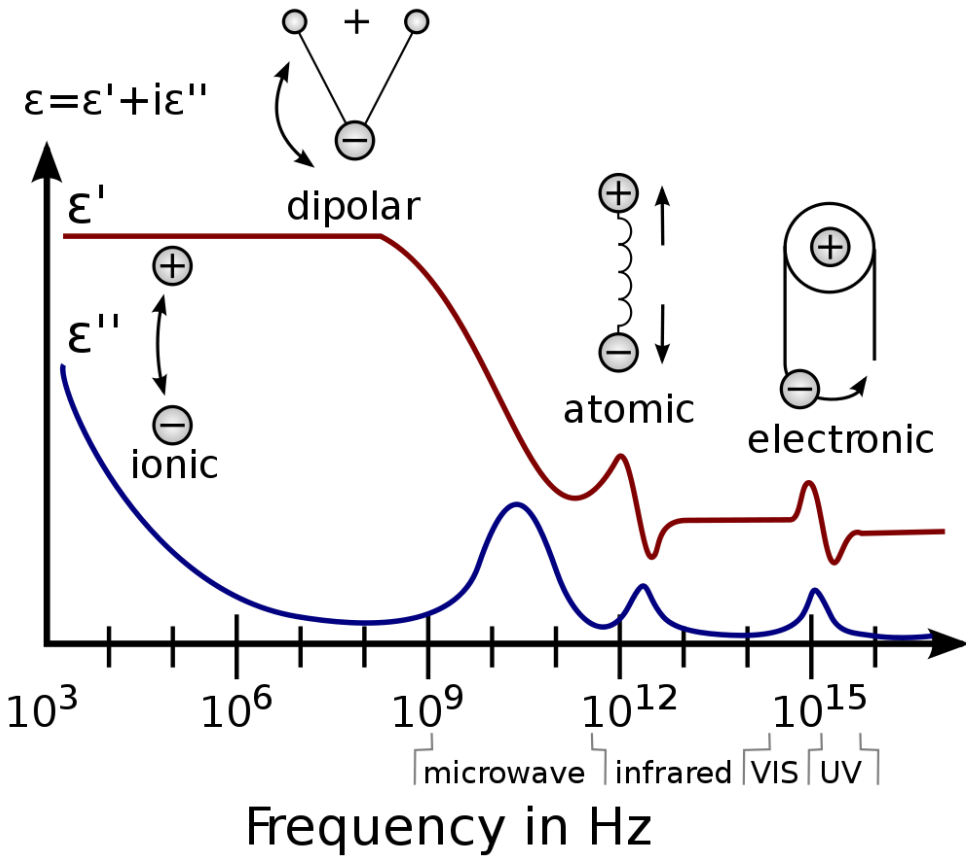

Figure 1.2 An illustration of the frequency response of various dielectric polarization mechanisms in terms of the real and imaginary parts of the permittivity. (copyright Prof. Kenneth A. Mauritz, Univ. Southern Mississippi)

We can consider dipolar molecules in a material as ellipsoidal-shaped balls with a positive charge on one end and a negative charge of the same magnitude on the other end in a viscous fluid. In this manner, it can be imagined that the orientation of dipolar molecules under the application of electric field involves the energy required to overcome the resistance of surrounding molecules, so the reorientation process is strongly temperature dependent. In other words, dielectric spectroscopy, which is either in time or frequency domain, can provide better understanding of the relaxation processes in dipolar molecules when measurements are performed with varying temperature.

For materials containing dipolar molecules, under high applied field there should be the

case in which all individual molecules are largely oriented, so that there can be little room for the further orientation of dipolar or nondipolar molecules when the field is further increased. This phenomenon is called as dielectric saturation, which is evidenced by the decrease in relative permittivity of materials as electric field increases.

In addition to the field induced polarization mechanisms, spontaneous polarization occurs in ferroelectric materials whose crystal structure exhibits electrical order without the help of an external electric field. It should be noted that unlike the four dielectric polarization mechanisms discussed above, spontaneous polarization does not require external electric field. It is believed that the driving force of spontaneous process is a thermodynamic free energy that leads the system into a lower energy state, which is thermodynamically stable.

$BaTiO_3$ is a typical example of such crystals, which undergo phase transition at Curie temperature, T_c. At $T > T_c$, $BaTiO_3$ exhibits a cubic structure in which the centers of negative and positive ions coincide, thereby leading the crystal to form a negligible net dipole moment. In contrast, at $T < T_c$ the movement of positive ions (Ba^{2+} and Ti^{4+}) to off-center positions converts the structure of the crystal from cubic to tetragonal. This distorted structure is enough for positive and negative ions to be separated, thereby resulting in an electric dipole moment. Each unit cell of the crystal holds a reversible dipole moment, which is spontaneously aligned parallel to the direction of the dipole moments of neighboring unit cells, thereby creating a net dipole moment.

Ferroelectricity is a property of certain materials that possess, over some range of temperature, a spontaneous electric polarization that can be reversed or reoriented by the application of external electric field. Among 32 classes of crystals based on the degree of symmetry, only ten noncentrosymmetric crystals exhibit spontaneous electrical polarization, that is, they have a permanent dipole moment per unit volume in the

direction of polar axis.

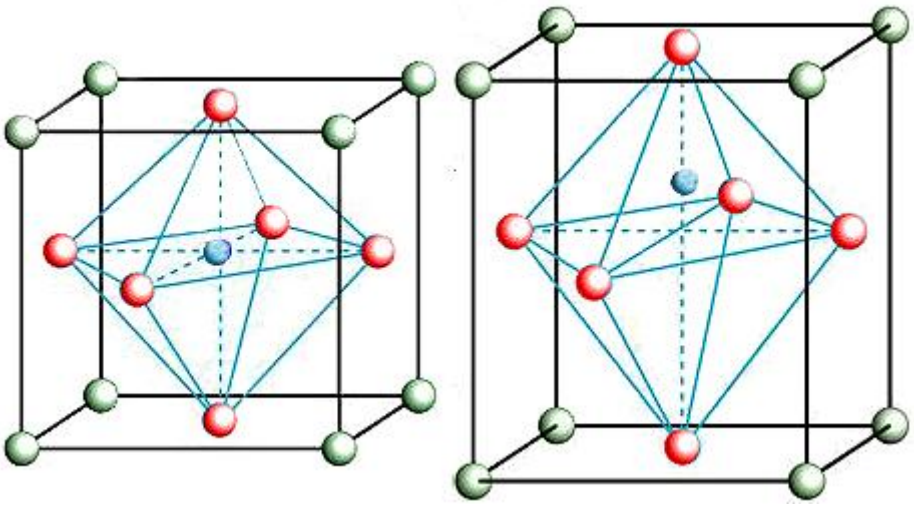

Figure 1.3 The structure of (left) cubic and (right) tetragonal $BaTiO_3$. The red spheres represent oxygen centers, green Ti^{4+} cations, and blue Ba^{2+}, respectively. The off-center position of Ba^{2+} ions are shown in tetragonal structure. (copyright Army High Performance Computing Research Center (AHPCRC), Stanford University)

Because of the requirement of nonvanishing dipole moments in ferroelectricity, most of ferroelectric materials are ceramics, which typically are polycrystalline materials comprising ferroelectric crystallites. However, such net dipole moments also exist in some semicrystalline polymers such as poly(vinylidene fluoride) [PVDF] and its copolymers, odd-numbered nylons, aromatic polyurea, and cyanopolymers.[1] Lovinger categorized structural requirements for macromolecules to possess ferroelectricity[2]: a permanent dipole moment in monomeric unit, configuration, conformation, morphology and packing of polymeric chains or crystallites in such a manner that individual dipole moment is not compensated. It should be noted that only the structural requirement associated with a monomeric unit is intrinsic and others are extrinsic properties. Therefore, ferroelectric response in polymers can be controlled by varying processing conditions such as film casting method, electrical poling, and mechanical orientation. This processing-dependent ferroelectric property of semicrystalline polymers will be

discussed in detail in section 1.3. More details for dielectric materials can be found in these references.[3-5]

1.1.2 Theory of dielectric breakdown

Dielectric breakdown is one category of failure phenomena in materials. It generally refers to an abrupt failure of an insulator to restrict the flow of a current, accompanied by a rapid reduction in the resistivity of an insulator. This electric failure occurs when the voltage applied across an insulator exceeds the electrical breakdown strength of a material. Dielectric breakdown results in a portion of an insulator becoming electrically conductive, which often leads to the failure in an electronic circuit in the form of a short circuit or a blown fuse. It is worthwhile to note that the breakdown strength of a material cannot be determined by a definitive value because there should be a statistical probability whether or not a material would fail at a given applied field. Although this thesis primarily deals with dielectric solids, it is worth reviewing briefly the mechanisms of electrical breakdown in gases because of the similarities in the breakdown processes of both gases and solids.

The typical current-voltage (I-V) relationship of gases is shown in Figure 1.4. Region 1 shows the current produced by free ions and/or charge carriers that are already present in gases. A region 2 of current saturation follows in which the current reaches a constant showing a plateau and all charge carriers produced are collected at metal electrodes. Region 3 represents a current rise in which the increase in an electrical current is due to a carrier multiplication process associated with impact ionization of charge carriers. I-V curve arrives in region 4 when a sufficiently high electric field is applied across the gap of gases. In this region, the multiplication of charge carriers in the gaseous medium makes a transition from non-self-sustaining to self-sustaining type, accompanied by the

rapid increase of current and usually a spark, a noise, and even a light emission. In order for electrical breakdown to occur, there must be a mechanism for producing enough ionization to amplify the multiplication process of charge carriers, not only offsetting the loss by diffusion and drift in the space between electrodes but also leading to self-sustainable carrier multiplication process.

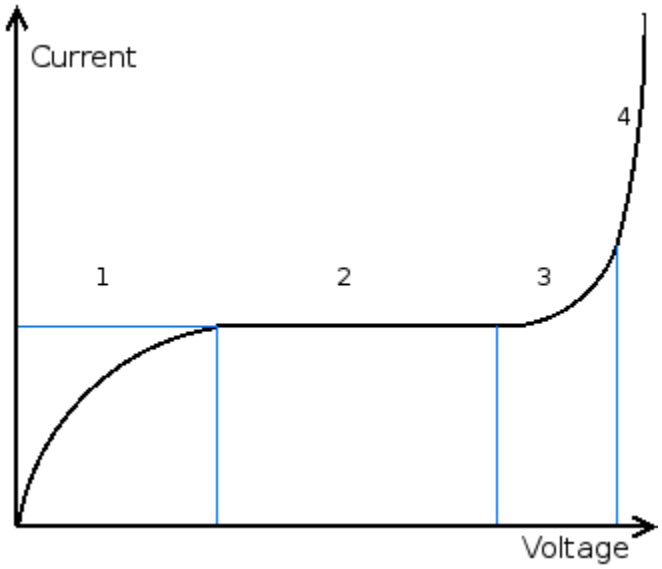

Figure 1.4 Typical current-voltage (I-V) characteristics of gases between two parallel metallic electrodes before breakdown.

Electrical breakdown in gases involves the injection of electrons from a cathode as a primary process. Subsequently, it is imagined that positive charge carriers are knocked out from an anode and local heating of the electrodes occurs, producing clumps of metal vapor during which impact ionization may take place. The combination of these interactions continuously enhances a carrier multiplication, until a destructive self-sustaining discharge and the final breakdown occur.

The primary difference between gases and solids in regard to the mechanism of dielectric breakdown is the mean free path of charge carriers, electrons. Compared to the value in gases, a mean free path of dielectric solid is extremely small, ranging in the order of several molecular radii (5-20 Å)[6]. Considering the requirement for a self-sustaining

carrier multiplication process for breakdown, which needs enough ionization to amplify a multiplication process, there should be another process that could extend intrinsic mean free path of charge carriers in dielectric solids.

Dielectric breakdown mechanisms in solids can largely be categorized into thermal and electrical breakdowns. The difference between two mechanisms is that a carrier multiplication is whether due to a mutual feedback between joule heating and thermal excitation or due to a pure electronic process other than thermal excitation. It is believed that the initial stage of breakdown process might be the combination of two processes, but ultimately the final destructive breakdown is due to thermal instability in a material.

Thermal breakdown refers to the breakdown caused by joule heating, which could not be removed fast enough by thermal conduction or convection, continuously generated primarily from electrical conduction and polarization. The mutual feedback of accumulated heat inside a material leads to thermal instability that brings about the destructive breakdown of a material.

Electrical breakdown theory includes intrinsic, Zener, Avalanche, and hot carrier breakdown mechanisms.[7, 8] From these relatively old theories, combining some important concepts such as impact ionization, hot carriers, and the formation of low-density phase, Kao has proposed a compromised theory of electrical breakdown in condensed insulators that involves the creation of low-density domains or channels initiated by carrier injection from electrical contacts.[9] Subsequently, by dissociative trapping, detrapping, and recombination of injected carriers, the low-density regions grow, so that the extended mean free path of injected carriers would cause impact ionizations in these regions. Then the carrier multiplication process leads to the further extension of low-density domains or channels, and finally results in the destructive breakdown of a material.

Based on proposed breakdown processes and mechanisms, it is believed that the following remedies are necessary to mitigate electrical breakdown of dielectric solids. 1) suppression of charge injection from electrical contacts, 2) minimization of low-density regions in dielectric materials, and 3) reduction of charge carriers inside dielectric materials before the application of electric field.

In the following chapters, this thesis shall present the effects of the abovementioned approaches on the breakdown strength and, furthermore, the energy storage performance of dielectric materials.

1.2 Basics of Energy Storage in Dielectric Film Capacitor

In a capacitor of capacitance *C*, holding a charge $+q$ on one plate and $-q$ on the other plate, the work needed to move a small element of charge dq from one plate to the other against the potential difference V is defined as dW.

$$dW = Vdq = \frac{Q}{C}dq \qquad \text{Equation 1.1}$$

Since work done to a system is equivalent to the energy stored in a system,

$$U_{stored} \equiv W = \int_0^Q \frac{q}{C}dq = \frac{1}{2}\frac{Q^2}{C} = \frac{1}{2}QV = \frac{1}{2}CV^2 \qquad \text{Equation 1.2}$$

Capacitance can be determined if the geometry of conductors and the dielectric property of an insulator between conductors, metal plates, are known.

$$C = \varepsilon_o \varepsilon_r \frac{A}{d} \qquad \text{Equation 1.3}$$

where A and d are area and thickness of device; ε_o and ε_r are vacuum and relative permittivities, respectively.

By combining Equation 1.2 and 1.3, we can determine the energy stored in a capacitor with known geometry of conductors.

$$U_{stored} = \frac{1}{2}CV^2 = \frac{1}{2}\varepsilon_o\varepsilon_r\frac{A}{d}V^2 \qquad \text{Equation 1.4}$$

$$Energy\ density, \frac{U_{stored}}{volume} = \frac{1}{2}\varepsilon_o\varepsilon_r\frac{V^2}{d^2} = \frac{1}{2}\varepsilon_o\varepsilon_r {E_B}^2 \qquad \text{Equation 1.5}$$

where E_B is the breakdown strength of dielectric material between metal plates. As shown in Equation 1.5, which is the theoretical energy density in a capacitor, the energy density of a capacitor is proportional to relative permittivity of a dielectric material and, more importantly, scales with the square of breakdown strength of a dielectric material. It is important to note that permittivity of a dielectric material becomes nonlinear when the applied electric field exceeds a certain value (usually above 100 V/μm). Therefore, Equation 1.5 is only valid in a small electric field regime, and to determine the energy density of a capacitor at high electric field, other techniques such as charge-discharge (C-D) and electric field dependent polarization (P-E) measurements are required, which will be discussed in Chapter 2.

In case of fluctuating voltage *V(t)*, the stored energy also fluctuates and hence power must flow into or out of a capacitor. The power, *P*, can be found by taking the time derivative of the stored energy in or work done to a system

$$P = \frac{dW}{dt} = \frac{d}{dt}\left(\frac{1}{2}CV^2\right) = CV(t)\frac{dV}{dt} \qquad \text{Equation 1.6}$$

Since,

$$I(t) = \frac{dQ(t)}{dt} = C\frac{dV}{dt} \qquad \text{Equation 1.7}$$

By combining Equations 1.6 and 1.7, we can obtain

$$\frac{dW}{dt} = CV(t)\frac{dV}{dt} = V(t)I(t) = I^2(t)R(t) \qquad \text{Equation 1.8}$$

Equation 1.8 is valid in case of resistive loads. Therefore, the energy stored in a capacitor is obtained by integrating Equation 1.8 with respect to time,

$$U_{stored} \equiv W = \int_0^t I^2(t)R(t)\,dt = \frac{1}{R}\int_0^t V^2(t)\,dt \qquad \text{Equation 1.9}$$

Extractable energy density of a capacitor is determined by using Equation 1.9 in RC circuit (capacitor and resistor in series) with series of resistors whose resistivity are already known.

In an RC circuit, a capacitor will discharge its stored energy through a resistor. The voltage across a capacitor, which is time dependent, can be found by using Kirchhoff's current law, where the current through a capacitor must be equal to the current through a resistor.

$$C\frac{dV}{dt} + \frac{V}{R} = 0 \qquad \text{Equation 1.10}$$

$$V(t) = V_o e^{-\frac{t}{RC}} \qquad \text{Equation 1.11}$$

where V_o is the voltage of a capacitor at $t = 0$. The time required for the voltage to fall to $\frac{V_o}{e}$ is called *RC* time constant and is given by $\tau = RC$.

In a charge-discharge measurement, the square of a voltage profile as a function of time is integrated to determine the stored energy in a capacitor. By using Equation 1.11, the capacitance of a capacitor in an RC circuit is also obtained.

1.3 Strategy towards Efficient, High Energy Density Film Capacitors

The surge in demand for electrical energy has served as a motivation for the development of high-performance materials for energy storage systems,[10] which generally consist of different types of devices: capacitors, supercapacitors, batteries, and fuel cells. These devices, which differ in power and energy densities, are selectively utilized primarily depending on applications and performance parameters such as power and energy density, charging time, cyclability, and working environment.[11]

Capacitors have been used for pulsed power applications that require large power density consisting of moderate energy density and fast charge/discharge speed in the order of a few milliseconds. Conventionally, thin polymeric films such as polypropylene (PP), polyester, and polyphenylene sulfide (PPS) have been materials of choice, which possess high breakdown strength and moderate energy density of up to ~3 J/cm^3. However, they suffer from low relative permittivity, limiting the energy storage density of capacitors significantly.[12, 13] As shown in Equation 1.5, the stored energy in a capacitor is linearly proportional to the relative permittivity and the square term of breakdown strength of dielectric materials. For this reason, most of the approaches for increasing energy density of a dielectric material are largely categorized by 1) increasing relative permittivity, 2) enhancing breakdown strength of dielectric materials, and 3) improving the efficiency of energy extraction by modifying molecular structure of dielectric materials.

In the following sections, three approaches to the development of novel polymeric and/or hybrid dielectric materials with high energy storage density shall be briefly reviewed and discussed.

1.3.1 High energy density polymers

After the discovery of ferroelectric polymers,[14, 15] poly(vinylidene fluoride), PVDF, and its random copolymers have been the center of interests for many researchers. Pioneering work by Zhang *et al*., opened up a potential for this class of semicrystalline polymers for energy storage applications by demonstrating relaxor ferroelectric behavior after the electron irradiation to the polymer.[16] Without a very high relative permittivity, a polymer dielectric capacitor with high energy density was demonstrated by reducing polarization hysteresis and avoiding electric displacement saturation well below the breakdown field of a polymer material.[17] Considering limitations in further increasing electronic, atomic, and rotational polarizations for polymeric system, the approach for improving the efficiency of energy extraction, in other words, reducing the loss in energy extraction seems appropriate.[18, 19]

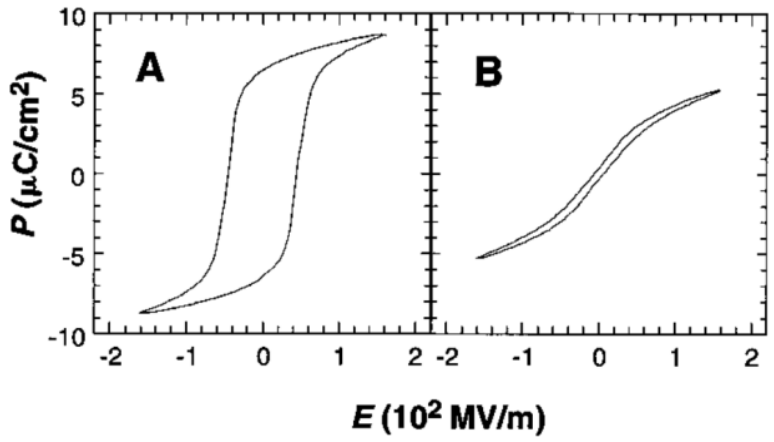

Figure 1.5 Polarization hysteresis loops of P(VDF-*co*-TrFE) 50/50 copolymer (A) before and (B) after electron irradiation with 4×10^5 Gy at 120ºC. (B) exhibits relatively lower remnant polarization and reduced maximum polarization indicating reduction of electronic and/or reorientational polarization after irradiation. Reproduced with permission.[16] Copyright © 1998, American Association for the Advancement of Science.

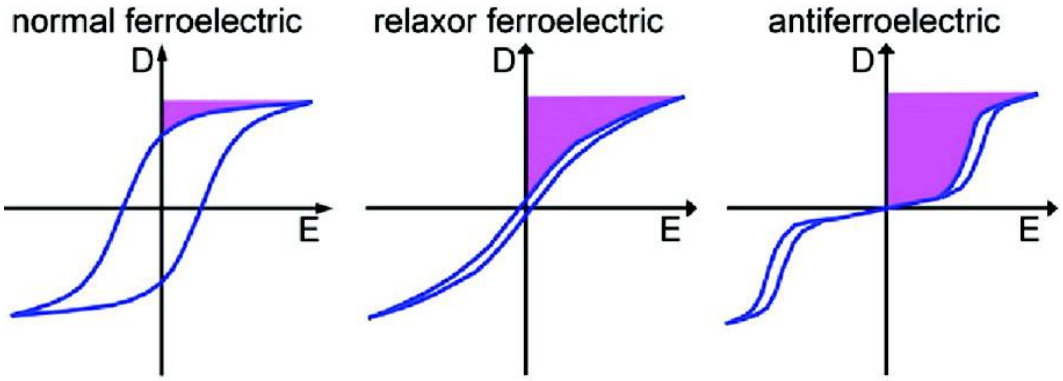

Figure 1.6 Schematic of field dependent polarization loops for a) normal ferroelectric, b) relaxor ferroelectric, and (c) antiferroelectric materials. Extractable energy is shown in shaded areas. Reproduced with permission.[18] Copyright © 2012, American Chemical Society

Many attempts for improving the efficiency of the energy extraction in dielectric materials revolve around the optimization of film processing for PVDF-based polymers including poly(vinylidene fluoride-*co*-trifluoroethylene) P[VDF-*co*-TrFE] copolymers, poly(vinylidene fluoride-*co*-trifluoroethylene-*co*-chlorotrifluoroethylene) P[VDF-*co*-TrFE-*co*-CTFE] terpolymers, PVDF-graft polymers, and PVDF blends. Since PVDF are a class of semicrystalline polymers, their crystallinity, crystal structure and orientation, molecular chain conformation are highly dependent on processing variables such as annealing temperature, history, pressure, mechanical stretching, and electrical poling.[1, 2]

F. Guan *et al*., reported the effects of film processing conditions on dielectric properties of PVDF-copolymers.[20-22] Depending on mechanical and thermal treatments, crystalline phases of PVDF-copolymers varied and this effect was reflected in the change of dielectric properties such as relative permittivity, loss tangent, polarization hysteresis, and extracted energy density. Since β-phase is the most polar among many crystalline phases in PVDF-copolymers, it is suggested to increase the amount of β-phase within crystals to maximize the polarization response of the polymer.

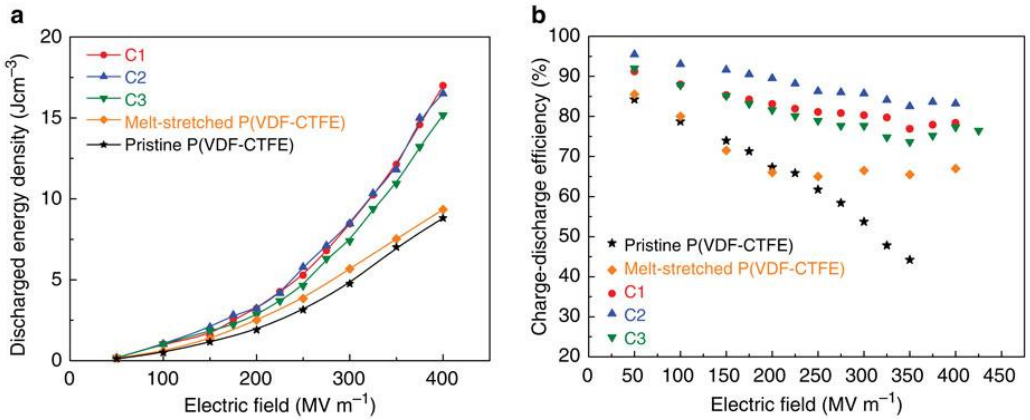

Figure 1.7 Discharged energy density (a) and charge-discharge efficiency (b) of cross-linked P(VDF-*co*-CTFE) films under various electric fields. C1 to C3 denotes cross-linked films containing 1, 3 and 5 wt% of 1,4-bis(t-butyl peroxy) diisopropylbenzene as an initiator. Reproduced with permission.[23] Copyright © 2013 Nature Publishing Group

The cross-linking method has been applied to enhance dielectric properties of neat polymers, including permittivity, breakdown strength, and dielectric and energy extraction efficiency of ferroelectric polymers. In crosslinked polypropylene (x-PP) films, increased permittivity was attributed to the induced π-electronic polarization of aromatic groups in butylstyrene (BSt) cross-linkers. Reduction of free volume or defects by cross-linking was believed to enhance breakdown strength and decrease energy loss, leading to two folds increase in energy density of cross-linked PP films.[24] Recently, Khanchaitit *et al*., have reported cross-linked ferroelectric polymer P(VDF-*co*-CTFE), which exhibited ~17 J/cm^3 of discharged energy density with much increased extraction efficiency, as compared to pristine polymers.[23] Similar to cross-linked PP, this system displayed increased permittivity and breakdown strength, which were attributed to smaller crystallite sizes that are easily switched or aligned under the application of electric field. It was postulated that the combination of reduced crystal size and enhanced dipole reversibility rendered reduced hysteresis and low ferroelectric switching loss.

Modular approach to tune the chemical composition of P(VDF-*co*-TrFE-*co*-CTFE)

terpolymers demonstrated the increase in permittivity up to 50 without negligible loss tangent. These terpolymers also showed decreased glass transition temperature and Curie temperature compared to neat PVDF, suggesting that the introduction of TrFE and CTFE contents into the polymer resulted in a reduced activation energy barrier for the crystal phase transition from ferroelectric β-phase to γ-phase.[25] It was indicated that the incorporation of bulky side groups into the backbone of PVDF altered the crystal structure in a way that the switching of domains under the application of electric field would be promoted with less remnant polarization, leading to a relaxor ferroelectric type response.

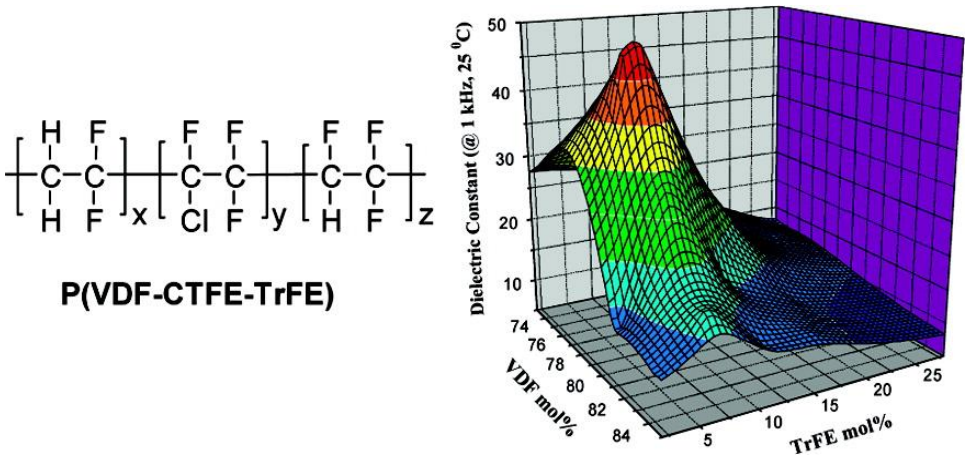

Figure 1.8 Chemical structure of P(VDF-*co*-CTFE-*co*-TrFE) terpolymer (left) and a 3-D dimensional plot of relative permittivity of terpolymers at 1 kHz at room temperature (right). The terpolymer of 78.8 mol % of VDF, 7.2 mol % of TrFE, and 14 mol % of CTFE exhibits the permittivity of 50 and a low loss tangent below 0.05. Reproduced with permission.[25] Copyright © 2006, American Chemical Society

Grafting another polymer in PVDF-copolymers as a side chain is another way to introduce defects into PVDF based ferroelectric polymer, converting normal ferroelectrics into a relaxor ferroelectric, in which a remnant polarization is significantly reduced. More interestingly, in polystyrene (PS)- and poly(methyl methacrylate) (PMMA)-grafted PVDF-copolymers, antiferroelectric-like behavior were reported.[26, 27] It is suggested that the poor compatibility of PS and PMMA with

PVDF chains forces chains of grafted polymers forming a nanoscale interfacial layer in the periphery of PVDF crystals. Although the low permittivity of grafted-polymers substantially reduces the effective permittivity of the entire system, the grafting approach is another good example of how important the efficiency of the energy extraction process is in the development of high energy dielectric materials (14 J/cm^3 for PMMA grafts).

The blends of PVDF based ferroelectric polymers and polar polymers have been prepared to investigate the effect of intermolecular interaction between PVDF crystals and additives.[28-30] It is indicated that by changing crystallinity, the composition of polar crystalline phases, and the size of crystalline domains, the improved energy extraction process is shown to be effective for dielectric capacitor with much reduced loss.

One step forward from simple blend method, micro/nanolayer coextrusion method is used to prepare laminates of nonpolar polymer and ferroelectric PVDF-copolymers.[31-37] The high-field polarization hysteresis is found to decrease with decreasing layer thickness of each and the content of ferroelectric polymer. It is proposed that the interface of laminates prevents the migration of charge carriers, which is the primary reason for hysteresis loss, to adjacent layers. This approach can be considered as a way to mitigate the charge migration and associated conduction in a dielectric material, which are known to be a primary culprit for increasing loss and premature breakdown events. This topic will be revisited in Chapter 5 with greater detail.

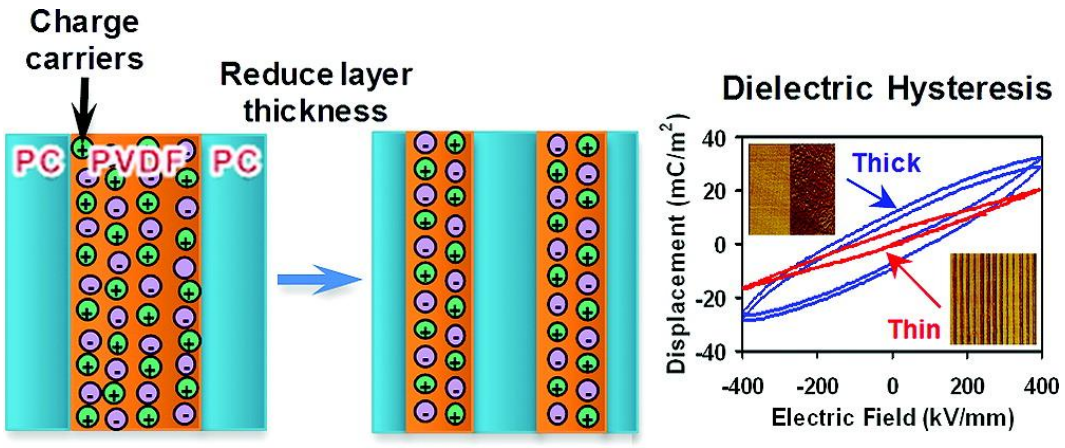

Figure 1.9 Schematic of charge migration (left) in layered films in thick and thin layers. Electric field dependent displacement loops (right) for 2 layers for 6000 nm each (denoted as Thick) and 256 layers for 50 nm each (denoted as Thin) along with AFM phase images for each films. Reproduced with permission.[34] Copyright © 2012, American Chemical Society

Other than PVDF-copolymers, a few different polar polymers have been studied for pulsed power applications. Wu et al., recently have reported dielectric films from aromatic polythiourea with relatively high permittivity of 4.5 resulting from high dipole moment of thiourea unit. Due to its amorphous structure and extremely low leakage current, discharged energy density of ~25 J/cm^3 is demonstrated at above 1 kV/μm of electric strength.[38, 39]

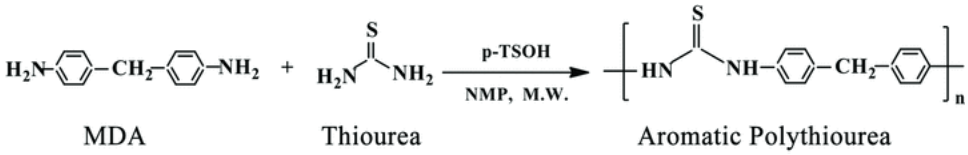

Figure 1.10 Synthetic scheme of aromatic polythiourea via microwave-assisted polycondensation of 4,4′-diphenylmethanediamine (MDA) and thiourea. Reproduced with permission.[39] Copyright © 2013 WILEY-VCH Verlag GmbH & Co. KGaA, Weinheim

Cyanopolymers also have been studied because of the large dipole moment associated with the dipolar cyano group (−C≡N) of approximately 3.5 Debye, as compared to about 2 Debye of fluorine atoms in PVDF. Among many possible polymeric systems

containing dipolar cyano groups, polyacrylonitrile (PAN) was shown to have a signature of dielectric response and form randomly spaced kinks, resulting in a relatively large degree of disorder.[40, 41] A copolymer system poly(acrylonitrile-allylcyanide) P(AN-*co*-AL) was somehow successful in stabilizing the structure against the formation of kinks.[42] The suppressed kink formation was attributed to promote the growth of larger crystallites, which were not present in PAN system. It is somehow similar approach used for P(VDF-*co*-TrFE-*co*-CTFE) terpolymers in that introduced defects change crystalline phase and molecular interactions of PVDF, thus converting normal ferroelectrics into a relaxor ferroelectric. Since P(AN-*co*-AL) copolymer has a structural similarity to the silicate sol-gel containing cyano group, which is the second main topic of this thesis, the detailed discussion of the polymer will be followed in Chapter 4.

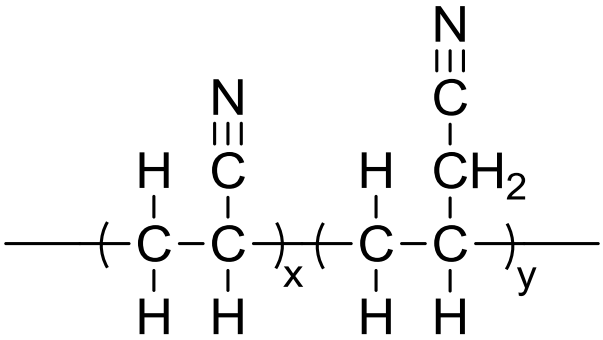

Figure 1.11 Chemical structure of the copolymer of polyacrylonitrile and polyallylcyanide, P(AN-*co*-AL).

1.3.2 Polymer nanocomposites

The low relative permittivity of polymeric materials is the significant drawback of polymeric materials for energy storage application. A composite approach wherein high permittivity inorganic fillers are added to a polymer matrix is straightforward and promising in that this approach combines advantages of both inorganic fillers with high permittivity and polymeric materials with high breakdown strength, as well as facile processibility.[43-46] However, several technical issues must be tackled to realize its full potential: 1) the selection of materials for a filler and a polymer matrix so as to maximize the energy storage performance of composites, 2) the stabilization of an inorganic filler in a polymer matrix for homogeneous mixing, and 3) the appropriate film fabrication method to optimize morphology of developed composite materials.

The most common choices for high permittivity inorganic fillers are ferroelectric metal oxides such as $BaTiO_3$, TiO_2, ZrO_2 and $Pb(Zr,Ti)O_3$. However, nanoparticles easily form aggregates because of their high surface energy and large surface area if they are not properly stabilized in a polymer matrix. Once formed, aggregates of nanoparticles significantly compromise the quality of nanocomposite films, leading to poor breakdown strength and energy storage density. Therefore, a suitable surface modification of the particles to stabilize them in the polymer matrix is a necessity. In the following, the nanocomposite approach will be divided into three parts: 1) composites in ferroelectric polymers, 2) composites in hydrocarbon polymers including polymer-grafted nanoparticle system, and 3) percolative composites with conductive fillers.

As discussed in section 1.3.1, PVDF-based ferroelectric polymers exhibit large spontaneous polarization and relatively high permittivity (~10 at 1 kHz). In

particular, because of increased energy extraction efficiency, defect-modified PVDF-copolymers such as P(VDF-*co*-TrFE), P(VDF- *co*-TrFE- *co*-CTFE), and poly(vinylidene fluoride-*co*-hexafluoropropylene) P(VDF- *co*-HFP) have been primarily utilized as a ferroelectric matrix for nanocomposites. Despite their relatively high permittivity, the issue of particle aggregation becomes more prominent in the composite with fluoropolymers because of their low surface energy.

Phosphonic acid with pentafluorobenzyl pendent group was successfully employed as a surface modifier to incorporate $BaTiO_3$ nanoparticles into the ferroelectric polymer P(VDF- *co*-HFP).[47, 48] Phosphonic acid acted as a linker to the surface of oxide particles and fluorine-terminated moiety provided miscibility to a fluoropolymer matrix. With optimized volume loading of fillers, a maximum energy density of 3.2 J/cm^3 was demonstrated.

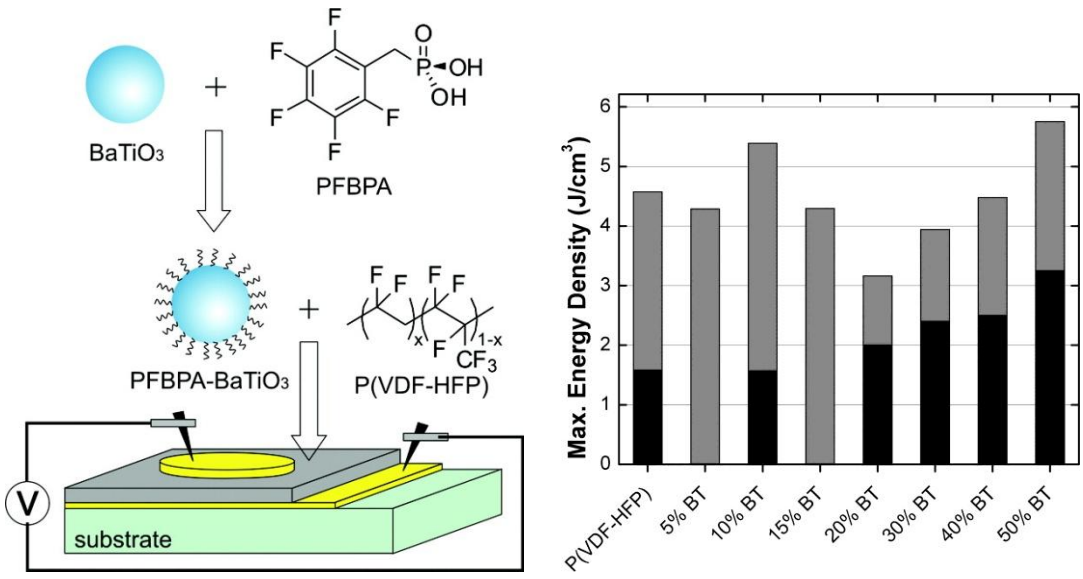

Figure 1.12 (left) Schematic illustration of surface modification of $BaTiO_3$ using pentafluorobenzyl phosphonic acid (PFBPA), and the geometry of nanocomposite thin film capacitors. (right) Calculated (gray) and measured energy density (black) of nanocomposites containing PFBPA-modified $BaTiO_3$ in P(VDF- *co*-HFP). Energy densities were measured under the fixed field strength of 164 V/μm. Reproduced under permission.[48] Copyright © 2009, American Chemical Society

Ethylenediamine-modified $BaTiO_3$ in P(VDF- *co*-TrFE- *co*-CTFE) terpolymer nanocomposite also achieved ~ 7 J/cm^3 of energy density owing to high permittivity of terpolymer matrix (~45) and the improved compatibility between the fillers and polymer matrix.[49]

In another approach, TiO_2 nanoparticles with rod shape were incorporated into P(VDF- *co*-TrFE- *co*-CTFE) with the aid of Ba-OH surface groups, which greatly enhances the dispersibility of nanoparticles in a solvent (*N*,*N*-dimethylformamide) and a polymer matrix.[50] The large energy density of 6.9 J/cm^3 was attributed to homogeneous dispersion of nanoparticles, smaller crystalline domains and a higher degree of crystallinity, as compared to neat polymer matrix.

Instead of a surface modifier for nanoparticles, polymeric modifier can be employed for the stabilization of nanoparticles. Li et al., prepared ferroelectric polymer terminated with phosphonic acid, in which reactive end-groups created covalent bond with ZrO_2 nanoparticles, leading to covalent-bonded nanocomposites.[51] A maximum energy density of 11.2 J/cm^3 at 270 V/μm with 9.1 wt% of ZrO_2 loading was obtained, which represented 60% increase in comparison to the neat polymer at the same field strength.

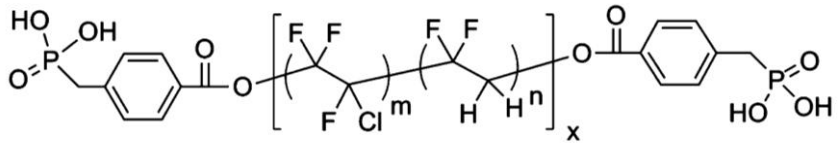

Figure 1.13 Chemical structure of phosphonic-acid-terminated P(VDF- *co*-CTFE). Reproduced under permission.[51] Copyright © 2010, American Chemical Society

The size dependence of high permittivity fillers on the dielectric properties of nanocomposite is worth revisiting because the ferroelectricity of some metal oxides such as $BaTiO_3$, $Pb(Zr,Ti)O_3$ (PZT) is size dependent.[52, 53] Mao et al., investigated

$BaTiO_3$-PVDF nanocomposite with varying $BaTiO_3$ sizes from 25 to 500 nm.[54] The remnant polarization of nanocomposites was found to increase with larger filler size, and the permittivity of nanocomposites peaked at the size of $BaTiO_3$ particles around 80 to 100 nm. Considering the loss during an energy extraction cycle associated with a remnant polarization, it can be indicated that there should be a trade-off between permittivity and extraction loss in nanocomposite system depending on the volume loading of inorganic ferroelectric fillers.

Recently, the incorporation of high-aspect ratio fillers into ferroelectric polymer matrix has been reported. Surface functionalized-barium strontium titanate ($Ba_{0.2}Sr_{0.8}TiO_3$) (BST) nanowires are incorporated into PVDF matrix and a maximum energy density of 14.9 J/cm^3 is achieved with only 7.5 volume percent of filler loading.[55] The use of high-aspect ratio filler rather than equiaxial ones is believed to afford high dielectric permittivity without losing breakdown strength of nanocomposites. Additionally, with high-aspect ratio lead zirconate titanate (PZT) nanowires, the energy storage density of nanocomposites is shown to be enhanced up to 30% through the alignment of nanowires along the direction of applied field, as compared to randomly oriented nanocomposites.[56]

Core-shell architecture is another interesting approach to stabilize inorganic fillers in a polymer matrix. Xie et al., have reported the preparation of $BaTiO_3$-core/polyamide-shell and $BaTiO_3$-core/polyamide-PMMA-double shell nanocomposites. The advantage of this core-shell structure is not only providing stabilization but also decreasing a dielectric contrast between high permittivity filler and low permittivity polymer matrix.[57, 58] Yu et al., also have reported the reduction of energy loss because of suppressed remnant polarization with $BaTiO_3$-core/silica shell nanocomposites in PVDF.[59]

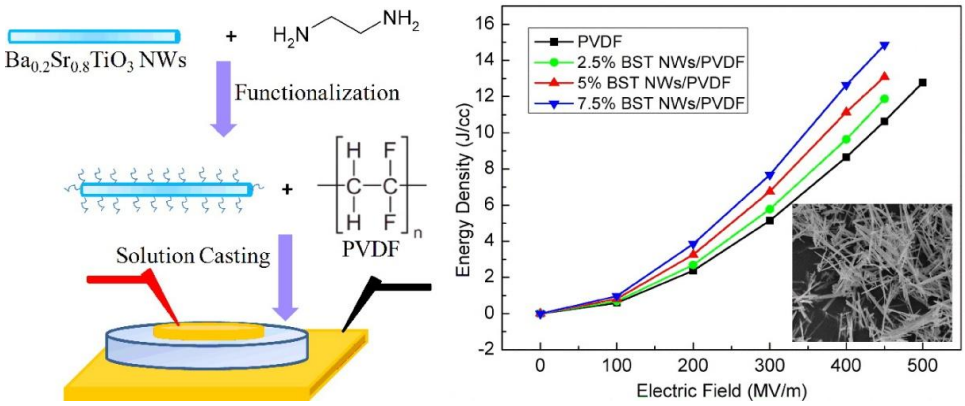

Figure 1.14 (left) Schematic of device fabrication using surface-modified BST nanowires incorporated into PVDF matrix. (right) Extracted energy density of nanocomposites and SEM images of synthesized BST nanowires. Reproduced under permission.[55] Copyright © 2013, American Chemical Society

Hydrocarbon polymers have been primarily utilized to stabilize high permittivity inorganic fillers with the grafting approach. In their pioneering paper, Maliakal *et al*., demonstrated TiO_2 oxide core, polystyrene shell nanocomposite as a candidate for high-*k* dielectric materials.[60] This oxide surface-initiated polymer grafting method provides facile synthetic route toward so-called one-component nanocomposite system, which affords better control of oxide surface and the dispersion of oxides in polymer matrix by covalency. It also does not require time consuming mixing process that is often needed in the preparation of the homogeneous mixture of nanocomposites.

Tchoul *et al*., prepared polystyrene-grafted-TiO_2 hybrid nanocomposites by a combination of phosphonate coupling and "click" chemistry.[61] The volume fraction of TiO_2 nanoparticles was controlled by varying molecular weight of polystyrene. Although the permittivity of the hybrid materials was shown to increase to 6.4, the presence of leftover ions was indicated by extremely high loss tangent at frequency range below 100 Hz.

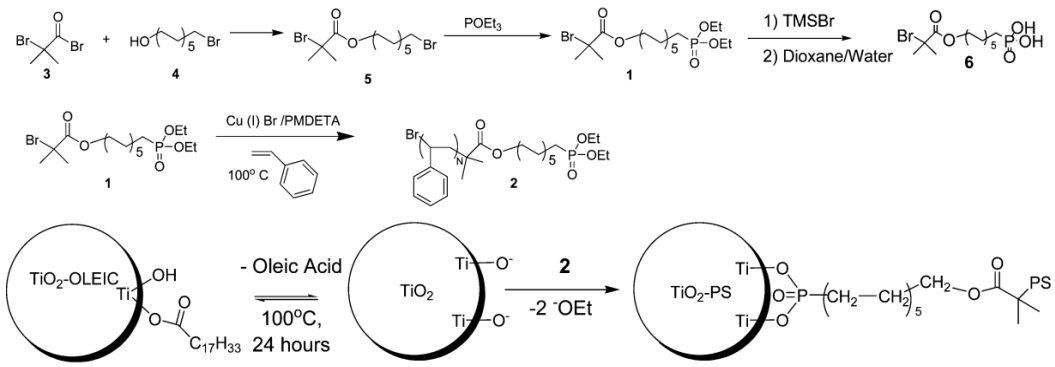

Figure 1.15 Synthesis of phosphonate terminated polystyrene (**2**) and ligand exchange reaction of diethyl phosphonate terminated polystyrene **2** with oleic acid terminated titanium oxide to generate polystyrene coated titanium dioxide (TiO_2-PS) (PMDETA = Pentamethyldiethylenetriamine). Reproduced with permission.[60] Copyright © 2005, American Chemical Society

Other examples of polymer-grafted nanoparticles involve nanocomposites containing polyolefin synthesized in situ from the surfaces of metal oxides by metallocene catalysis,[62-65] diblock copolymer-grafted to $BaTiO_3$,[66] poly(methyl methacrylate)-grafted-$BaTiO_3$,[67] TiO_2-paraffin core-shell nanoparticles.[68] Although these examples show promising synthetic routes for one-component nanocomposites, the permittivity of hydrocarbon polymers utilized usually ranges from ~2 to 5, which is substantially lower than that of inorganic fillers. This so-called dielectric contrast between two ingredients would increase the average electric field in low permittivity region, thus resulting in very little energy being stored in high-permittivity region of inorganic fillers. In addition, the dielectric contrast would bring about a local field concentration in low-permittivity polymer matrix, thus possibly leading to premature breakdown in composite materials consequently.

Besides grafting methods, a few model nanocomposite systems are studied, which contains surface modified-low *k* inorganic fillers in hydrocarbon polymer matrix. The purpose of these model systems is to investigate the effect of the nanofiller orientation on the breakdown strength of nanocomposites. Using high aspect ratio

montmorillonite (MMT) nanofillers in polyethylene matrix, Tomer et al., explored the effect of filler alignment on the dielectric properties of nanocomposites.[69] It was found that although the nanocomposites differing in the alignment/orientation of the nanofillers exhibited essentially the same morphology and crystallinity, the nanocomposites with oriented fillers achieved larger breakdown strength and energy storage efficiency. These improvements were attributed to optimized electric field distribution and suppressed electrical breakdown tree inception and propagation. Fillery et al., also showed improved breakdown strength of the model nanocomposite system, consisting of organically modified MMT and polyvinyl butyral (PVB).[70] This so-called nanolaminate is believed to provide a densely packed morphology capable of retarding breakdown and carrier mobility, thus leading to increased breakdown strength within a broad range of nanofiller fractions.

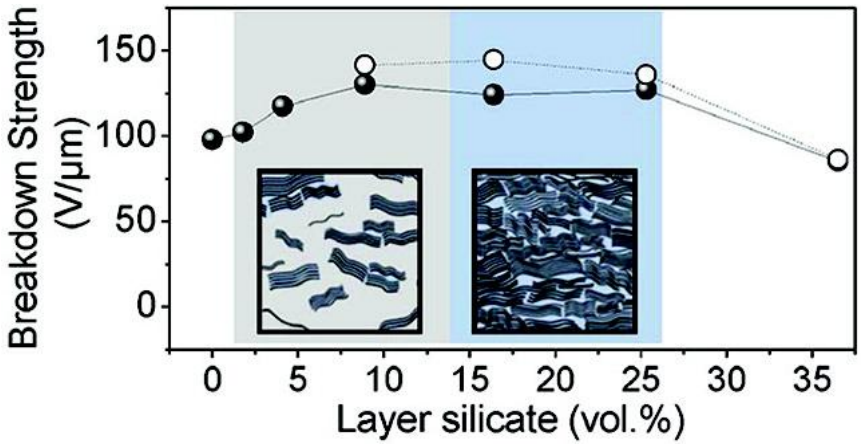

Figure 1.16 Breakdown strength of MMT-PVB nanocomposites as a function of MMT volume fraction. Solid and hollow dots represent as-fabricated and consolidated nanocomposites, respectively. Inset shows schematic illustration of the morphology of the MMT-PVB nanolaminates. Reproduced with permission.[70] Copyright © 2012, American Chemical Society

Percolative composites refer to the composites with conductive or semiconductive fillers in an insulating polymer matrix. This approach is based on a metal-insulator transition with increasing conductive filler concentration, which is characterized by

an abrupt rise in conductivity and permittivity in the vicinity of the percolation threshold.[43, 45] Dang et al., demonstrated permittivity of 400 from Ni-PVDF composite[71], and 550 with surface-modified multiwalled-carbon nanotubes in PVDF[72] near the percolation region of conducting fillers. Although remarkably high permittivity can be achieved near the percolation threshold, loss tangent and breakdown strength of these percolative composites still need to be improved to realize its full potential for energy storage applications.

Calame predicted the theoretical limit of the energy storage in nanocomposite capacitors to 10-12 J/cm^3.[73] This number was calculated for a composite composed of a linear matrix with a permittivity of 12 containing 30-40% volume fraction of inclusions with a low field permittivity of 1200 at the field strength of 300-350 V/μm. The controlling factors for energy storage density include the intensification of electric field in low permittivity matrix, the geometry of the filler particle arrangement, and the optimum volume fraction of fillers, which would otherwise lead to increased probability of electrical breakdown unless optimized. Although the energy storage density found to be feasible in this paper has been overcome in a few cases *via* the use of high permittivity polymer matrix, the optimized geometry of filler arrangement, and controlled morphology that favors enhanced breakdown strength of composite materials, the controlling factors that would limit the energy storage capability should be taken care of when the nanocomposite approach is utilized.

1.3.3 Polar hybrid sol-gel materials

Sol-gel processing is defined by the formation of interconnected three dimensional network, a *gel*, with submicron pores and polymeric chains, whose length scale ranges up to micrometers, from the dispersions of colloidal particles, *sols*, in a liquid.[74] A sol-gel precursor includes silicon alkoxides or nitrates and metal alkoxides. The structure of a gel ranges from well-ordered lamellar structure to polymeric networks with covalent link and disordered physical entanglement. A typical sol-gel reaction comprises simultaneous hydrolysis and condensation of sol-gel precursors followed by the formation of 3-D network. Depending on the condition of thermal treatments for the evaporation of residual solvent, aerogel or xerogel is produced.

The advantage of sol-gel processing is primarily the mild processing condition near ambient temperature and the capability for crafting composite materials at the molecular level. Therefore, both organic and inorganic phases can be mixed to produce a molecular hybrid, which could have not been made by conventional methods, that maintains the properties of both components. In this regard, the incorporation of molecules that exhibit a permanent dipole moment into sol-gel matrix may be one way to produce polar macromolecules. However, to realize polar sol-gel materials, polarizable moieties in sol-gel network should be packed in such a way that the dipole moment of each unit does not cancel out.

Kwon et al. investigated organic-inorganic sol-gel hybrids comprising sols of trimethoxysilane with acrylate and fluorinated aromatic bisphenol A with high electronic polarizability.[75] This sol-gel hybrid achieved a relative permittivity of 13 at 1 kHz but no dielectric breakdown strength was reported. The authors incorporated surface-treated $BaTiO_3$ nanoparticles (average size ranges from 50-80 to 400 nm) into the sol-gel matrix, which resulted in increasing the relative permittivity up to 62 at 1 kHz. Although the

detailed mechanism for large polarization response of this sol-gel hybrid was not presented, the authors speculated that the permanent dipole moment of fluorinated bisphenol A moieties underwent orientational polarization under the application of the external field.

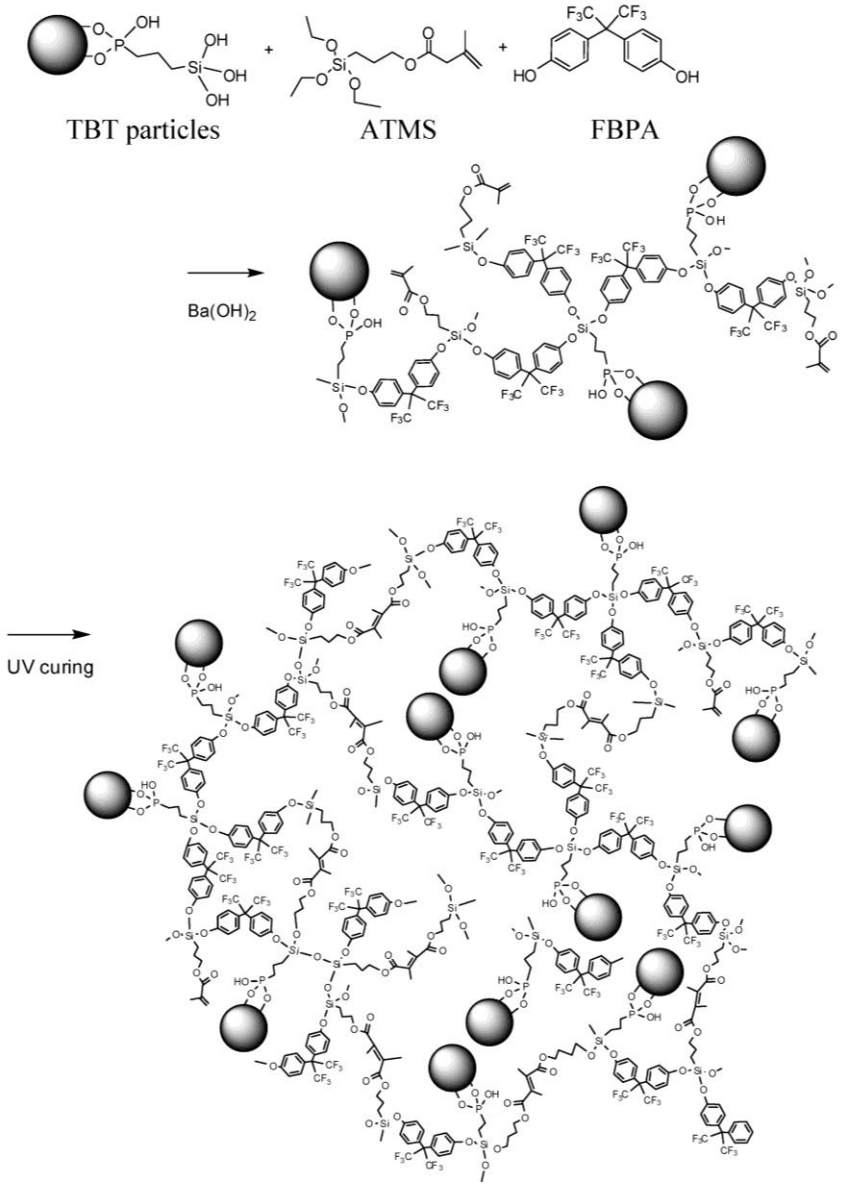

Figure 1.17 Synthetic scheme of organic-inorganic sol-gel hybrids comprising sols of trimethoxysilane with acrylate (ATMS), fluorinated aromatic bisphenol A (FBPA), and silane terminated $BaTiO_3$ nanoparticles. Reproduced with permission.[75] Copyright © 2010, American Chemical Society

Another example of polar sol-gel materials include sol-gel films prepared from a mixture of cyanoalkylsiloxane precursors, which have been reported to exhibit the relative permittivity of 27 and loss tangent below 0.05 with good thermal and mechanical stability.[76] This patent attributed the large permittivity of sol-gel films to orientation polarization of cyano groups, which possess a permanent dipole moment, under the influence of electric field. It is worthwhile to note that the authors varied the molar ratio of difunctional silane to trifunctional silane from 1 to 0.25 and the tensile strengths of sol-gel films ranged from 50 to 430 kg/cm^2, respectively.

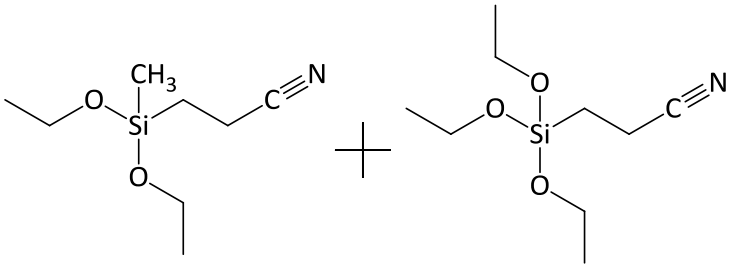

Figure 1.18 Chemical structure of cyanoalkylsiloxane precursor blends for sol-gel films utilized in reference 73.

In addition to the abovementioned approach utilizing polar silicon alkoxide precursors, polar sol-gel materials can be prepared by the doping of polar molecules to sol-gel matrix. Avnir reviewed many sol-gel materials with entrapped polar molecules for optics and photophysics applications.[77] The entrapment process comprises the introduction of dopant molecules to the dispersion of sols, followed by the entrapment of dopants within sol-gel matrix when a sol turns into a gel, which typically produces a porous xerogel. Naik et al. also reported the entrapment of enzymes and inorganic cobalt platinum nanoparticles, whose average size was 4 nm, in silica particles prepared from tetramethoxysilane sol-gel precursor.[78]

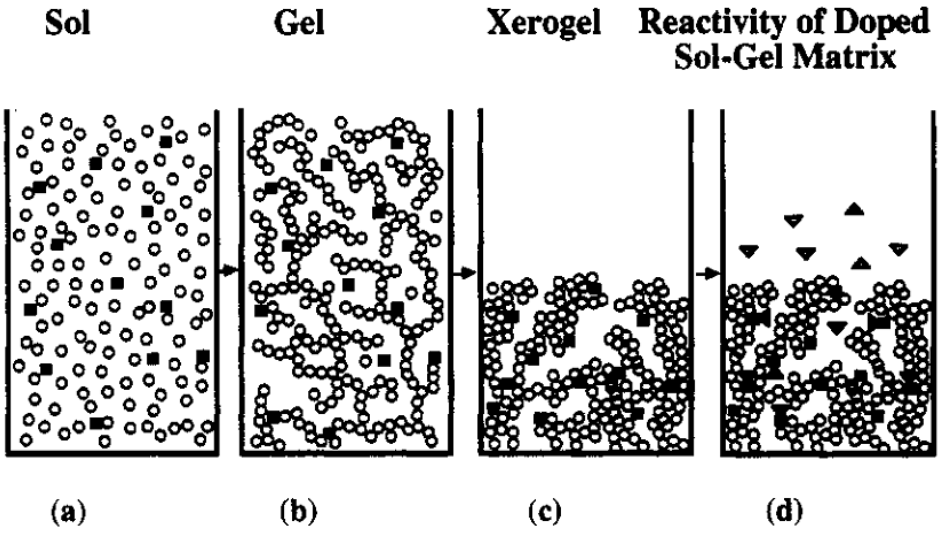

Figure 1.19 Schematic illustration of the entrapment process. (a) a sol of inorganic oxide particles is prepared in the presence of desired dopant molecules. (b) Sols turn into a gel, forming a xerogel (c). The porous network allows external molecules to diffuse into the matrix and react with the trapped molecules (d). Reproduced with permission.[77] Copyright © 1995, American Chemical Society

In brief, sol-gel processing allows the preparation of polar sol-gel hybrid materials by means of the incorporation or the entrapment of polar molecules in the sol-gel matrix. However, as an analogy to ferroelectric polymers, the polar molecules in sol-gel matrix should be packed in such a manner that the dipole moment of each polar unit is not compensated when the 3-D sol-gel network forms. In this regard, the structural change in polar sol-gel materials associated with various processing parameters involved in sol-gel processing should be investigated and optimized to realize polar sol-gel hybrid with large polarization response.

1.4 Overview and Organization of the Thesis

The introduction and literature survey put forward in this chapter serves to introduce basic concepts and approaches to the development of efficient, high energy dielectric materials. While two different types of materials, nanocomposites and polar sol-gels, will be dealt with in this thesis, these materials will be characterized with the same tools and techniques.

Chapter 2 details experimental methods including the preparation of dielectric films, characterization techniques, the fabrication of capacitor devices, and detailed information about field dependent polarization loops, which is of great significance in evaluating the efficiency of materials during the charge-discharge processes.

In chapter 3, nanocomposite thin films are prepared by using two different methods, and the effect of these methods on the morphological and dielectric properties are compared. Chapter 4 introduces polar sol-gel material bearing dipolar organic cyano side groups, which is relatively a new class of dielectric material. The orientational polarization of polar cyano groups is attributed to the dielectric response of this sol-gel material, and its full characterization for energy storage applications is presented. In chapter 5, the effect of tunneling barrier layer on the polar sol-gel material is investigated to enhance its dielectric properties particularly at high electric field. Outlook for the development of dielectric materials for energy storage applications is presented in chapter 6.

CHAPTER 2

EXPERIMENTAL DETAILS

2.1 Film Preparation Procedure

In this thesis, all films for capacitor devices are prepared by solution casting method. In spin coating, a few drops of polymer solution, which consists of polymeric matrix, nanosize fillers (if needed), and solvent are applied onto a substrate spread into thin film layers when a spinning head attached to a substrate rotates. The centrifugal force by rotating motor is a governing force in this process, and the thickness of films can be tuned by changing the spinning speed, viscosity of solution, and the evaporation speed of solution, which can be controlled by the temperature of the substrate and the vapor pressure of a spinning chamber.[79, 80]

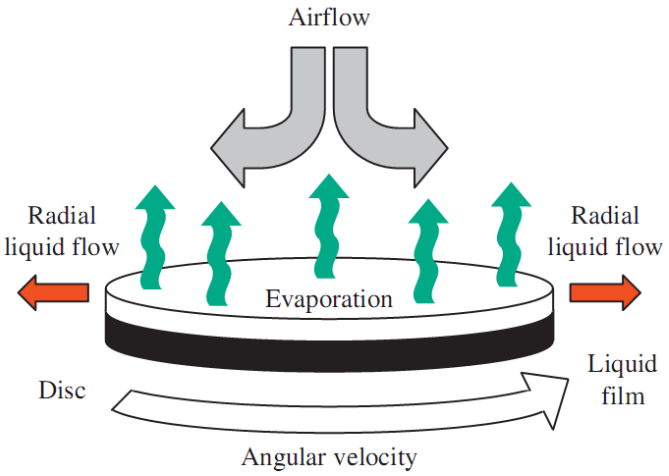

Figure 2.1 Schematic illustration of spin coating. Reproduced with permission.[80]

Blade casting also utilizes a polymer solution to be spread on a substrate. However, instead of a spinning head in spin coating, a blade in motion exerts shear force on a polymer solution. The thickness of films can also be controlled by modifying the speed of the blade, viscosity and evaporation kinetics of the solvent, similar to that in spin

coating.[81, 82] Particularly, the lower evaporation speed of solvent in blade casting as compared to spin coating, may allow sufficient time for evaporation without the formation of air voids in the film, which will be discussed in Chapter 3 in which highly filled nanocomposite films prepared by either spin or blade casting are compared.

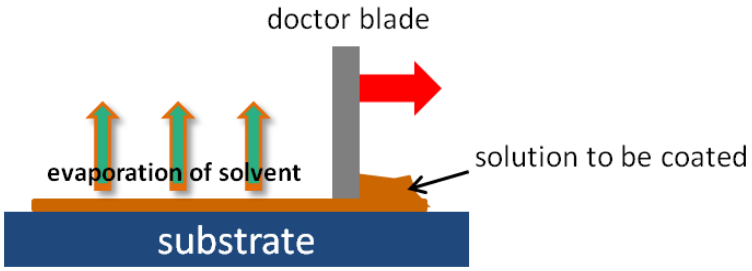

Figure 2.2 Schematic illustration of blade casting.

Typically, the procedure of film preparation consists of 1) the preparation of homogeneous solution, 2) the cleaning of a substrate, 3) the formation of a film by proper method, and 4) a thermal treatment to remove the solvent inside a film.

For nanocomposite solutions containing nanosize filler, polymer matrix, and a solvent, a homogeneous mixture was obtained by ball-milling of the mixture in a Teflon jar for several days. Yttria-stabilized zirconia ceramic particles of different diameter were used as grinding media to break up agglomerates, as well as to prevent the aggregation of nanoparticles. For sol-gel solutions containing a sol-gel precursor and a solvent, a mixture was obtained by stirring the reaction mixture typically for overnight.

Prior to film casting, all substrates (aluminum-coated glass substrates (Newport Thin Film Laboratory) and indium tin oxide (ITO) coated glass substrates (Colorado Concept Coatings, LLC)) were cleaned by ultrasonication with acetone for ten minutes followed by similar treatment with isopropyl alcohol and then, if needed, treated with cold plasma at 750 W for about three minutes.

A spin coater (Laurell WS-400B-8NPP/Lite) and a manual film applicator (Elcometer 3580) with a speed of ~5 cm/s were used to prepare spin- and blade-cast films, respectively. After the film casting, nanocomposite films were soft-baked on a hot plate at 80 ºC for a few minutes followed by overnight drying at 120 ºC *in vacuo*. For sol-gel films, soft baking in a hot plate was omitted and films were dried *in vacuo* at an elevated temperature up to 130 ºC for 3.5 hours. Depending on the type of substrate used, the as prepared sol-gel films were either directly baked or dried after one day of ageing in a desiccator. After drying, the thickness of films was determined by using a surface profilometer (Dektak 6M, Veeco).

2.2 Spectroscopic and Microscopic Characterization

For surface-modified $BaTiO_3$ (BT) nanoparticles in polymer/ceramic nanocomposites, the surface modification was confirmed by Fourier transform infrared (FT-IR, Perkin-Elmer Spectrum 1000) spectra using the KBr pellet method with a resolution of 2 cm^{-1}. Thermogravimetric analysis (TGA Q50, TA Instruments) was conducted to determine the surface coverage of organic surface modifiers on BT. To study the crystallinity of nanocomposite and sol-gel films, room temperature wide angle X-ray diffraction patterns were obtained on films using an X-ray source with $\lambda = 0.154$ nm (PANalytical, X'Pert PRO Alpha-1).

To study morphological property of the films, microscopic tools were utilized. Top-surface and cross-sectional images were obtained by field-emission scanning electron microscope (FE-SEM, Zeiss Ultra60) on samples with a sputtered gold coating. To minimize the structural change in cross-sectional samples, all specimens were freeze-fractured in liquid nitrogen. Transmission electron microscopy (TEM) images were collected using a TECNAI F30 microscope (FEI, Oregon, USA), operated at 300 kV.

The surface morphology of the films was also measured by an atomic force microscope (AFM, Digital Instrument Nanoscope IIIa – Dimension 3000).

2.3 Device Fabrication and Electrical Characterization

Parallel-plate capacitors were produced by depositing circular aluminum top electrodes (480 nm thick and areas of 0.25 and 1.0 mm^2) on top of nanocomposite and/or sol-gel films using a thermal evaporator (PVD75, Kurt J. Lesker) through a shadow mask at a deposition rate of 3 Å/s.

The frequency-dependent capacitance and loss tangent of capacitors were measured from 20 Hz to 1 MHz at either 0.1 or 1 V_{rms} inside a glove box by using an LCR meter (Agilent 4284A). For temperature-dependent capacitance and loss tangent measurements, a specimen was placed on top of a hot plate with desired temperature. To reduce a temperature fluctuation, measurements were performed in closed environment, and several minutes were allowed after desired temperature was reached.

The dielectric breakdown strength, E_B, was measured inside a glove box (Labmaster 130, M. Braun) using a probe station (H-100 Signatone) equipped with a micromanipulator, a microscope and a high-voltage power supply (Keithley 248 or Trek 610-D). Breakdown testing was performed by ramping an applied voltage from 50 V (DC) at a rate of 10 V/s until a catastrophic breakdown occurred, which was indicated by a rapid increase in leakage current above 5 μA. The electrode area of 0.25 mm^2 was used for breakdown testing and at least 20 devices were tested to provide average and standard deviation of E_B. The leakage current density was measured by applying DC voltage while monitoring current output using a source monitor unit (Agilent E5272A) connected to a probe station in a glove box.

Energy densities of capacitor devices were determined by the pulsed charge-discharge (C-D) and electric field dependent polarization (P-E) methods. In the pulsed C-D method, a voltage pulse with a rise and a hold time of a few hundred milliseconds under various electric fields was employed. The measurement was performed at progressively higher voltages until electrical breakdown occurs, which was indicated by highly jittery signal during a charge cycle or significantly reduced discharged energy. The polarization-electric field (P-E) experiments were performed using a home-built modified Sawyer-Tower circuit controlled by LabVIEW. Same as C-D measurements, progressively higher voltages were applied until a device reached the electrical breakdown point. For both measurements, samples with the electrode area of 1 mm^2 were subjected to voltages up to 2 kV provided by a high voltage amplifier (Trek 610-D). For the P-E method, a unipolar sine waveform with a period of 0.01 s was used, and induced charges on a sample were measured using a charge integrator circuit. Since all samples were tested under ambient conditions, special care was taken to maintain appropriate distances (> 1 cm) between probes and cablings to avoid a flash-over.

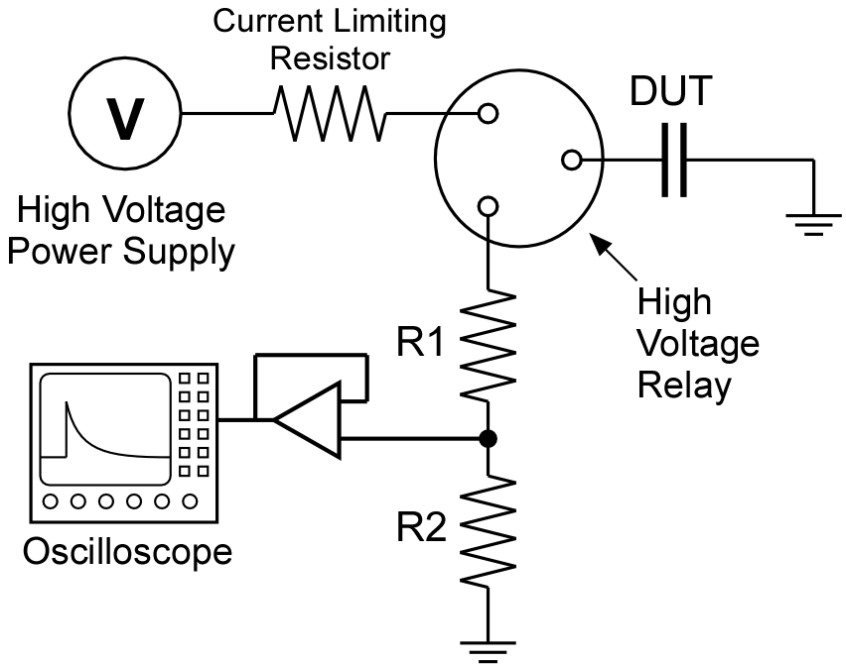

Figure 2.3 Schematic illustration of a charge-discharge test circuit. Reproduced with permission.[48] Copyright © 2009, American Chemical Society

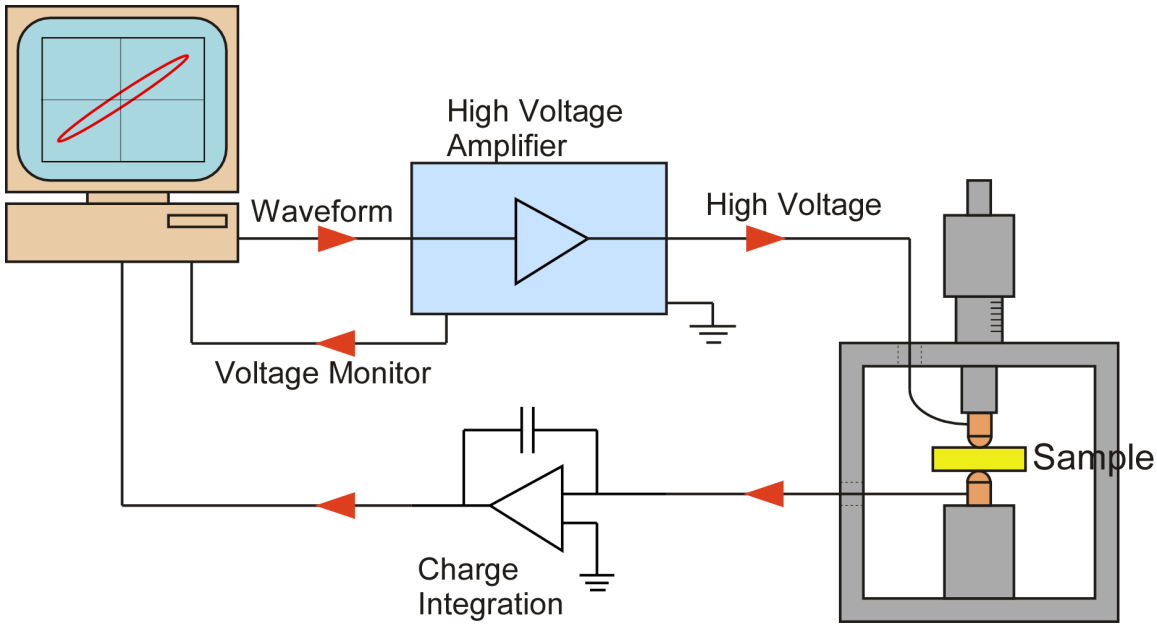

Figure 2.4 Schematic illustration of a field dependent polarization measurement circuit.

2.4 Interpretation of Polarization-Electric Field (P-E) Loops

In a capacitor of capacitance *C*, holding a charge $+q$ on one plate and $-q$ on the other plate, the work needed to move a small element of charge *dq* from one plate to the other against the potential difference *V* is defined as *dW*, and this work is equivalent to energy stored in a capacitor.

$$U_{stored} \equiv W = \int_0^Q V dq = \int_0^Q \frac{q}{C} dq = \frac{1}{2}\frac{Q^2}{C} = \frac{1}{2}QV = \frac{1}{2}CV^2 \quad \text{Equation 2.1}$$

where *Q* is the charge stored in a capacitor, and *V* is the voltage applied.

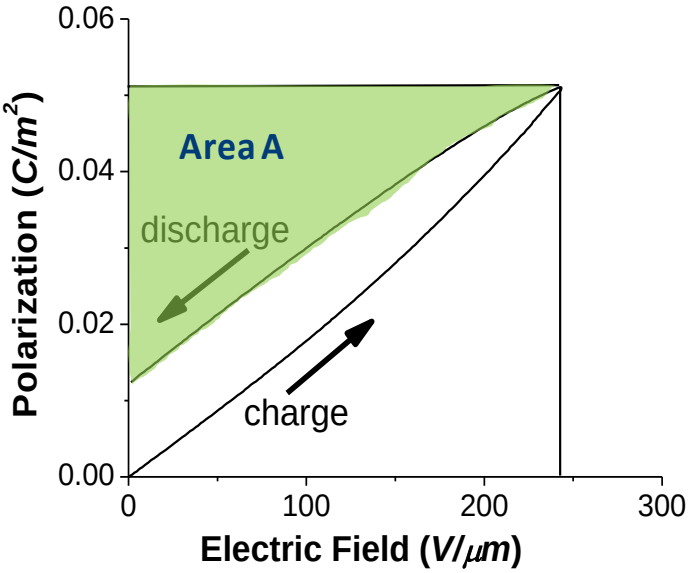

Figure 2.5 The determination of extractable energy density, U_{max}, and energy extraction efficiency by using hysteresis loops from P-E measurements.

In polarization-electric field (P-E) measurements, the summation of integrated area A and B shown in Figure 2.5 is the energy stored in a capacitor, which is also shown in Equation 2.1, and the area A is an extracted energy during a discharge cycle. Therefore, the energy extraction efficiency is defined by the ratio of extracted to stored energy in a capacitor, which is shown in Equation 2.2.

$$Efficiency = \frac{A}{A+B} \qquad \text{Equation 2.2}$$

In P-E measurements, total currents determined by induced charges on a sample measured in a charge integrator circuit is the sum of conduction and displacement currents.[83]

$$J_{total} = J_c + J_d \qquad \text{Equation 2.3}$$

Since,

$$P = \varepsilon_o \chi E \qquad \text{Equation 2.4}$$

$$D = \varepsilon_o E + P = \varepsilon_o (1 + \chi) E = \varepsilon_o \varepsilon_r E = \varepsilon E \qquad \text{Equation 2.5}$$

where *P* is polarization; *D* is displacement; ε_r and ε_o are relative and vacuum permittivities; χ is electric susceptibility; *E* is applied field.

By combining Equations 2.4 and 2.5 into 2.3, Equation 2.6 is obtained, which allows for the determination of conduction current of linear dielectric materials.

$$J_c = J_{total} - J_d = \frac{dD}{dt} - \frac{dP}{dt} = \frac{dD}{dt} - \varepsilon_o (\varepsilon_r - 1) \frac{dE}{dt} \qquad \text{Equation 2.6}$$

where J_c, J_d, and J_{total}, are conduction, displacement and total current densities.

Please note that Equation 2.6 is only valid in the linear dielectric regime, which is dependent on the polarization response of materials such as linear dielectric, paraelectric, ferroelectric, and antiferroelectric polarizations, as well as the field strength applied to the materials.

Relative permittivity, ε_r, of a dielectric material can be determined from the slope of P-E loops in relatively low electric field using the relationship in Equation 2.4.[84]

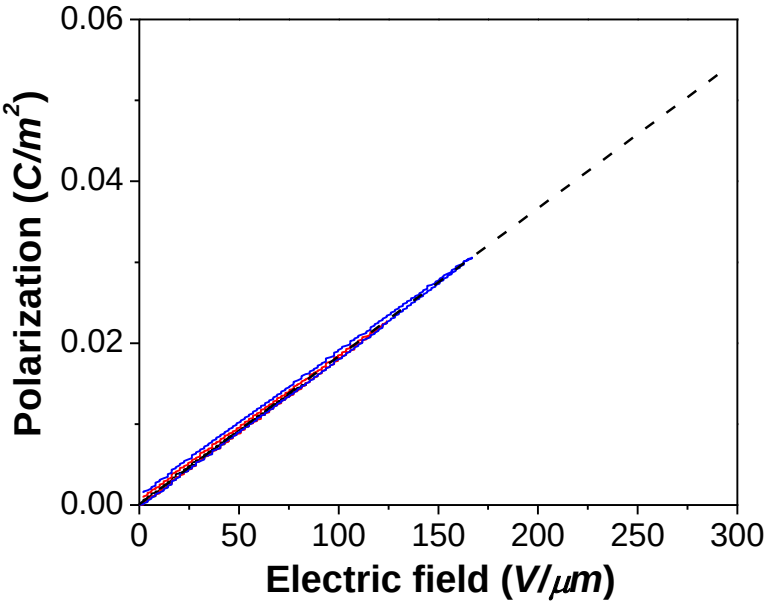

Figure 2.6 The P-E loops of sol-gel films based on 2-cyanoethyltrimethoxysilane precursor, which exhibit linear dielectric response. Dashed guideline shows the slope of P-E loops, which is the relative permittivity of this sol-gel material that can be used in the determination of conduction current in Equation 2.6.

CHAPTER 3

ENHANCEMENT OF ENERGY STORAGE PERFORMANCE OF HIGHLY FILLED $BaTiO_3$/POLY(VINYLIDENE FLUORIDE-*co*-HEXAFLUOROPROPYLENE) NANOCOMPOSITE FILM CAPACITOR *via* BLADE CASTING

3.1 Motivation

Polymeric thin films have long been the material of choice for capacitors because of their high dielectric strength and fast electrical charge/discharge speeds.[17, 85] However, the low relative permittivity of polymeric materials significantly compromises the energy density of capacitors, and more importantly, limits the potential of capacitors used for energy storage device applications. Among the many approaches to improving relative permittivity of polymeric materials, the nanocomposite approach wherein a high permittivity inorganic nanoparticle is added to the polymer is promising because it combines advantages of both inorganic nanoparticles with high permittivity and polymeric materials with high breakdown strength (E_B), as well as facile processibility.[44-46]

Previously, Kim *et al*., have reported on dielectric nanocomposites consisting of poly(vinylidene fluoride-*co*-hexafluoropropylene), P(VDF-*co*-HFP), as a ferroelectric host matrix and high-permittivity $BaTiO_3$ nanoparticles as an inorganic filler, which exhibited 3.2 J/cm^3 of an extractable energy density at a field strength of 164 V/μm with a nanoparticle volume fraction of 50%.[48] Although the fabrication of reasonably uniform nanocomposite thin films was demonstrated *via* the surface modification of $BaTiO_3$ nanoparticles with phosphonic acid ligands, the energy density of the nanocomposite films was compromised as a result of the decrease of E_B, for nanoparticle loadings above

10–20%. The reduced E_B has been generally attributed to an increase in porosity, the enhancement of the local electric field in the host material, and aggregation of the nanoparticles.

The effect of processing method on the physical properties of thin films and their associated device performance has been an extensively studied topic in solution-processed thin-film electronics such as transistors, photovoltaics, and dielectrics.[80, 86] In the fabrication of nanocomposite films bearing nano-size fillers dispersed in polymeric matrix *via* solution casting, the ordering and the packing of nano-fillers are known to depend largely on the processing method and variables such as solvent, shear rate, evaporation rate, substrate temperature, and annealing conditions. In particular, Mittal *et al*. reported the orientation of titanium dioxide nanoparticles along the direction of the coating flow *via* a fixed blade.[87] Bodnarchuk *et al*. also demonstrated enhanced ordering of magnetic nanocrystals from colloidal suspension *via* blade casting.[88] In this work they found that the ordering in films made by blade casting was greatly improved compared to the films fabricated by inkjet or drop casting. Given the fact that nanocomposite films for capacitors have usually been fabricated by spin casting or for thick films, drop casting followed by hot pressing, it is of great importance to investigate the effect of processing method on the performance of thin film capacitors.

In this chapter, comparative work on the fabrication of nanocomposite thin films *via* two independent processing methods, spin and blade casting, and a detailed study of their morphological, dielectric, and energy storage properties are presented. To investigate the effect of processing method on the energy storage characteristics of thin film capacitors, a nanocomposite model system is chosen that contains 50% volume loading of $BaTiO_3$ nanoparticles surface modified with pentafluorobenzyl-phosphonic acid (PFBPA) in P(VDF-*co*-HFP) matrix, which exhibited the largest extractable energy density in the previous report.[48] Additionally, to examine the effect of nanoparticle size on the

extractable energy density and efficiency, nanocomposites consisting of PFBPA modified 50 or 120 nm $BaTiO_3$ particles (PFBPA-BT) have been prepared and compared as to their processing *via* blade vs. spin coating methods. Dielectric characterization of all fabricated films included relative permittivity, loss tangent, electrical breakdown strength, Weibull statistics, extractable energy density and extraction efficiency. The extractable energy densities of blade-cast films show at least a two-fold increase compared to spin-cast films, establishing the significance of processing method as a means to improve the energy storage capability of thin film nanocomposite capacitors.

3.2 Materials

Chemicals and raw materials used here were obtained from the following commercial sources and used as received: 2,3,4,5,6-pentafluorobenzylphosphonic acid (PFBPA, Sigma-Aldrich), $BaTiO_3$ (BT, 50 nm average diameter nanopowder, Sigma-Aldrich; 120-150 nm, Cabot corp.), poly(vinylidene fluoride-*co*-hexafluoropropylene) (P(VDF-*co*-HFP), Sigma-Aldrich). All the solvents were reagent grade and used without further purification. Surface modification of BT was performed using a method reported previously.[48]

3.3 Surface Modification and Characterization of $BaTiO_3$ Nanoparticles

Nanoparticles easily form aggregates because of their high surface energy and large surface area if they are not stabilized properly in a polymer matrix. Once formed, nanoparticle aggregates in a polymer matrix significantly compromise the quality of nanocomposite films. Kim *et al*., have previously shown that PFBPA stabilized BT particles in ferroelectric polymeric host, P(VDF-*co*-HFP). The resultant nanocomposite

films exhibited homogeneous microstructure up to 50% of nanoparticle volume loading.[47, 48]

Surface modification of BT by PFBPA was confirmed by the FT-IR spectra, which are shown in Figure 3.1. Both 50 nm and 120 nm of BT nanoparticles bearing PFBPA ligands exhibit C-F stretching mode from PFBPA at around 1125 cm^{-1} and characteristic peaks of P-O-M (M stands for Ti or Ba) stretching modes at around 1045 and 1095cm^{-1}.[48] The surface coverage of organic ligands on nanoparticles was determined by the weight loss of nanoparticles *via* thermogravimetric analysis. In this way, the surface coverage of PFBPA on 50 nm and 120 nm BT nanoparticles was determined to be 92% and 125% of theoretical monolayers, respectively (Figure 3.2), assuming the footprint of each phosphonic acid head group as 24 $Å^2$.[89] The decomposition of PFBPA mainly occurred at temperatures ranging from 450 °C to 500 °C on both BT nanoparticles.

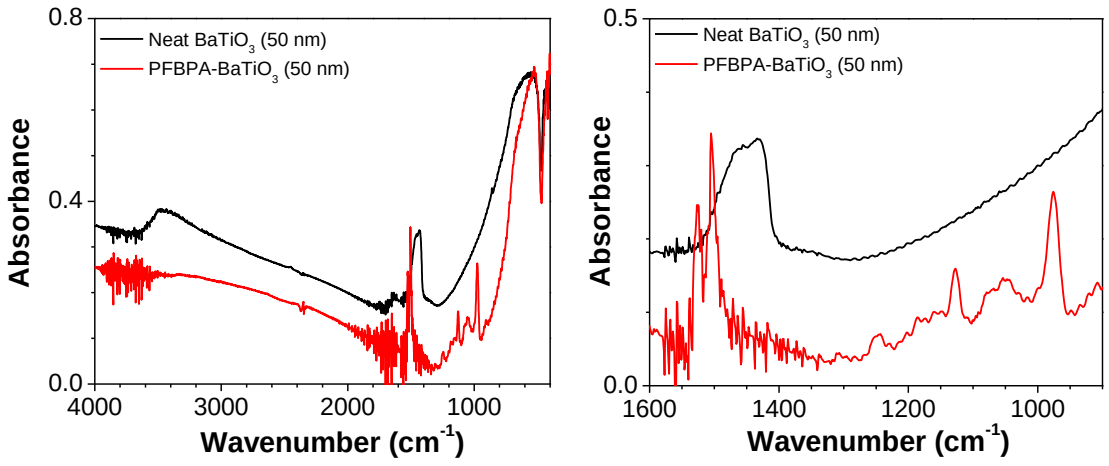

(a) (b)

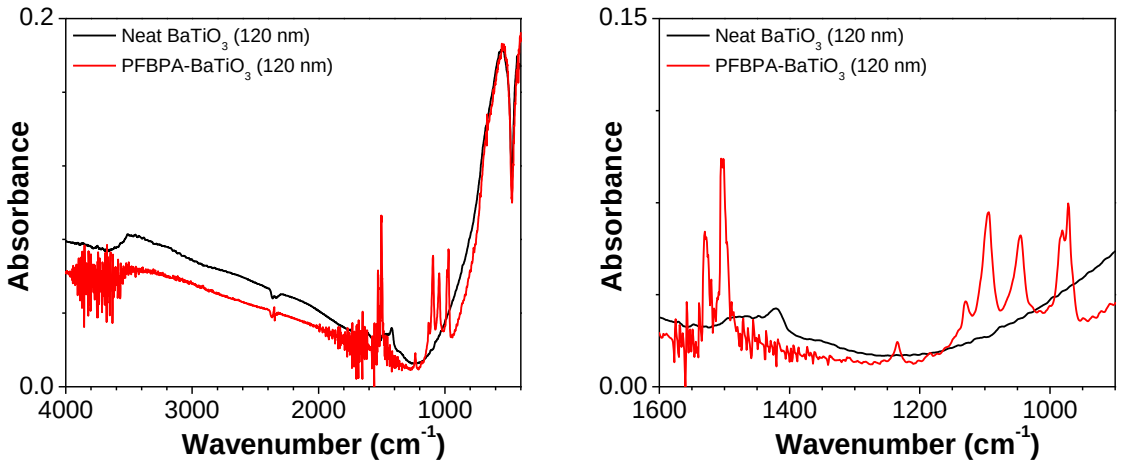

(c) (d)

Figure 3.1 FT-IR absorption spectra of unmodified (in black) and PFBPA-modified BT (in red) ((a) and (b): 50 nm BT, (c) and (d): 120 nm BT). All spectra were normalized using the Ti-O absorption peak at ~540 cm^{-1}.

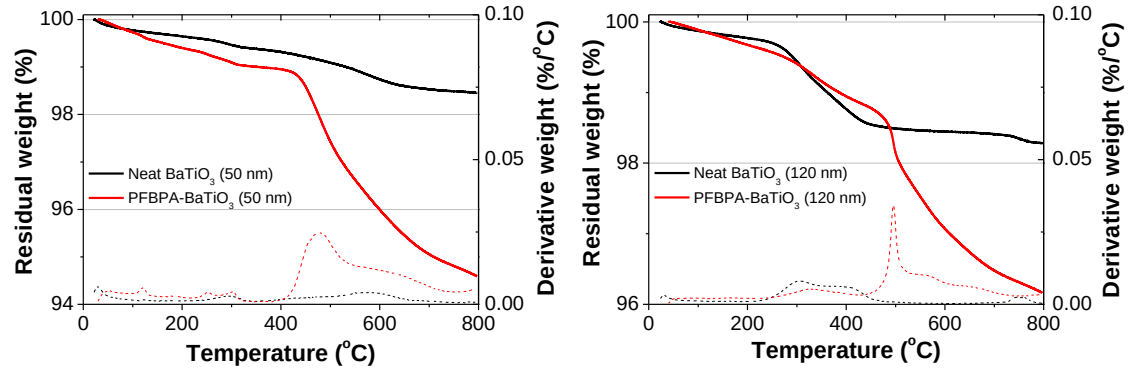

(a) (b)

Figure 3.2 Thermogravimetric analysis of unmodified (in black) and PFBPA-modified BT particles (in red) ((a) 50nm BT; (b) 120 nm BT). Residual weight is shown in solid lines and the derivative of residual weight is shown in dashed lines.

3.4 Thin Film Morphology

In the nanocomposite approach to improving properties of materials such as permittivity, breakdown strength, and processibility, the interface between nanoparticles and a polymer matrix plays a pivotal role in determining the success of this approach.[90-93]

Interfaces in dielectric nanocomposites consisting of oxide nanoparticles and a polymeric matrix can be largely governed by the dispersion of the nanoparticles in a matrix. In our earlier reports, BT nanoparticles were successfully stabilized and homogeneously dispersed in P(VDF-*co*-HFP) matrix by employing PFBPA surface modifier.[47, 48] Not only the homogeneity but also the overall morphology of the nanocomposite was greatly improved by the treatment of interfaces between BT nanoparticles and P(VDF-*co*-HFP).

In addition to the improved interfaces *via* the surface treatment of BT nanoparticles, in this chapter we investigate the distribution of BT nanoparticles in P(VDF-*co*-HFP) *via* different fabrication methods, *i.e.*, blade vs spin casting. Blade casting utilizes shear force exerted by a blade in motion, which is beneficial for the distribution of nanoparticles in a matrix. In addition, the lower rate of solvent evaporation in blade casting, as compared to spin coating, may allow sufficient time for evaporation without the formation of air voids in the film, which is a problem for highly filled nanocomposite films formed by spin coating. Previous experimental results also showed better ordering of particles in thin films *via* blade casting.[82, 87, 88]

Figure 3.3 and 3.4 show the cross-sectional SEM images of nanocomposite films prepared *via* spin and blade casting. Nanocomposite films with the same size of BT particles were displayed next to each other to compare the effect of processing method on the distribution of nanoparticles and morphology of thin films. Compared to spin-coat films, blade-cast films show a denser microstructure, which is evidenced by a lower number density of voids. The reduction of porosity in blade-cast films can be correlated to the improved breakdown strength and its statistics because of the lower probability of porosity-induced breakdown events as the density of voids and percolation of nanoparticles are lowered.[48] It is also worthwhile to note that the enhancement of morphology *via* blade casting is more noticeable in the 120 nm BT nanocomposites.

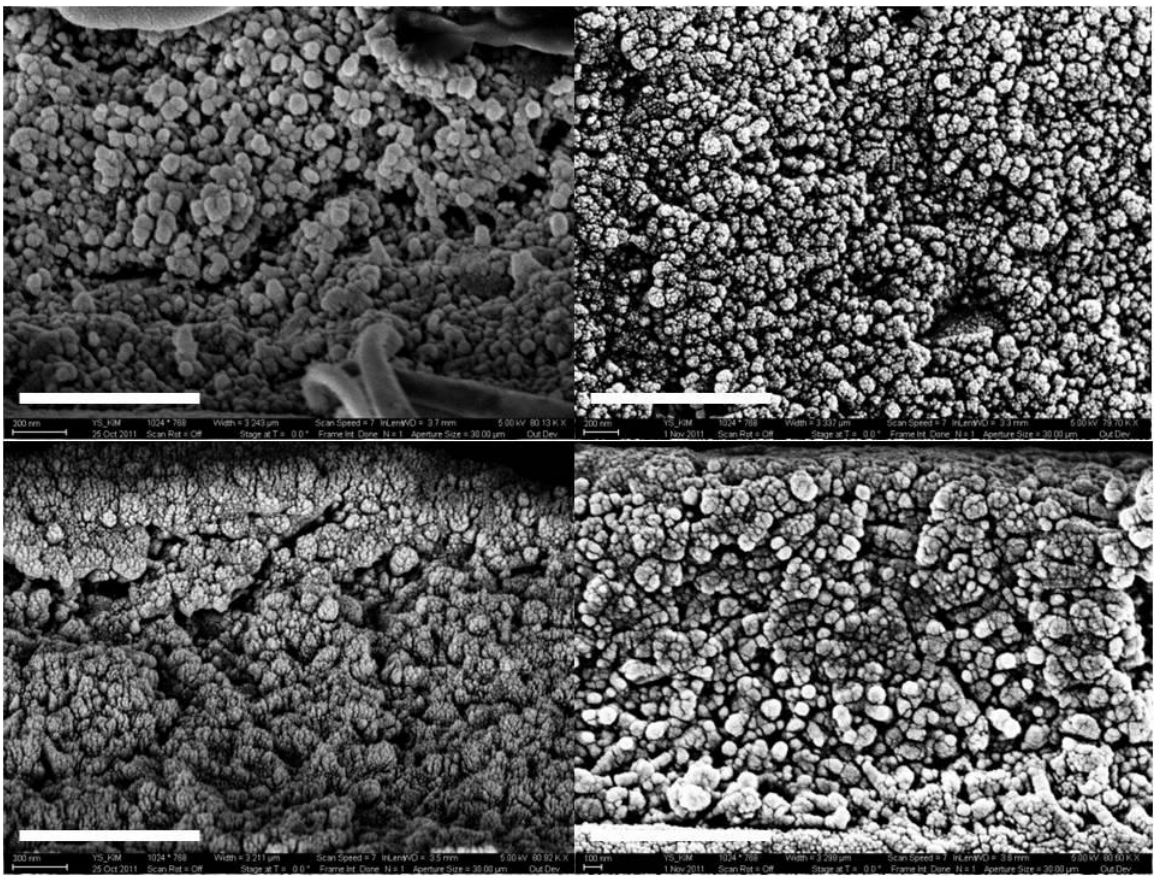

Figure 3.3 High-magnification cross-sectional SEM images of BT/P(VDF-*co*-HFP) nanocomposite films containing 50 and 120 nm BT particles with a volume loading of 50%, fabricated *via* spin or blade casting: BT50s (top left), BT50b (top right), BT120s (bottom left), and BT120b (bottom right). **(**scale bar 1 μm).

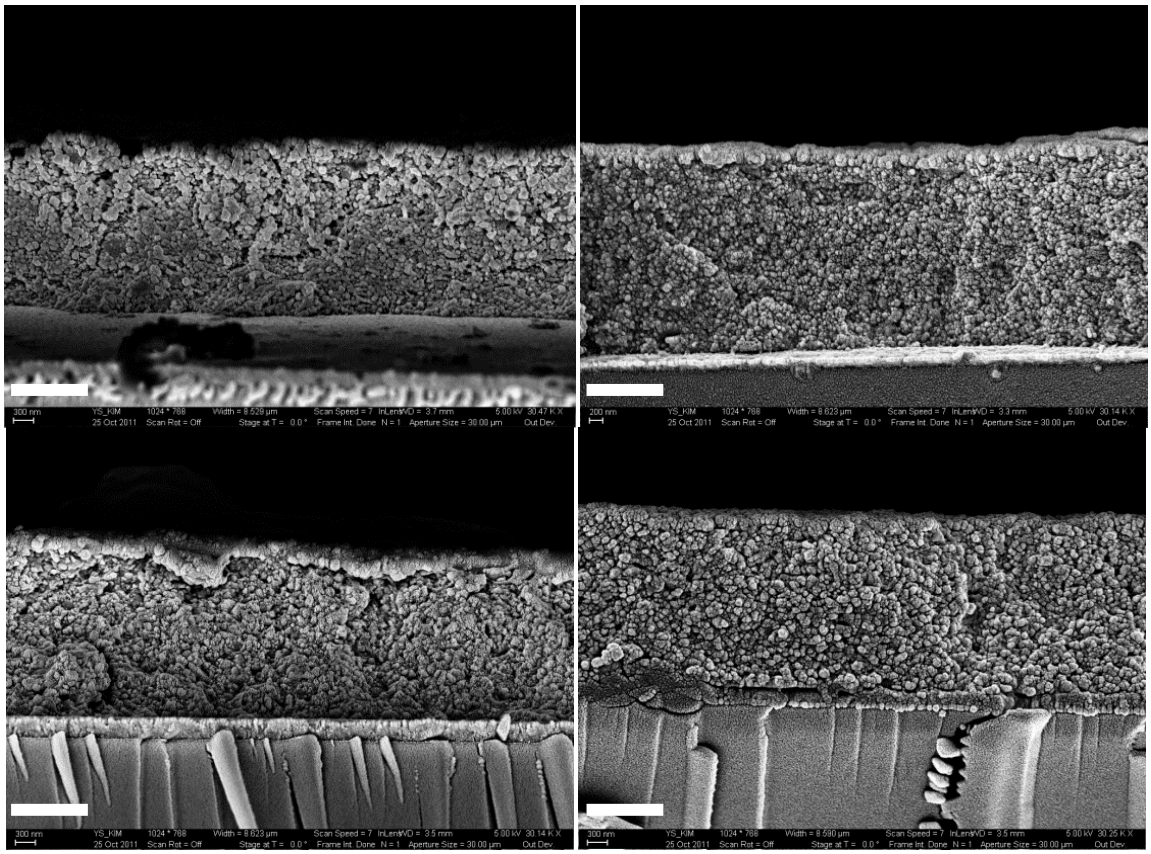

Figure 3.4 Low-magnification cross-sectional SEM images of BT/P(VDF-*co*-HFP) nanocomposite films containing 50 and 120 nm BT nanoparticles with a volume loading of 50%, fabricated *via* spin or blade casting: BT50s (top left), BT50b (top right), BT120s (bottom left), and BT120b (bottom right). **(**scale bar 1 μm).

The AFM images of the nanocomposite thin films are shown in Figure 3.5 and their root mean square (RMS) roughness values are summarized in Table 3.1. Although nanocomposite films containing 50 nm BT nanoparticles only indicate marginal improvement in surface roughness, the surface of 120 nm BT nanocomposites is greatly planarized by blade casting, leading to the reduction of surface roughness from 340 to 63 nm. The improved uniformity of film surface can be ascribed to a more uniform distribution of nanoparticles under blade casting, consistent with the cross-sectional SEM images of the films. The smoother surface in blade-cast films could suppress the development of non-uniform electric fields induced by surface topography and associated

premature electrical breakdown events, which likely contributes to the observed enhancement of breakdown strength in blade-cast films.

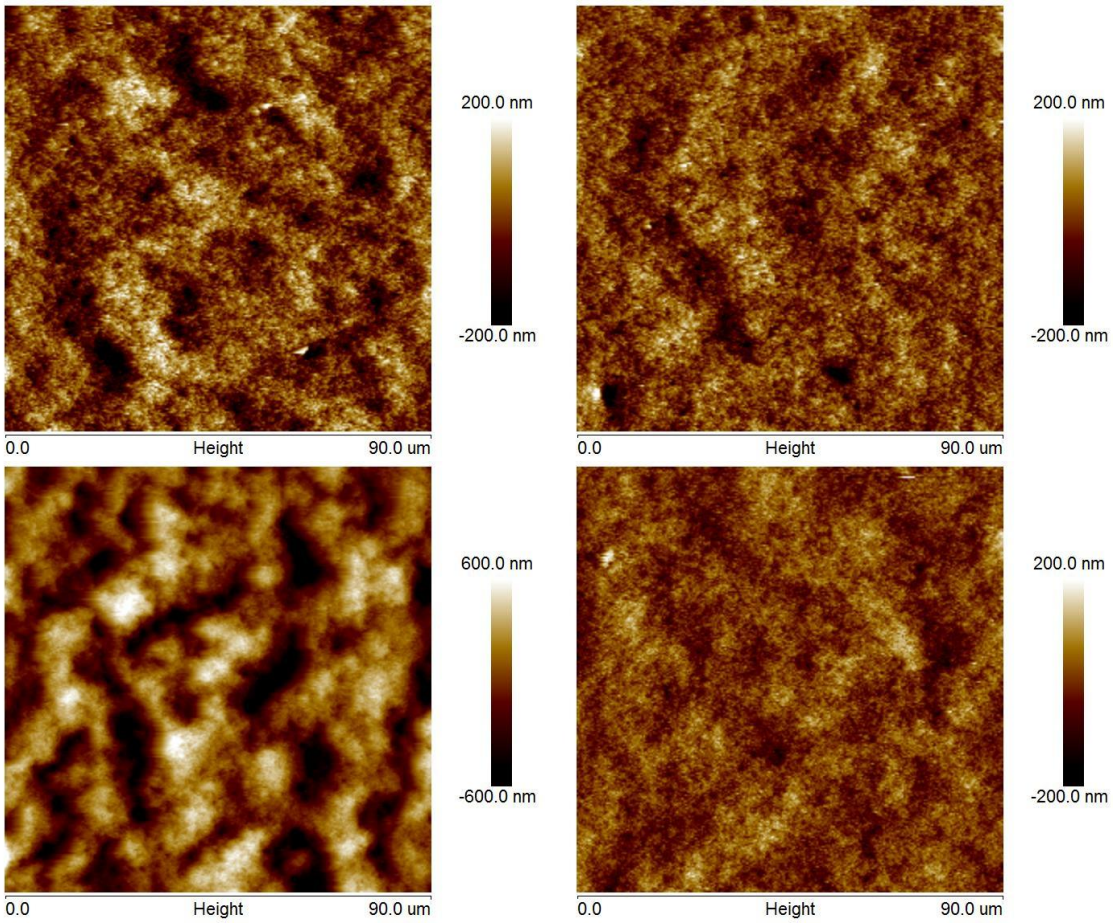

Figure 3.5 AFM images of BT/P(VDF-*co*-HFP) nanocomposite films containing 50 nm and 120 nm BT nanoparticles with a volume loading of 50%, *via* spin or blade casting: BT50s (top left), BT50b (top right), BT120s (bottom left), and BT120b (bottom right).

Table 3.1 Surface roughness and its standard deviation of BT/P(VDF-*co*-HFP) nanocomposite films from AFM images.

	50 nm BT, spin-coat	50 nm BT, blade-cast	120 nm BT, spin-coat	120 nm BT, blade-cast
RMS roughness (standard deviation) (nm)	62 (6)	50 (3)	340 (62)	63 (17)

X-ray diffractograms of nanocomposite films prepared by spin or blade casting are shown in Figure 3.6. The incorporation of BT nanoparticles in polymer matrix resulted in the suppression of peaks from PVDF crystals such as α and β phases, which actually appear at 18 to 20° in neat P(VDF-*co*-HFP) films in Fig. 3.6b.[94-96] Instead, a broad peak appears at two theta of 5.2° only in blade-cast nanocomposite films for both BT50 and BT120 (sharp peaks denoted by stars are from BT crystals), which is not seen in neat polymer films. It should be noted that XRD pattern of neat polymer film by blade casting in Fig. 3.6b shows much stronger peaks of PVDF crystallites at 18 and 20° whereas spin-coated film exhibits only a trace of them (sharp peaks denoted by stars are from ITO substrate). We attribute this difference to the lower rate of solvent evaporation in blade casting that may provide sufficient time for nucleation and growth of crystallites, thus possibly facilitating the formation of large crystalline domains, in contrast to the effect of rapid solvent evaporation in the case of spin coating. In this context, although the *d*-spacing of the broad peak in the blade-cast nanocomposite films is assigned as 1.7 nm, which is different than that of ordinary PVDF crystallites, we speculate that blade-cast nanocomposite films have crystalline domains, which maintain long range order that is more uniform in terms of size and distribution, as compared to those of the spin-coated nanocomposite films.

Further investigation of broad peaks at 5.2° using Scherrer equation (see Equation 3.1 below) reveals that the sizes of crystallites in blade-cast films are bigger than in spin-coated films (summarized in Table 3.2). We believe that larger crystalline domains in blade-cast films can be correlated with the increase of E_B as discussed earlier because with larger crystallite size the probability of breakdown events across the boundary of crystalline domains will be reduced.[97-99] Moreover, larger crystallites exhibit a tendency to act as charge trapping and scattering center that impede the transport of charge carriers, thus mitigating premature dielectric breakdown of nanocomposite films.[48, 100]

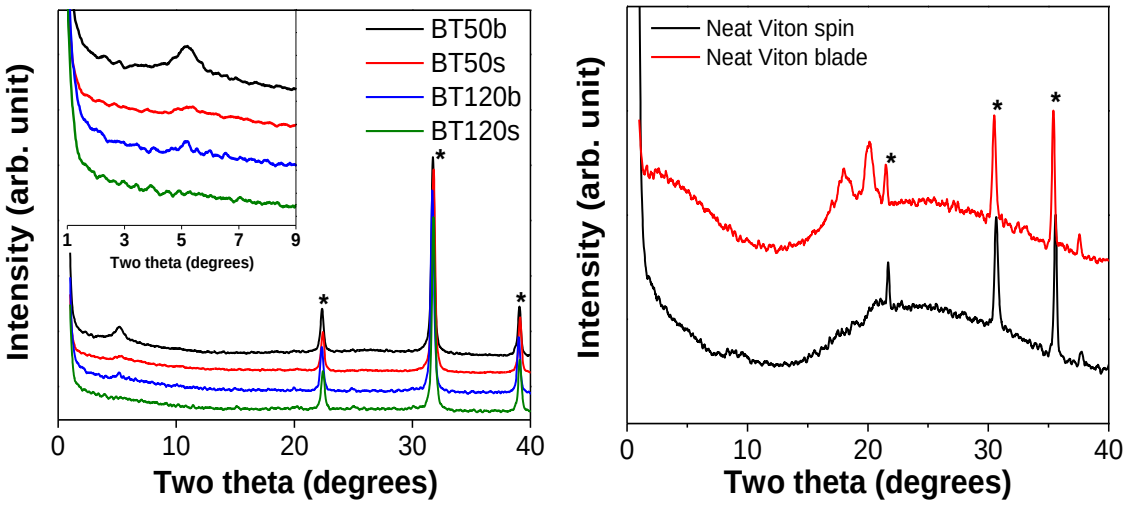

(a) (b)

Figure 3.6 X-ray diffractogram of (a) BT/P(VDF-*co*-HFP) nanocomposite films, (b) neat P(VDF-*co*-HFP) films prepared by spin or blade casting methods (stars denote peaks from (a) BaTiO3 for (001) and (100) at 22º, (101) and (110) at 31.5º, and (111) at 39º; (b) from ITO for (211) at 21.5º, (222) at 30.5º, and (400) at 35.5º). Number in the legend of Figure 3.6a denotes the size of BT particles used, followed by a letter indicating film preparation method (s for spin coating and b for blade casting)

Table 3.2 Coherence length for the polymer crystallites in BT/P(VDF-*co*-HFP) nanocomposite films calculated from low angle peaks after baseline correction using Scherrer equation.

	Coherence length (nm)	FWHM
BT50b	8.7	0.91 ± 0.02
BT50s	6.2	1.3 ± 0.05
BT120b	23	0.35 ± 0.03
BT120s	2.8	2.8 ± 0.17

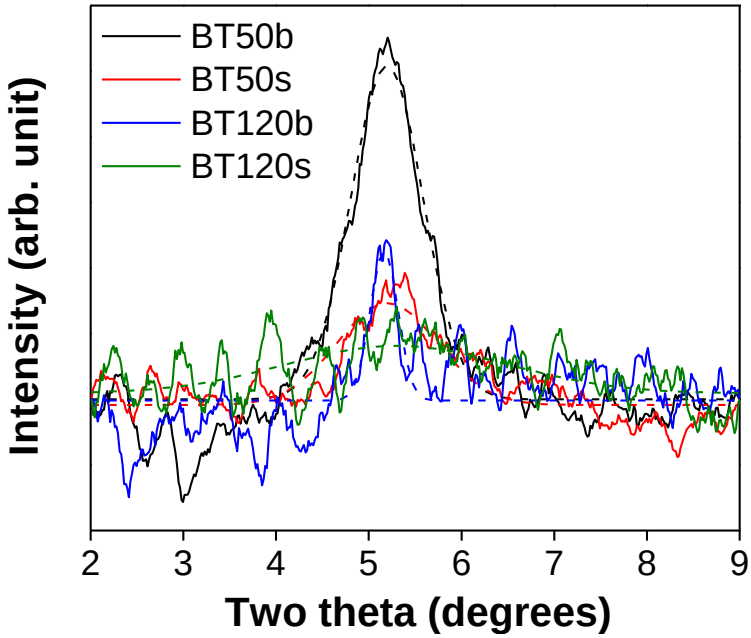

Figure 3.7 X-ray diffractogram of nanocomposite films at low angle shown on inset in Figure 3.6. Dashed lines represent Gaussian fits after baseline correction and their full width at half maximum (FWHM) are summarized in Table 3.2.

Scherrer equation is defined by,

$$L = \frac{0.9\lambda}{B\cos\theta} \qquad \text{Equation 3.1}$$

where L is coherence length, λ is the wavelength of x-ray, B is full width at half maximum, and θ is angular position of the peak.

3.5 Dielectric Properties

The frequency dependent permittivity and loss tangent of PFBPA-BT/P(VDF-*co*-HFP) nanocomposite films containing either 50 nm or 120 nm BT nanoparticles, prepared by spin and blade casting are compared in Figure 3.8. Because of the large permittivity of 120 nm BT nanoparticles, nanocomposites containing 120 nm BT nanoparticles (shown in red) exhibit higher effective relative permittivity of 40 (at 1 kHz) than 50 nm BT

nanocomposites (30 at 1 kHz). It was also observed that both the permittivity and loss tangent over the frequency range (100 to 1 MHz) were independent of processing method, *i.e.*, blade or spin casting. Figure 3.9 summarizes the permittivities and thicknesses of all four sets of nanocomposite films including their standard deviations (1σ). For convenience we denote the 50 nm BT nanocomposite film prepared by blade casting as BT50b (BT120s indicates 120 nm BT nanocomposite film prepared by spin coating). Thicknesses of all four sets of nanocomposite films were in the range of 3 ± 0.5 μm, in order to minimize the influence of thickness on the breakdown strength of dielectric films.[101]

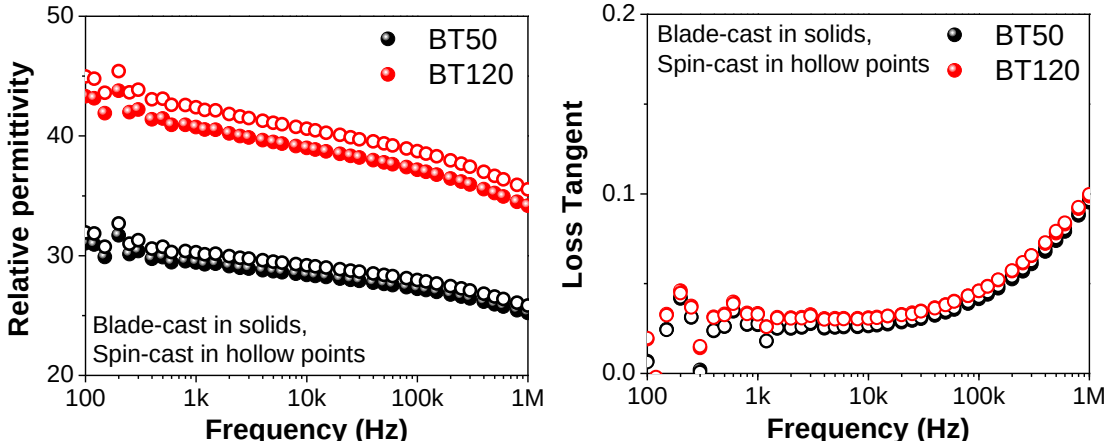

(a) (b)

Figure 3.8 Frequency dependent (a) permittivity and (b) loss tangent of PFBPA-BT/P(VDF-*co*-HFP) nanocomposite films. Data of blade and spin-cast films are shown in solid circles and hollow circles, respectively. Solid dots are behind hollow points in Figure 3.8b.

The E_B values of nanocomposite films were determined and analyzed by using Weibull analysis, which has been discussed in detail elsewhere.[48, 102] Briefly, the cumulative failure probability distribution (P_F) is expressed by Equation 3.2 below:

$$P_F(E) = 1 - exp\left[-\{(E-\gamma)/\alpha\}^{\beta}\right] \qquad \text{Equation 3.2}$$

where, E is the applied electric field, α is the scale parameter, β is the shape parameter or Weibull modulus, which represents the dispersion of E_B, and γ is the electric field below which no observable failure occurs. In this study, γ was set to zero. The cumulative probability of failure (% CDF) in nanocomposite films is shown in Figure 3.10 as a function of electric field. The slope of % CDF is the Weibull modulus, β, and the characteristic breakdown strength, E_{BD}, is defined as the electric field at which the failure probability is 63.2%.

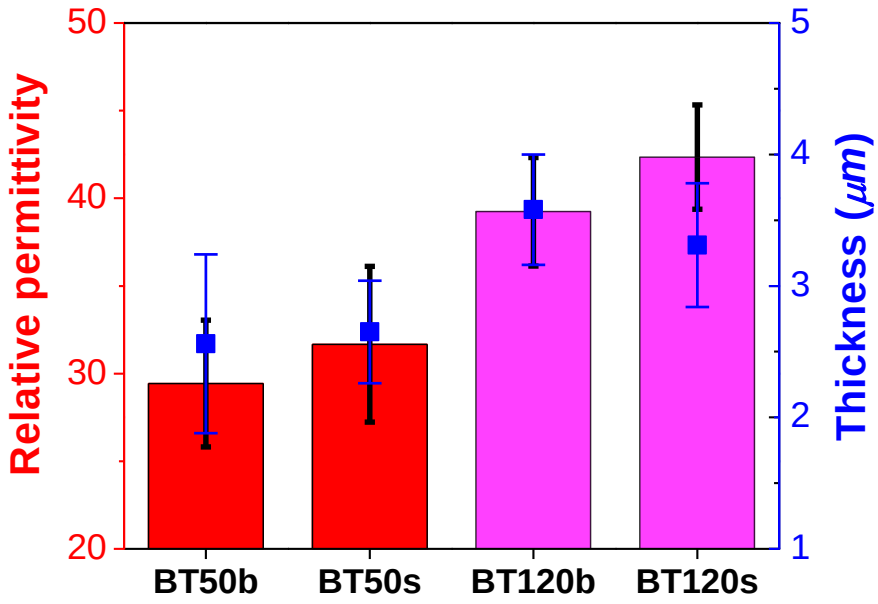

Figure 3.9 Relative permittivities and thicknesses of nanocomposite films containing either 50 nm or 120 nm BT nanoparticles with a volume loading of 50%, fabricated by either blade or spin casting. The error bars represent the standard deviations (1σ) of relative permittivity and thickness.

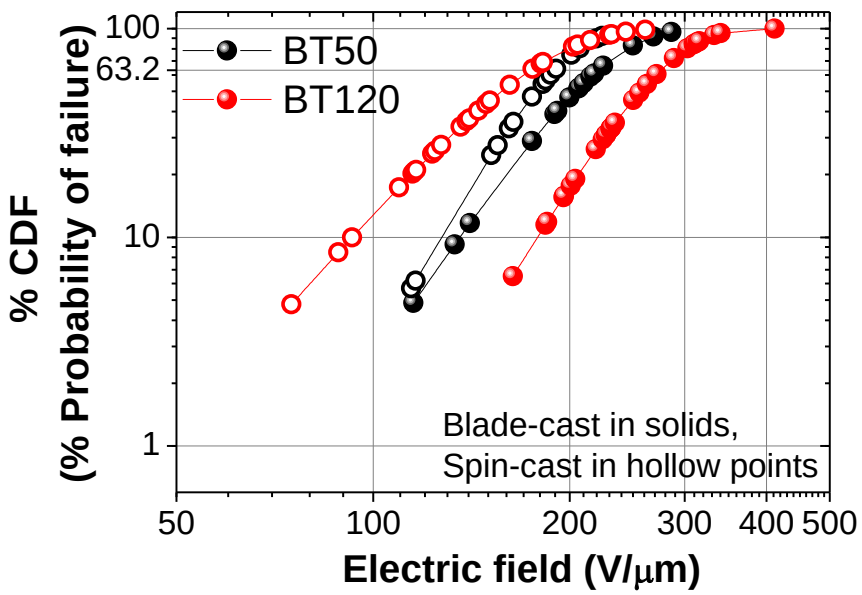

Figure 3.10 The % cumulative distribution functions (% CDF) of nanocomposite films containing either 50 nm or 120 nm BT nanoparticles with a volume loading of 50%, fabricated by either blade or spin casting, as a function of electric field.

Figure 3.11 summarizes the E_B and β of nanocomposite films, which were determined from the Weibull analysis as shown in Figure 3.10. Blade-cast nanocomposite films with both 50 and 120 nm BT particles show an increase in E_B compared to that of spin-cast films. The enhancement of E_B *via* blade casting is more dramatic in 120 nm BT nanocomposites, which showed an increase of 60%. This gain is attributed to the improved morphology, a more uniform distribution of nanoparticles, reduced surface roughness of thin films, and larger crystalline domains in blade-cast films as will be discussed below. Although Weibull modulus of nanocomposite films does not follow the same trend that was observed in E_B, β of blade-cast 120 nm BT nanocomposites does exhibit a moderate increase.

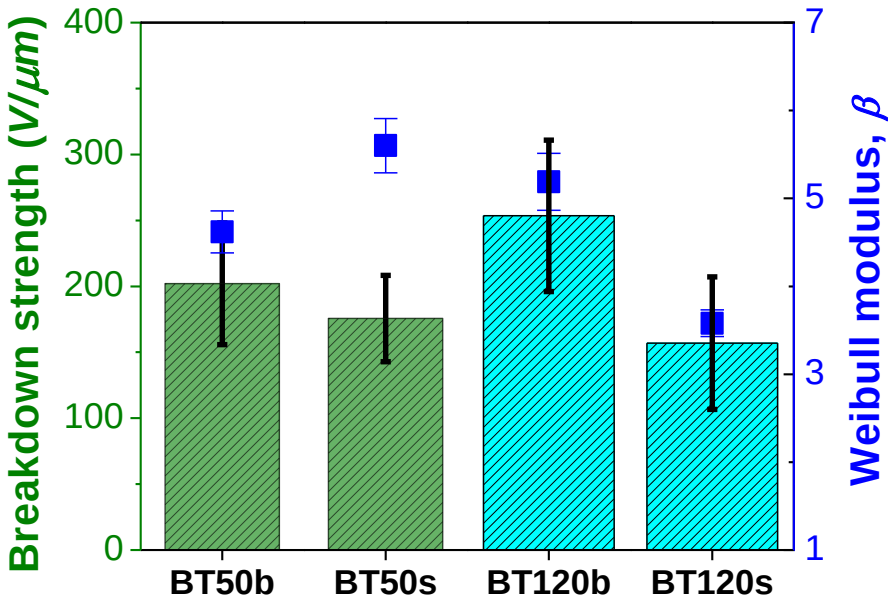

Figure 3.11 Breakdown strength (E_B) and Weibull modulus, β, of nanocomposite films containing 50 and 120 nm BT particles with a volume loading of 50%, fabricated by either blade or spin casting. The error bars of breakdown strength were obtained from measurements of at least 15 devices. The Weibull modulus β and its error bar were determined by Weibull analysis.

3.6 Energy Storage Characteristics

To determine the maximum extractable energy density (U_{max}) of nanocomposite thin films, we have performed charge-discharge (C-D) and polarization-electric field (P-E) measurements, which were conducted under pulsed and ramped field conditions, respectively. As shown in Figure 3.12, blade-cast nanocomposite films consisting of 50 nm BT give U_{max}^{CD} and U_{max}^{PE} (maximum extractable energy densities from C-D and P-E, respectively) values of ~7 J/cm^3, which are nearly twice larger than those of spin-cast films. The U_{max} for nanocomposite films bearing 120 nm BT is also increased from 2.5 to 4.5 J/cm^3 and 1.5 to 5.5 J/cm^3 from C-D and P-E methods respectively. Although the field strength at which the maximum energy density, U_{max}, is obtained is different,

U_{max} of nanocomposite films does not show a significant dependence on the measurement method (C-D or P-E) for the same batch of nanocomposite films, *i.e.*, the same size of BT and the same processing method used. We attribute this difference to the longer charging time for C-D measurements, which is around a few hundred milliseconds. The lower breakdown strength of nanocomposite films in C-D can also be explained by larger electrical stress when the dielectric film is subjected to a pulsed electric field.

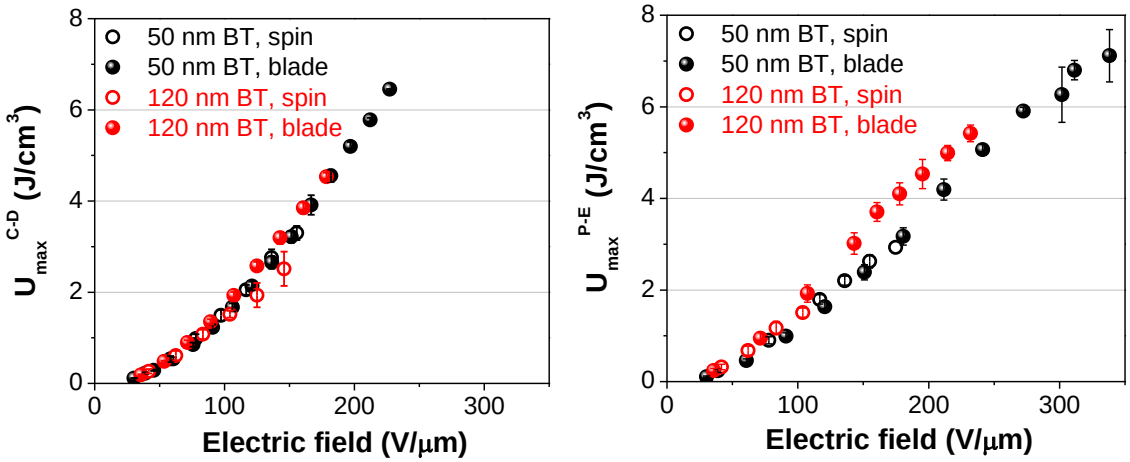

(a) (b)

Figure 3.12 Extractable energy densities of BT/P(VDF-*co*-HFP) nanocomposite films determined from (a) charge-discharge (C-D) and (b) polarization-electric field (P-E) methods. The error bars represent the standard deviations (1σ) of extractable energy density.

The enhancement of U_{max} in blade-cast nanocomposite films (for both 50 and 120 nm BT particles) is primarily due to the increased breakdown strength, which was shown earlier in Figure 3.11. It is interesting to note that U_{max} of nanocomposite films are limited mainly by the breakdown strength of the films in the C-D measurement. In the P-E method, however, nanocomposite films containing 120 nm BT particles yielded higher U_{max}^{PE} than the 50 nm BT nanocomposites throughout the range of electric fields investigated in this study (shown in Figure 3.12b). It should be noted that the enhancement of U_{max}^{PE} in nanocomposite films of 120 nm BT particles is only observed in

blade-cast films and not in spin-coat films. We believe that the very large RMS roughness (340 nm) of spin-cast films with 120 nm BT negates any enhancement.

The effect of BT nanoparticle size on the energy density of nanocomposite films is further investigated by comparing P-E loops of blade-cast films. In general, the crystal structure of BT nanoparticles transforms from cubic to tetragonal when the size of BT increases, providing greater relative permittivity due to the spontaneous polarization from the displacement of Ti ions.[53, 103] In Figure 3.13, the slope of P-E loops, which is proportional to the permittivity of dielectric material,[84] in nanocomposite films with 120 nm BT is steeper than films with 50 nm BT, suggesting an increased tetragonal phase content of the BT particles incorporated into the polymeric matrix. Although higher permittivity leads to larger U_{max}^{PE} in nanocomposites with 120 nm BT, the lower breakdown strength limits U_{max}^{PE} to 5.5 J/cm^3 at 240 V/μm, which is still 10% higher than nanocomposites with 50 nm BT at the same field strength. P-E loop of neat P(VDF-*co*-HFP) film is also laid out to show the effect of BT incorporation on the ferroelectric response of nanocomposite films.

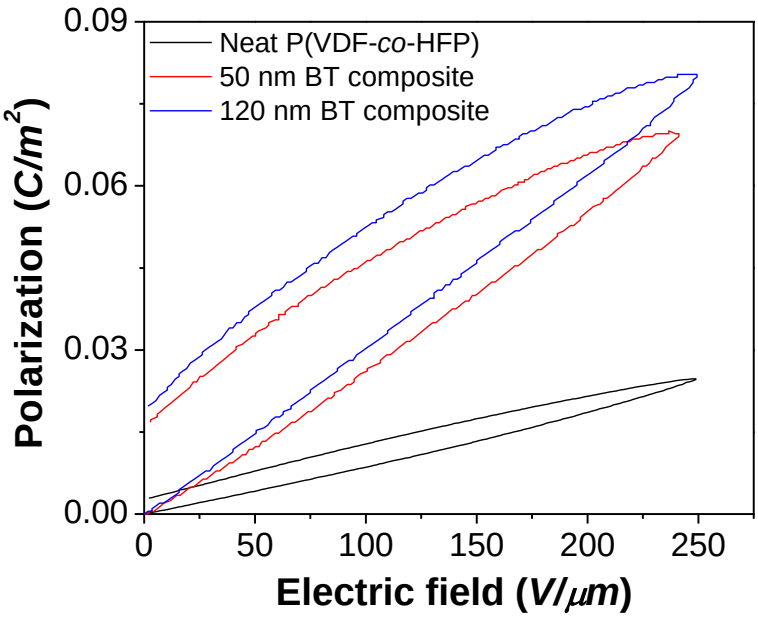

Figure 3.13 P-E loops of blade-cast BT/P(VDF-*co*-HFP) nanocomposite films at ~250 V/μm containing 50 volume% of either 50 nm or 120 nm BT nanoparticles. Neat P(VDF-*co*-HFP) is also laid out to show the effect of BT incorporation on the hysteresis of P-E loops. Unlike neat polymer matrix, P-E loops of nanocomposites exhibit significantly increased remnant polarization, which is due to ferroelectric response of BT nanoparticles.[104]

Additional P-E loops of nanocomposite films of both 50 nm and 120 nm BT particles are presented in Figure 3.14. The overall shape of P-E loops is similar in that the loops become wider as the electric field increases, which is also reflected in the reduced energy extraction efficiency shown in Figure 3.15. The extraction efficiency decreases to 60% at ~150 V/μm, for both spin- and blade-cast films, and the blade-cast films consistently show extended performance to higher fields, while extraction efficiency is reduced and the P-E loops widened. The widening of P-E loops, which is directly related to the reduction in extraction efficiency, is attributed to charge injection and/or conduction in these dielectric films.[84] This trend discussed above suggests that blade-cast films are more resistant to injection/conduction-induced catastrophic breakdown, which we attribute to the reduced porosity, the more uniform distribution of nanoparticles, and larger crystalline domains in blade-cast films. Finally, it is worth noting that blade

casting and related processing methods are quite scalable for the fabrication of large area nanocomposite dielectric thin films.

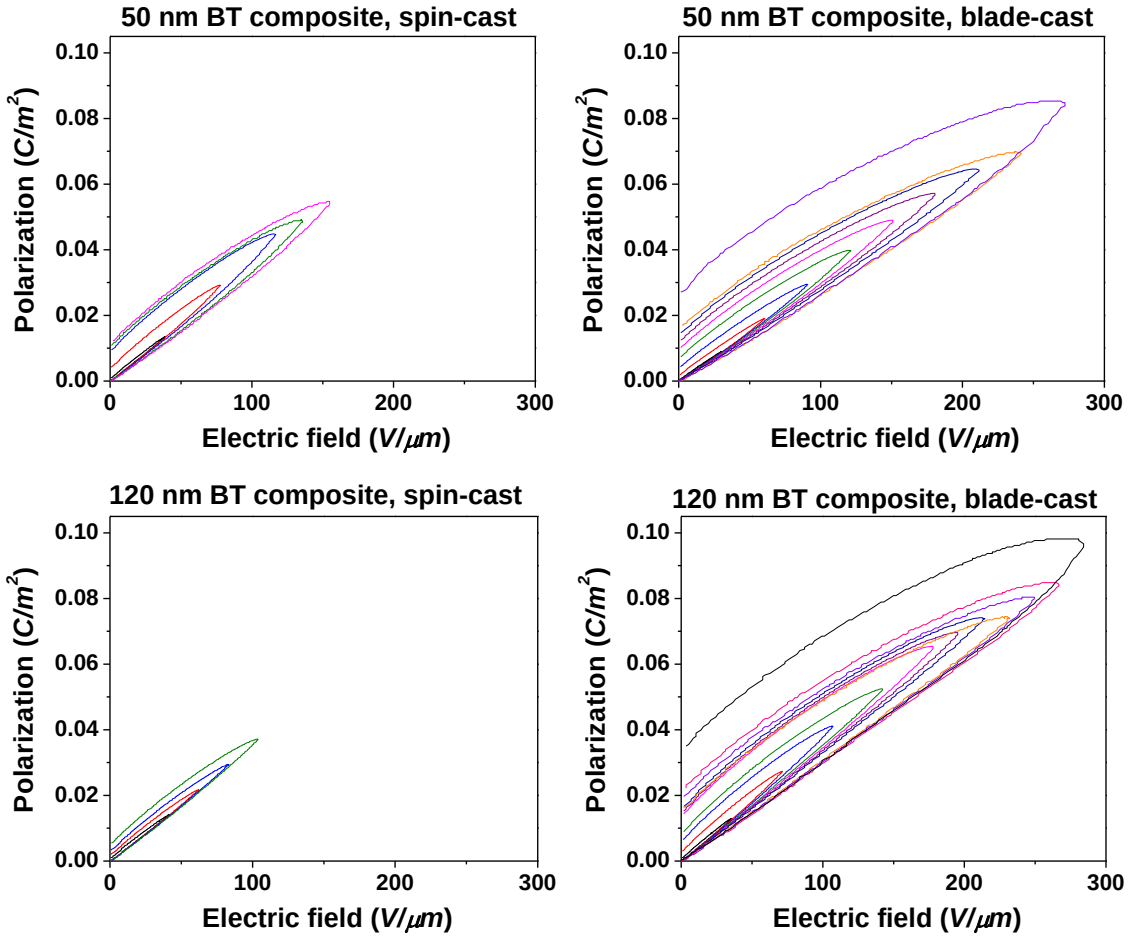

Figure 3.14 Unipolar P-E loops of BT/P(VDF-*co*-HFP) nanocomposite films.

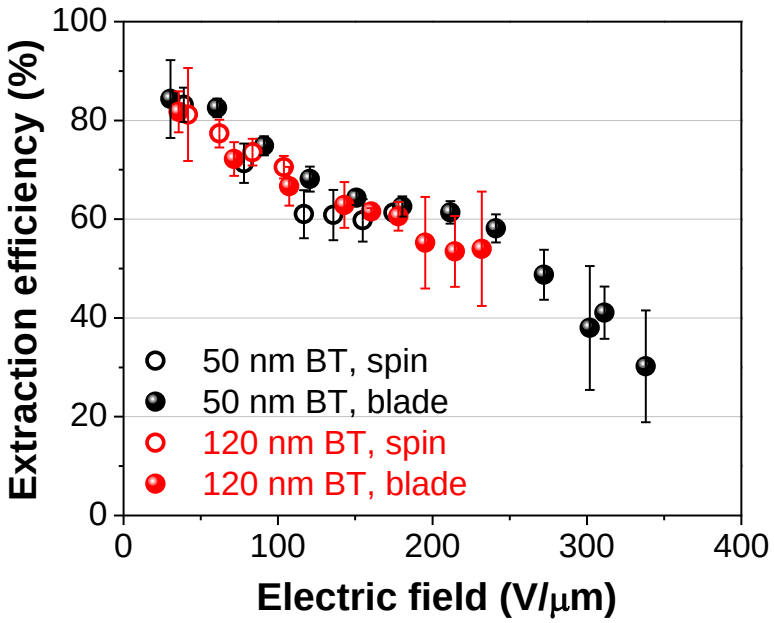

Figure 3.15 Energy extraction efficiency of BT/P(VDF-*co*-HFP) nanocomposite films determined from polarization-electric field (P-E) method.

3.7 Conclusions

It was shown that the blade-cast thin films obtained from nanocomposite solutions consisting of surface-modified BT nanoparticles in P(VDF-*co*-HFP) yield an extractable energy density of ~7 J/cm^3, which is larger by a factor of two relative to spin-coated films. The improvement of extractable energy density is associated primarily with the increase of the dielectric breakdown strength, which is attributed to reduced porosity, a more uniform distribution of nanoparticles, and larger crystalline domains obtained *via* blade casting. Nanocomposite films with 120 nm BT nanoparticles lead to higher permittivity but the maximum energy density is compromised by the reduced breakdown strength of these films. The increased breakdown strength and extractable energy density in blade-cast thin film capacitors suggests the utility of using blade casting for making thin films for dielectric energy storage and pulsed power applications, as well as in solution processed thin-film electronics as a methodology of film fabrication.

CHAPTER 4

DIELECTRIC FILM CAPACITOR BASED ON CYANOALKYLATED SILICATE SOL-GELS

4.1 Basics of Sol-Gel Processing

As introduced in the section 1.3.3, sol-gel processing is defined by the formation of interconnected three dimensional network, a *gel*, with submicron pores and polymeric chains, whose length scale ranges up to micrometer, from the dispersions of colloidal particles, *sols*, in a liquid.[74] A typical sol-gel reaction comprises simultaneous hydrolysis and condensation of sol-gel precursors followed by crosslinkings, leading to the formation of 3-D networks. The structure of a gel ranges from well-ordered lamellar structure to polymeric networks with covalent link and disordered physical entanglement.

The microstructure of sol-gel materials is strongly dependent on processing conditions, which render different physical properties such as porosity, pore size distribution, transparency, and density of resulting sol-gel films.[105] For silica-based sol-gel materials, the general trend related to catalysis and solvent ratio, which are the most important factors governing the microstructure of sol-gel materials, is that acid-catalyzed hydrolysis with low H_2O to Si ratio produces weakly branched polymeric networks, whereas base-catalyzed hydrolysis with large H_2O to Si ratio produces highly branched colloidal particles.[106] Depending on the morphology of sols, whether they form weakly or highly branched polymeric network, the physical properties of gels vary widely.

The effect of catalysis on the hydrolysis and the condensation of sols, which are the first and most important stage in sol-gel reaction, can be explained by the charges on the transition state. In acid-catalyzed hydrolysis, a positively charged transition state is stabilized by electron donating groups. Because alkoxy groups are more electron

donating than hydroxyl groups when the more alkoxy groups are converted to hydroxyl groups, the less stable the transition state becomes. Therefore, the condensation reaction between Si-OH and other alkoxy groups dominates sol-gel reaction, thereby creating linear polymeric networks. The entanglement of these linear chains leads to homogeneous and dense gels with relatively small pores.

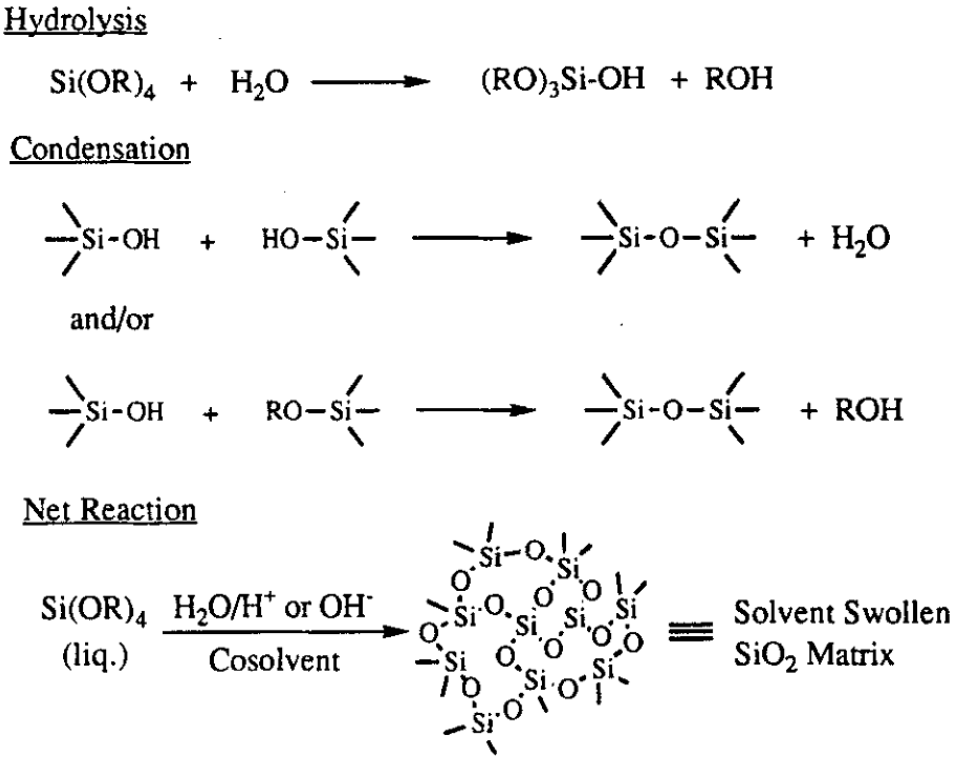

Scheme 4.1 The general sol-gel reaction scheme involving the hydrolysis and the condensation of tetraalkyl orthosilicates in the presence of co-solvents to form three-dimensional SiO_2 networks as solvent-swollen gels. Reproduced with permission.[107] Copyright © 1993 Verlag GmbH & Co. KGaA, Weinheim

On the other hand, in base-catalyzed hydrolysis, a negatively charged transition state is stabilized by electron withdrawing groups, so that the more alkoxy groups are converted to hydroxyl groups to make the transition state more stable. Accordingly, the fully hydrolyzed species undergo rapid condensation reaction and thus highly branched particulate sols are formed. The entanglement of these branched particulates leads to less dense gels with relatively large pores. It should be noted that because the reverse

conversion of hydroxyl groups to alkoxy groups stabilizes the positively charged transition state, esterification reaction is more likely to happen in acid-catalyzed hydrolysis than base-catalyzed system.

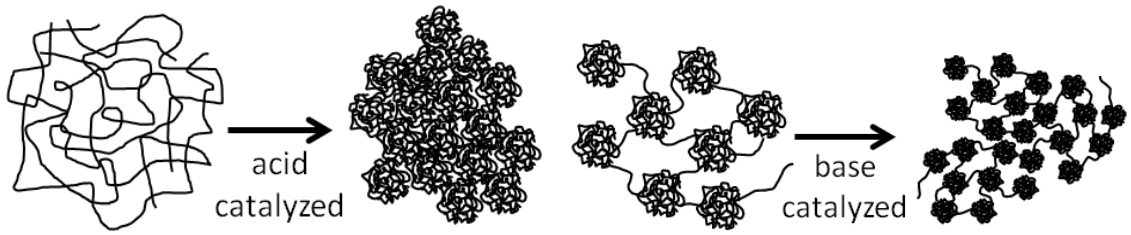

Figure 4.1 A schematic illustration of sol-gel structures catalyzed either by acid or base. Linear polymeric networks leads to more dense and less porous structure (left), whereas branched polymeric networks lead to less dense and more porous structure (right).

Brinker *et al*. reviewed several factors that affect the microstructure of sol-gel films, in particular, porosity.[108, 109] The factors involved 1) the packing of precursor species during gelation, 2) the condensation rate of sols, 3) the balance of shear and gravitational forces during film formation, and 4) the magnitude of capillary pressure during drying.

Many examples for the microstructural control of sol-gel films can be found in the literature. Nitta *et al*. reported spin-coated sol-gel films with high porosity (>70%) and low dielectric constant (1.4 – 2.2).[110] To generate highly porous and mechanically stable sol-gel films, they utilized two step catalyses (acid catalysis followed base catalysis) and saturated atmosphere during spinning and aging to prevent the shrinkage of porous sol-gel structure. Prakash et al. produced aerogel films with 98.5% of porosity by introducing trimethylchlorosilane groups that enabled the silica gel to undergo reversible shrinkage during drying.[111]

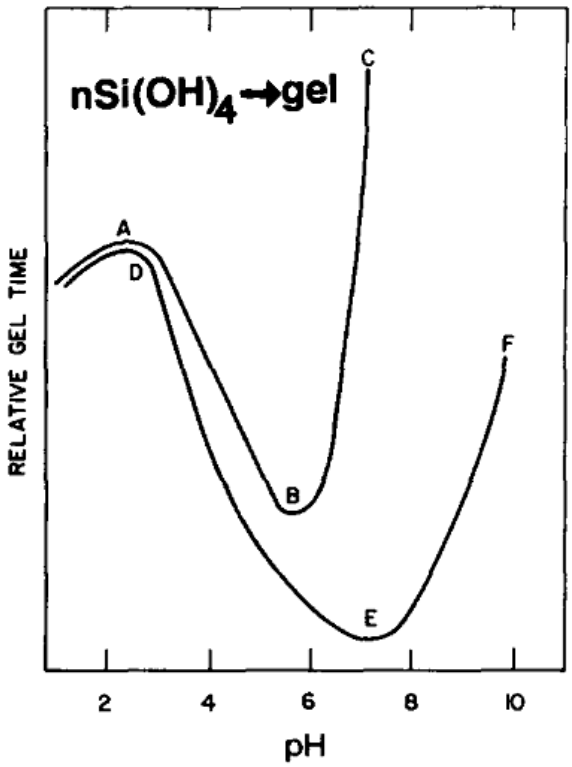

Figure 4.2 The effect of pH on the gelation time of silica sols. Curves A-C sols in the absence of sodium salts; D-F in the presence of sodium salts. Reproduced with permission.[106] Copyright © 1988, Elsevier

In brief, the microstructure of silica sol-gel materials is controlled by processing variables including catalyst, solvent, film deposition method, and drying procedure. Particularly, understanding the structure-property relationships in polar sol-gel materials would provide many potential opportunities in electrical applications.

4.2 Materials and Preparation of Sol-gel Films

Sol-gel precursors of 2-cyanoethyltrimethoxysilane (CNETMS), tetraethyl orthosilicate TEOS), 2-cyanoethylmethyldimethoxysilane (CNEMDMS), and 3-cyanopropyltriethoxysilane (CNPTES) were obtained from Gelest and used as received. The chemical structures of these precursors are shown in Figure 4.3. All the solvents and

chemicals purchased from Sigma-Aldrich (methanol, 2-methoxyethanol, 0.1 N hydrochloric solution) were reagent grade and used without further purification.

The typical procedure of sol-gel film preparation is as follows: 1) 1 g of sol-gel precursor is mixed with 0.5 g of solvent (methanol or 2-methoxyethanol) and 0.5 g of aqueous solution containing catalyst. The mixture is stirred overnight at room temperature. The resultant sol-gel solution is then placed on pre-cleaned conductive substrates (either aluminum(Al)-coated glass substrates or indium tin oxide (ITO) coated glass substrates) and subjected to spinning. The thickness of sol-gel film is controlled by employing different spin speeds. The as spun films on ITO substrates are stored at room temperature in a closed environment overnight and subsequently baked at the temperatures up to 130 °C for 3.5 hours. For films on Al-coated substrates, as spun films are directly subjected to baking under the same thermal condition for films on ITO substrates.

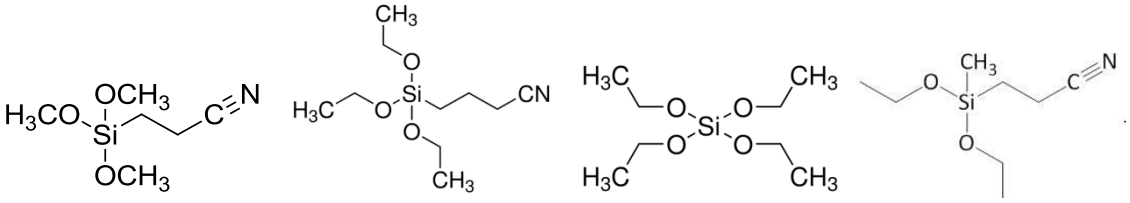

Figure 4.3 Chemical structure of sol-gel precursors. (from left to right) 2-cyanoethyltrimethoxysilane (CNETMS), 3-cyanopropyltriethoxysilane (CNPTES), tetraethyl orthosilicate (TEOS), and 2-cyanoethylmethyldimethoxysilane (CNEMDMS).

4.3 Sol-gel Film Capacitor Based on 2-Cyanoethyltrimethoxysilane (CNETMS)

The organic-inorganic hybrid sol-gel approach is a promising method for the formation of dielectric films, as it offers relatively mild reaction conditions for the synthesis of composite materials with molecular level control of composition and solution-based processing of films.[74, 107] One avenue to develop sol-gel hybrid materials with high

permittivity is to incorporate highly polarizable moieties as a pathway to high energy density materials. Recently, Kwon et al. reported on organic-inorganic sol-gel hybrids in which surface-modified $BaTiO_3$ nanoparticles were incorporated into organic-inorganic sol-gel hybrid matrices.[75] Their sol-gel hybrids were formed by hydrolysis and the condensation of trimethoxysilane with pendant acrylate groups, which were polymerized following condensation. 4,4'-(hexafluoroisopropylidene)diphenol was also included to impart a moderate dipole moment and electronic polarizability. The hybrid sol-gel composites with 65 and 400 nm $BaTiO_3$ particles showed relative permittivities of ~25 and ~62, respectively, at 1 KHz. The dielectric strength of the composite with 65 nm $BaTiO_3$ particles was reported to be 263 V/μm, quite similar to poly(vinylidene fluoride-*co*-hexafluoropropylene)-$BaTiO_3$ nanocomposites.[48]

Another pathway to high permittivity hybrid sol-gel films would be to incorporate compact dipolar groups tethered to a trimethoxysilane precursor via a flexible linkage, which could provide for a dipolar orientation polarization mechanism. An example of such organic sol-gel hybrid materials was reported by Maruyama, et al. based on xerogel films prepared from blends of trialkoxysilanes, tetraalkoxysilanes and a trialkoxysilane with a pendant cyanoalkyl-moiety, which showed large relative permittivity in the range of 22 to 27 and small loss tangent, along with good thermal and mechanical stability.[76]

In this section, the formation of neat sol-gel films of 2-cyanoethyltrimethoxysilane (CNETMS) is demonstrated and a detailed study of their morphology, electronic and dielectric properties, which are crucial to evaluate the potential for energy storage applications, is presented. The polarization response and mechanism of CNETMS xerogels films are examined *via* dielectric spectroscopy and field dependent polarization (P-E) measurements, which show narrow hysteresis, negligible remnant polarization, and linear dielectric-like response, suggesting the potential of CNETMS sol-gel films as linear dielectrics for pulsed-power and energy storage applications.

4.3.1 Chemical Structure and Morphology

Thin films of CNETMS were characterized by FT-IR and XRD techniques. The characterizations were performed using CNETMS solid that was obtained by removing CNETMS film from a substrate and grinding it to obtain the powder form. The KBr pellet method was used to take FT-IR spectrum of CNETMS shown in Figure 4.4a. The FT-IR spectrum of CNETMS clearly shows the cyano stretching vibrations in the region of 2250 cm^{-1}. The infrared absorptions in the region of 1000-1200 cm^{-1} and that at 2900 cm^{-1} are assigned to the Si-O-Si and C-H vibrational modes respectively of the hybrid network.[112] The powder XRD data of the CNETMS in Figure 4.4b (measured by (PANalytical, X'Pert PRO Alpha-1 diffraction system and copper K-alpha source) exhibit a weak diffraction peak at a 2θ value of 8°, suggesting the presence of features with a characteristic *d*-spacing of ~1 nm in the otherwise primarily amorphous material. The dominance of amorphous structure of the CNETMS xerogels film suggests that this sol-gel material may have a loosely-packed random structure, which is a favorable condition for cyano groups to reorient themselves along the direction of applied electric field. The appearance of crystalline domains in the sol-gel film can be attributed to the partial ordering of CNETMS in the solid state (aided by free volume from porous networks) due to the orientation and alignment of the cyano groups, which have been shown in polymer matrices containing the mixture of cyano resins and non-cyano resins as well as in copolymers of cyano resins.[1]

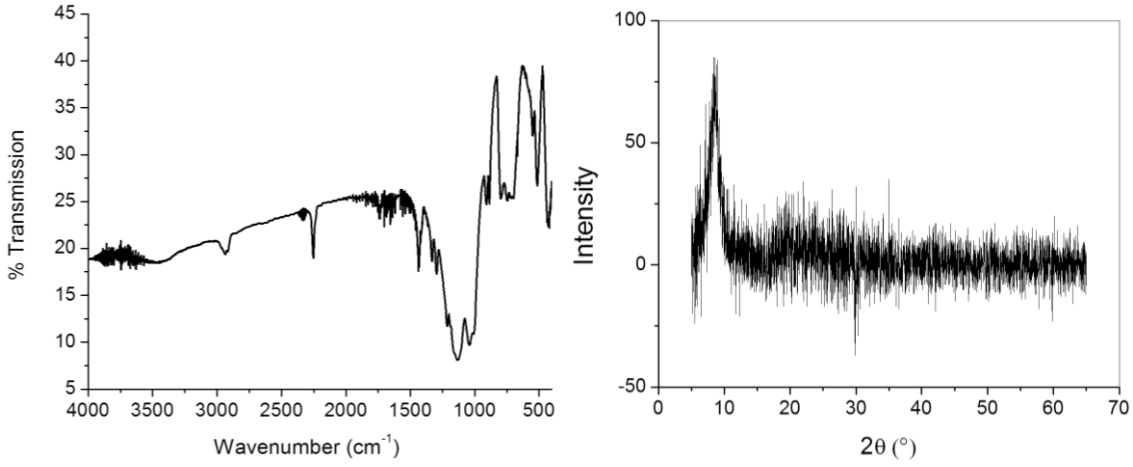

a) b)

Figure 4.4 a) FT-IR transmission spectrum of CNETMS solid (using KBr pellet method) obtained from sol-gel CNETMS films. b) X-ray diffraction spectrum of CNETMS solid powder obtained from CNETMS films.

It is worthwhile to compare this sol-gel material bearing cyano groups to its polymeric analog polyacrylonitrile (PAN). In XRD diffractogram of powder sample of PAN shown in Figure 4.5, the presence of sharp reflections superimposed over diffuse scattering in these diffraction patterns is characteristic of crystalline and amorphous phases of conventional semicrystalline polymers.[40] Although CNETMS and PAN have one cyano group in common per repeating unit or monomer, the difference in crystallinity between CNETMS sol-gel and polymeric PAN may be attributed to the flexibility of chains, which is presumably larger in hydrocarbon bonds in PAN than crosslinked siloxanes in CNETMS sol-gel. Despite of larger crystallinity, PAN exhibits a relative permittivity of only 5.5 (at 1 kHz), which suggests that crystalline domains in PAN is organized in such a way that the net sum of permanent dipole moment of cyano groups (individual dipole moment of 3.5 Debye) is substantially compensated, leading to very limited dielectric response.

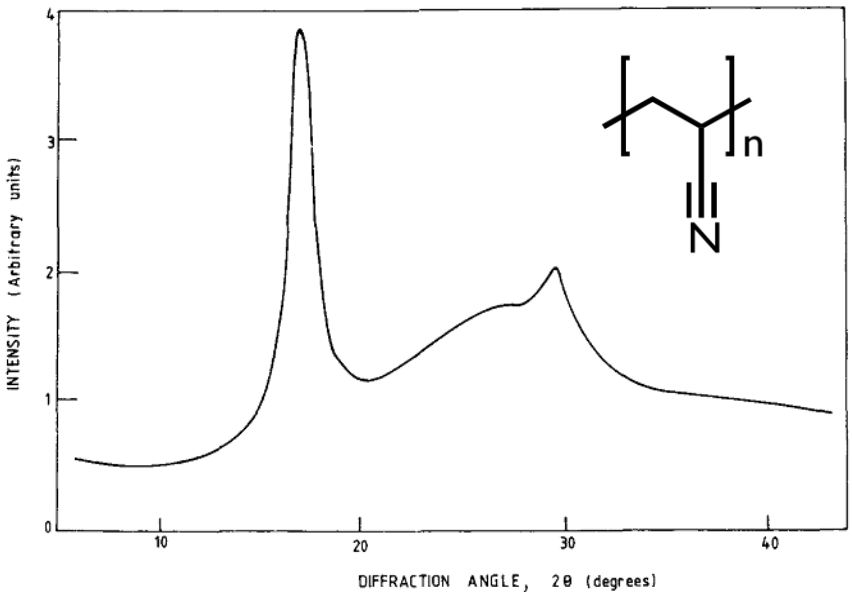

Figure 4.5 X-ray diffraction pattern of powdered sample of polyacrylonitrile (PAN) with overlaid chemical structure. Reproduced with permission.[40] Copyright © 1980 John Wiley & Sons, Inc.

The morphology of CNETMS films was characterized using AFM, top surface and cross sectional SEM, and cross sectional transmission electron microscopy (TEM) imaging. AFM image shown in Figure 4.6 of CNETMS films exhibit a very smooth surface with an RMS roughness of 0.27 nm. SEM images (Figure 4.7) indicate apparent pore sizes in the CNETMS films with mean values of the order of ~10 nm, as observed by top-surface and freeze-fractured cross sectional samples. High-resolution TEM images (Figures 4.8 and 4.9) of prepared cross sections of the CNETMS films showed a dense morphology with features that were < 1 nm in size, which is consistent with the feature size observed in XRD analysis. While we are not certain about the origin of the larger features in the SEM images, it is possible that these features result from stresses during film processing or the fracturing process used to obtain the cross sectional SEM images.

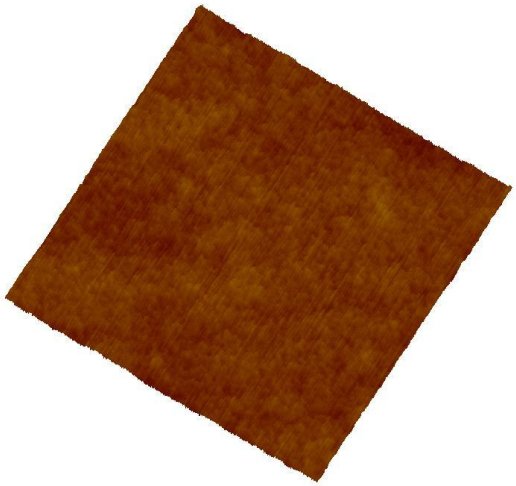

Figure 4.6 AFM image of a 3.5 µm thick CNETMS film (z scale is 10 nm and scan size is and 5 µm × 5 µm).

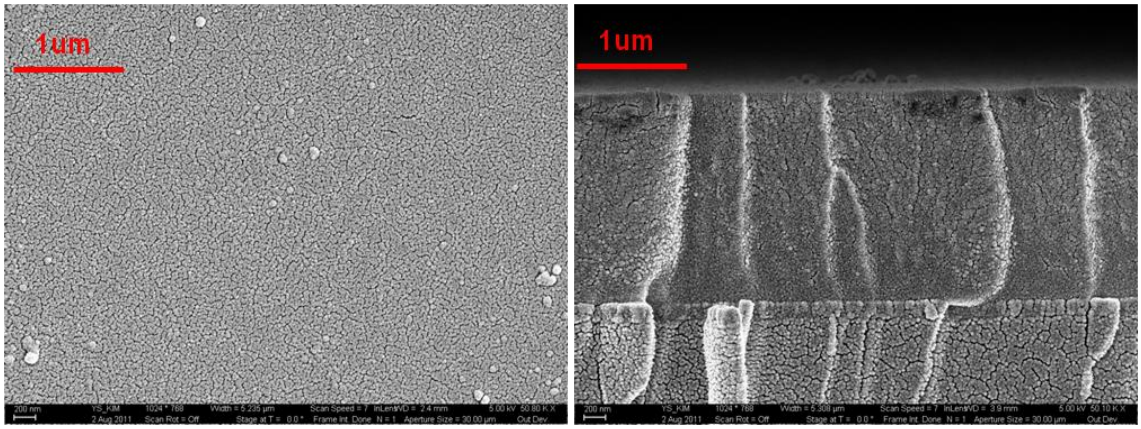

a) b)

Figure 4.7 a) Top surface and b) cross-sectional SEM images of 2.6 µm thick CNETMS film. CNETMS sol-gel is the thickest layer in Figure 4.7b.

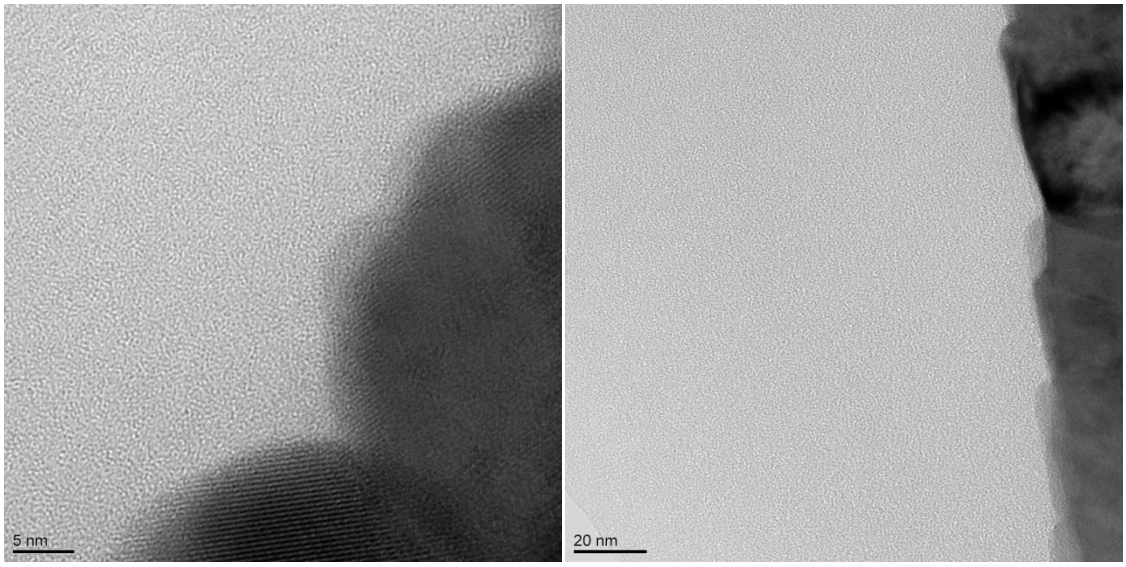

Figure 4.8 Cross-sectional TEM images of 1.3 μm thick CNETMS film on indium tin oxide coating, showing a relatively dense, homogeneous morphology: (left) 5 nm scale bar, (right) 20 nm scale bar. An upper limit on the size of pores in the material appears to be ~ 1 nm. The ITO electrode appears as the dark phase on the right side of the images.

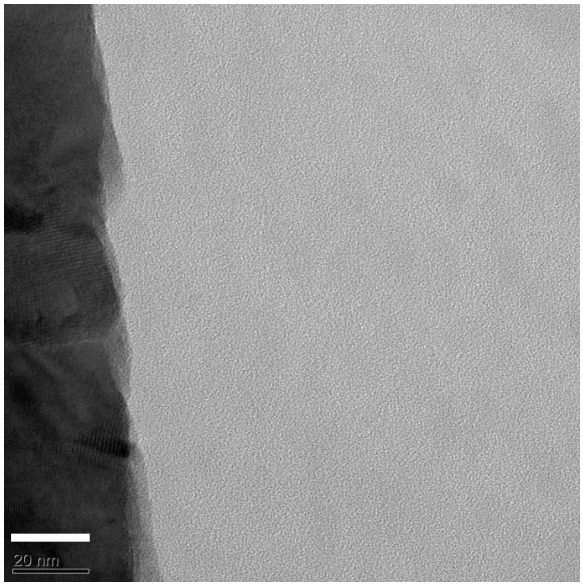

Figure 4.9 Cross-sectional TEM image of 3.5 μm thick CNETMS film on indium tin oxide coating, again showing a relatively dense, homogeneous morphology. The ITO electrode appears as the dark phase on the left side of the images. 20 nm scale bar.

4.3.2 Dielectric properties

For electrical measurements, parallel-plate capacitors were produced by depositing circular aluminum top electrodes on top of CNETMS films. Detailed device fabrication and characterization procedures can be found in the Section 2.3.

The measured ε_r and loss tangent as a function of frequency for CNETMS films in parallel plate capacitor devices (Figure 4.10) are shown in Figure 4.11. The ε_r of the CNETMS films was ~20 at 1 kHz, consistent with the values for mixtures of cyanoalkyl-trialkoxysilanes reported previously.[76] The large ε_r of the CNETMS films is attributed to the contribution of orientational polarization of the dipolar cyano groups present in the sol-gel networks, as will be discussed below. The porous structure of the CNETMS films may provide sufficient free volume for field-induced rotational polarization of the cyano groups and interfacial contributions to the permittivity.[45] The measured ε_r of the CNETMS films showed only a small reduction as the frequency varied from 100 Hz to 1 MHz. However, at frequencies greater than 100 kHz, the ε_r decreases slightly while the loss tangent exhibits an increase in magnitude, indicating the onset of a dielectric relaxation.[48]

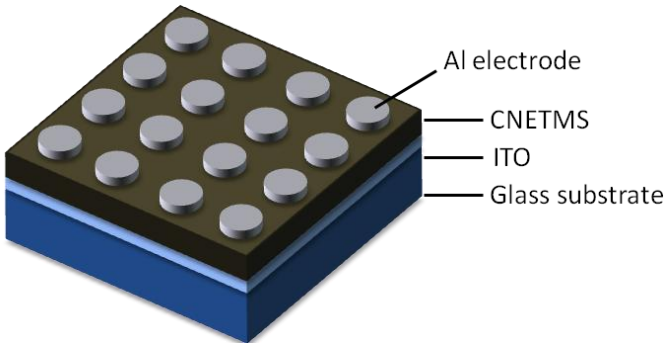

Figure 4.10 The schematic illustration of the capacitor device array containing CNETMS sol-gel films.

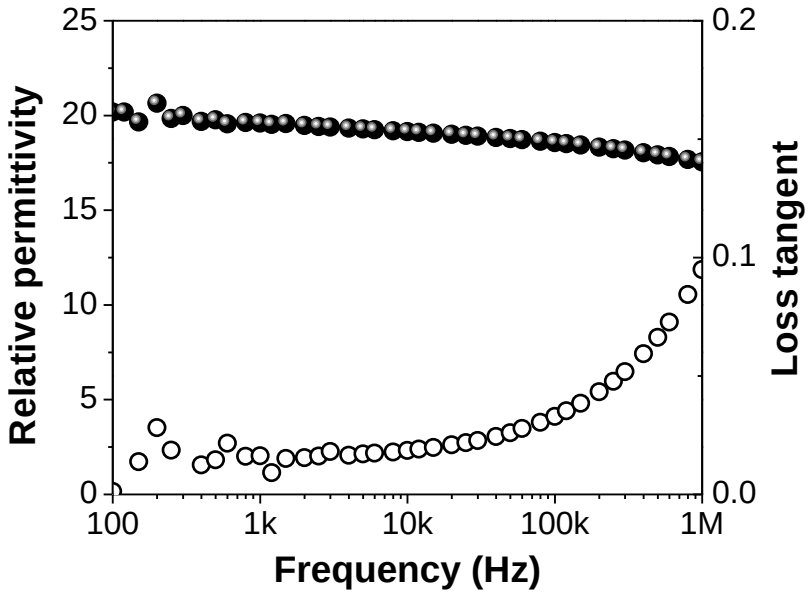

Figure 4.11 Frequency dependence of relative permittivity (solid points) and loss tangent (hollow points) of 1.3 μm thick CNETMS film.

Temperature dependent dielectric spectroscopy is a way to investigate polarization mechanism of dielectric materials. As discussed in the Section 1.1, unlike electronic and atomic polarizations, orientational or rotational polarization that involves reorientation process of dipolar molecules is strongly temperature dependent. As shown in Figure 4.12, the dielectric relaxation of loss tangent in CNETMS films starts to emerge at frequency range below 100 Hz as temperature increases and peaks at 30 Hz at 100ºC. This relaxation peak clearly shifts toward high frequency range as temperature becomes higher. It is postulated that thermal energy reduces an energy barrier for dipolar molecules to reorient themselves in response to applied electric field. The decreased energy barrier is believed to originate from increased flexibility of crosslinked siloxane networks. The higher temperature, the lower the energy barrier, which is manifested by the evolution of dielectric relaxation frequency toward higher frequency range. Because of the porous structure of CNETMS xerogel, the interfacial polarization between pores and dipolar cyano groups may also contribute.

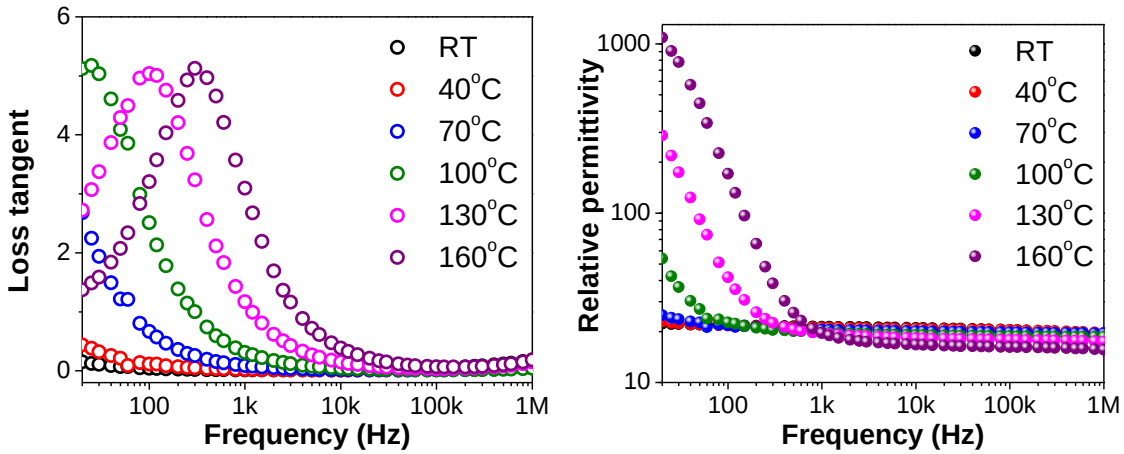

Figure 4.12 Temperature dependent (left) loss tangent and (right) permittivity of 1.3 μm thick CNETMS film.

The dielectric breakdown strengths of the CNETMS films were determined and analyzed using the Weibull method, as has been discussed in Chapter 3 and elsewhere.[48] Briefly, the Weibull cumulative failure probability distribution (P_F) is expressed by the following equation:

$$P_F(E) = 1 - exp\left[-\{(E-\gamma)/\alpha\}^{\beta}\right] \qquad \text{Equation 4.1}$$

where E is the applied electric field, α is the "scale" parameter, β is the "shape" parameter or Weibull modulus (which represents dispersion of the breakdown field) and γ is the electric field breakdown threshold parameter, which represents the field below which no observable failure occurs. Conventionally, the characteristic breakdown strength, E_{BD}, is defined as the field where P_F is 63.2%.

The failure probability of the CNETMS films with different thickness as a function of the applied electric field is shown in Figure 4.13. In general, the narrower the cumulative distribution function (CDF) with respect to electric field, the more reliable the material is for high dielectric strength applications.

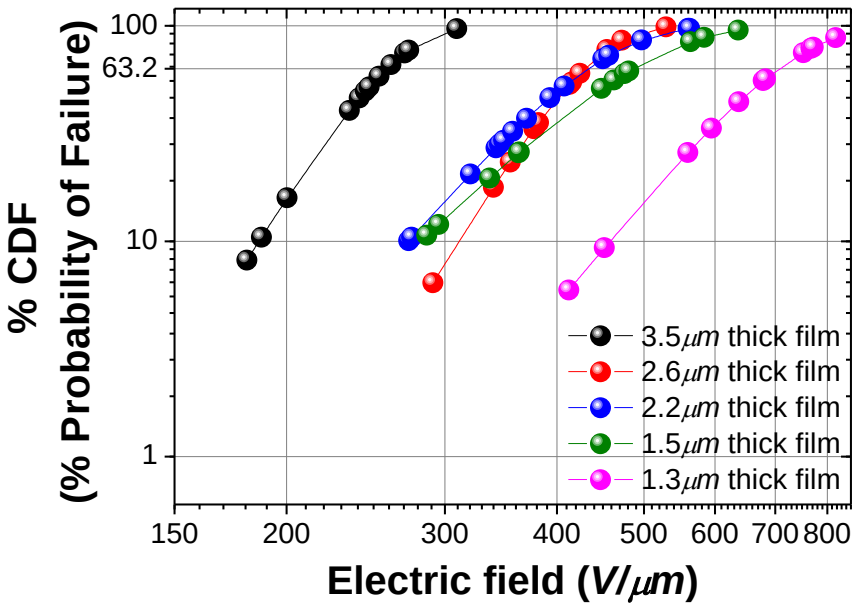

Figure 4.13 The % cumulative distribution function (% CDF) for CNETMS films with different thicknesses as a function of electric field.

The effect of thickness on the dielectric breakdown strength for CNETMS films is shown in Figure 4.14. In this graph, we plotted the average breakdown strength ($<E_B>$) over the measured distribution of breakdown fields for a given sample. It can be seen that $<E_B>$ increases as the thickness of the CNETMS films decreased, following an approximate inverse dependence on thickness, i.e. $<E_B> \sim d^{-1}$, (see Figure 4.15) as is typically observed for oxide and polymer thin films.[101, 113, 114] The maximum $<E_B>$ is ~650 V/μm for 1.3 μm thick CNETMS film. On the other hand, the Weibull modulus, β, decreases somewhat as the thickness of CNETMS is reduced, indicating a broader distribution of breakdown strength. A possible reason is that ionizable groups or trapped charges at the interfaces of these porous thin films may be distributed somewhat inhomogeneously.

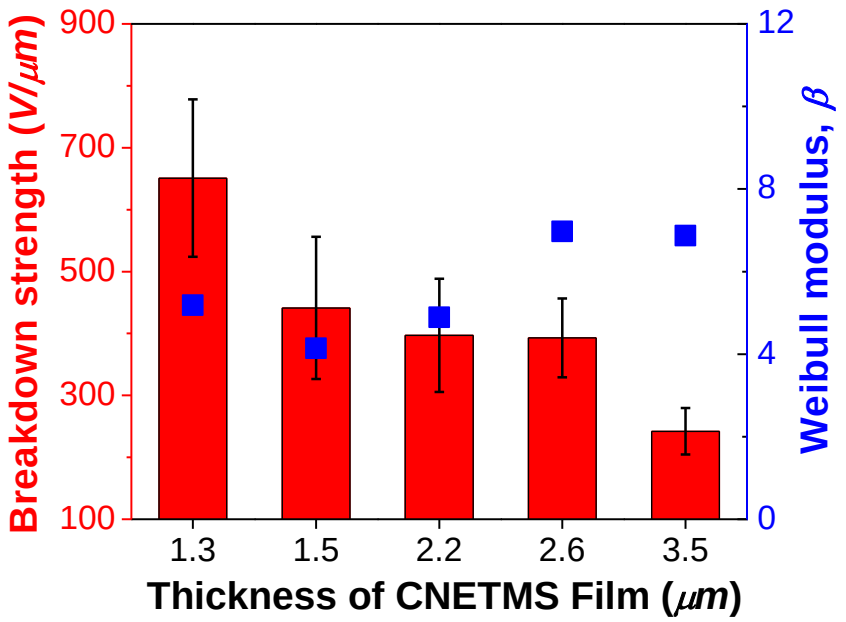

Figure 4.14 Thickness dependence of average breakdown strength (<E_B>) and Weibull modulus for CNETMS films. The error bars represent the standard deviation (1σ) of the average breakdown strength obtained from 12-20 devices.

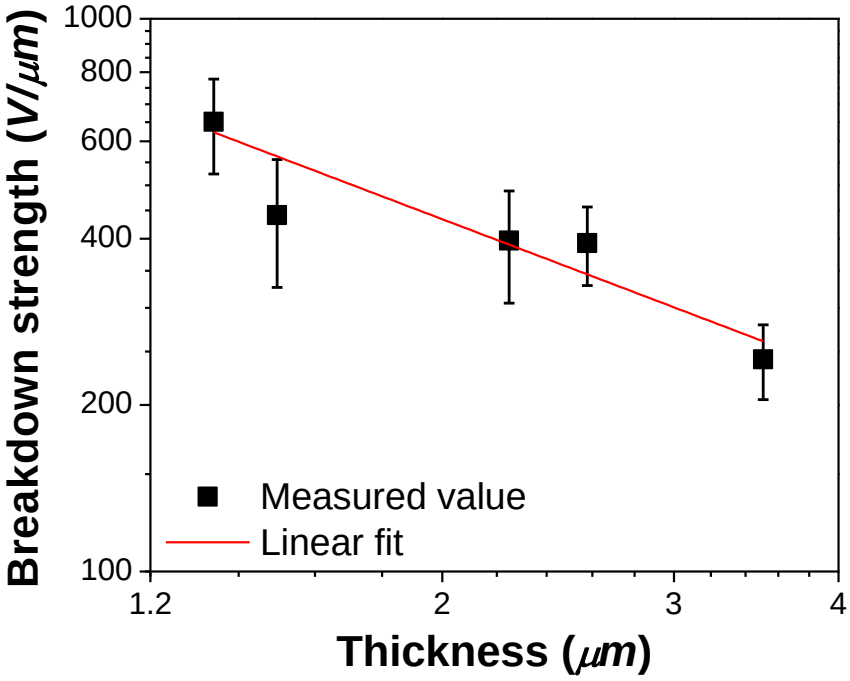

Figure 4.15 Average breakdown strength (<E_B>) and its standard deviation (1σ) of CNETMS films as a function of thickness. A linear fit gives $E_B = 2.91 * d^{-0.90}$, where d is the thickness of CNETMS film.

The thickness dependence of the breakdown strength of polymer thin films has been studied earlier for a number of polymers as well as ceramics.[101, 113, 114] The origin of this dependence is attributed to the increased probability of finding a defect site leading to a conduction or breakdown path in films as the volume of material increases. As this probability increases with the thickness of the film, the breakdown strength typically varies inversely with the film thickness. Consequently, a power law expression describes the relationship between breakdown strength and thickness:

$$E_B \propto d^{-n} \qquad \text{Equation 4.2}$$

where E_B is the breakdown strength, d is the thickness of thin films and n is a factor ranging from 0.3 to 0.9. An n value of 0.90 is obtained for CNETMS films with various thicknesses as the slope of a linear fit in Figure 4.15 and the value of n matches well with the numbers reported for polymer films with similar thickness range.[101, 114]

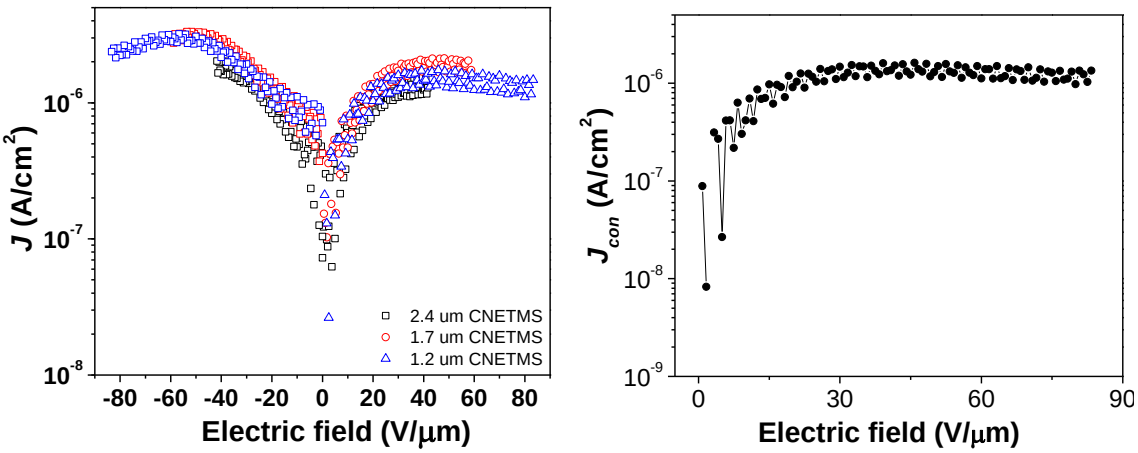

Figure 4.16 (left) Leakage current for CNETMS thin films of varying thickness showing saturation of the current density at fields > 30 V/ μm or < -30 V/ μm. (right) Conduction current density after correcting total current for the displacement current.[83]

Leakage current profiles of CNETMS films with different thicknesses are presented in Figure 4.16. Conduction current profile of 1.3 μm thick CNETMS film is extracted by using Equation 2.3 in the Section 2.4 since CNETMS must be linear dielectrics in the

electric field range below 100 V/μm. The conduction current of CNETMS is that of a typical insulator with initial rise followed by the saturation of current. The conductivity at low field was estimated as 8×10^{-12} S/cm.

4.3.3 Energy storage characteristics

To determine the maximum extractable energy density (U_{max}^{CD}) under pulsed conditions of CNETMS films, charge-discharge (C-D) measurements were performed. As shown in Figure 4.17, the 3.5 μm thick CNETMS film gave a U_{max}^{CD} value of ~ 4 J/cm^3, whereas the value for 1.3 μm thick CNETMS was ~7.5 J/cm^3, which is about twice as high as that of the thicker CNETMS film, as a result of the higher $<E_B>$ for the thinner film. The reduction of breakdown strength in C-D measurements compared to breakdown testing (shown in Figure 4.14) is attributed to electrical stress during the pulsed measurement conditions and the use of a larger electrode area (0.25 mm^2 for breakdown testing and 1.0 mm^2 for C-D measurements). The solid lines in Figure 4.17 correspond to a quadratic fit to measured data (average values and error bars are shown when two or three devices were measured at the same electric field). Although there are some deviations at higher fields that are likely associated with leakage currents (Figure 4.16), the increase of the extractable energy density fits reasonably well to the quadratic function, which would be expected for a linear dielectric. The lower β values of thin CNETMS films are consistent with the more scattered U_{max}^{CD} than that of thicker films, which suggests that thinner CNETMS films are more prone to catastrophic breakdown events particularly at high electric fields.

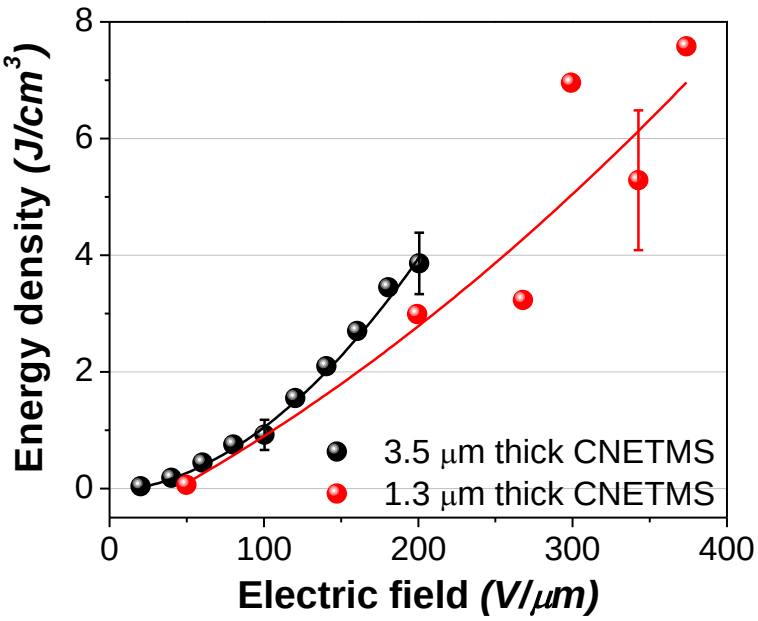

Figure 4.17 Extractable energy density of 3.5 μm and 1.3 μm thick CNETMS films from charge-discharge measurements. The error bars were obtained from measurements of 2-5 devices at the given electric field strength whereas the data points without an error bar were obtained from a single measurement at the applied electric field.

Figure 4.18 shows the unipolar polarization-electric field (P-E) loops of 1.3 μm thick CNETMS films as a function of electric field. P-E loops measured up to 300 V/μm display narrow hysteresis and linear dielectric-like behavior, which is desirable for achieving high energy storage density and low loss in pulsed power applications.[18] Linear dielectric-like polarization response is also observed for 3.5 μm thick CNETMS films (shown in Figure 4.19) but only for fields up to ~130 V/μm. Further increases in field strength exceeding 300 V/μm (shown in the inset in Figure 4.18) leads to a discernible rounding of the shape of P-E loops, indicating a contribution from electrical conduction possibly coming from injected charge carriers, which is reflected in the increased energy loss following reversal of the field.[83, 115] The difference in behavior of the thin and thick films suggests that the onset of charge injection or conduction is reduced in thick films, consistent with the trend of the breakdown data, and may be associated with an increase of voids, impurities, and trapped charges in CNETMS films

when the thickness is increased.

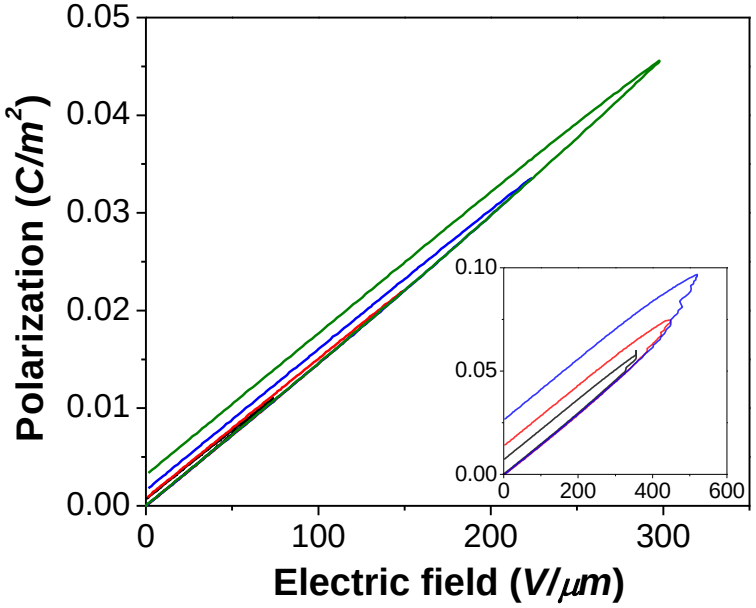

Figure 4.18 Polarization-electric field (P-E) hysteresis loops of 1.3 µm thick CNETMS films (loops above 300 V/µm shown in the inset).

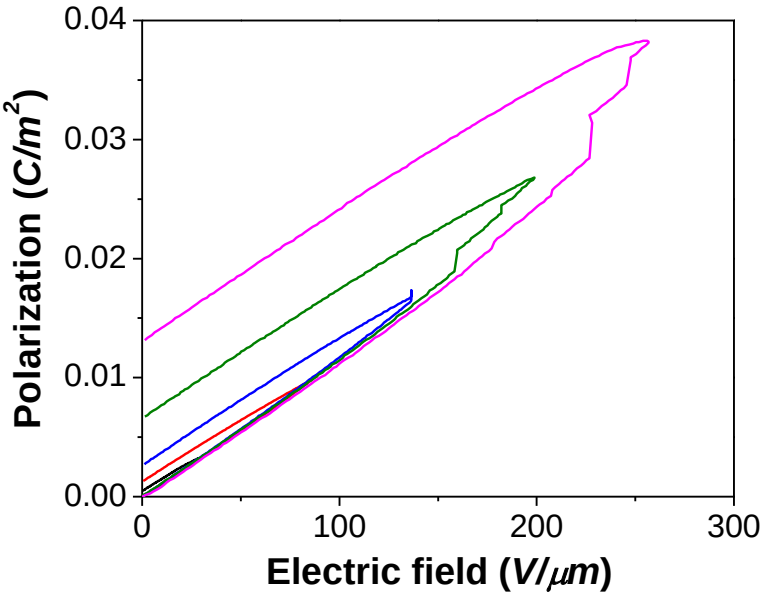

Figure 4.19 P-E hysteresis loops of 3.5 µm thick CNETMS film as a function of electric field.

We have assessed the extractable energy density, U_{max}^{PE}, and the energy extraction efficiency from the P-E measurements on the CNETMS films by integrating the area under the charge and discharge curves[17] as explained in the Section 2.4 and Figure 2.5.

The U_{max}^{PE} and the energy extraction efficiency of CNETMS films are shown in Figure 4.20. CNETMS films with a thickness of 3.5 μm exhibit a U_{max}^{PE} value of ~4 J/cm^3 at ~300 V/μm, whereas the U_{max}^{PE} of 1.3 μm thick CNETMS is determined to be ~19 J/cm^3 at ~500 V/μm, resulting from both the higher <E_B> and the energy extraction efficiency, as is indicated by narrow hysteresis loops, arising from the lower film thickness. It should be noted that the energy loss in dielectric capacitors will be dissipated in the form of heat, thereby limiting the efficiency and, more importantly, the lifetime of capacitors in use. Accordingly, the maximum extractable energy density of a capacitor has to be determined with due consideration of the energy extraction efficiency.

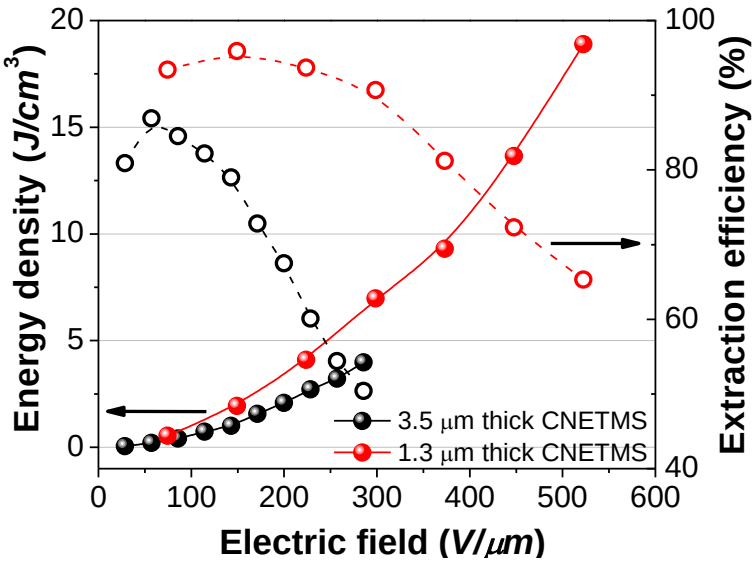

Figure 4.20 Extractable energy density and extraction efficiency from polarization-electric field measurements for 3.5 μm and 1.3 μm thick CNETMS films. Energy density and extraction efficiency are shown in solid and hollow points, respectively.

As explained in the Section 2.4, the conduction current of linear dielectric materials can be extracted from P-E loops. Using Equation 2.6, conduction currents of CNETMS films of 1.3 and 3.5 μm thick were determined and shown in Figure 4.21. Both films exhibit oscillatory variation in current density in common, presumably due to the field activation of injected and trapped charge carriers. For 3.5 μm thick CNETMS film, the conduction behavior appears around at 120 V/μm and reaches maximum at around 240 V/μm. These

values for the onset of conduction and the field at maximum conduction current are much lower for thicker CNETMS film, which is consistent with lower breakdown strength and energy extraction efficiency of 3.5 μm thick CNETMS film. On the contrary, the onset of conduction behavior for 1.3 μm thick CNETMS film first appears at 200 V/μm and conduction current peaks at around 450 V/μm. The data for the 1.3 μm thick films shows an average conductivity of ~ 2×10^{-12} S/cm, which is within the range of silica sol-gel glass.[116]

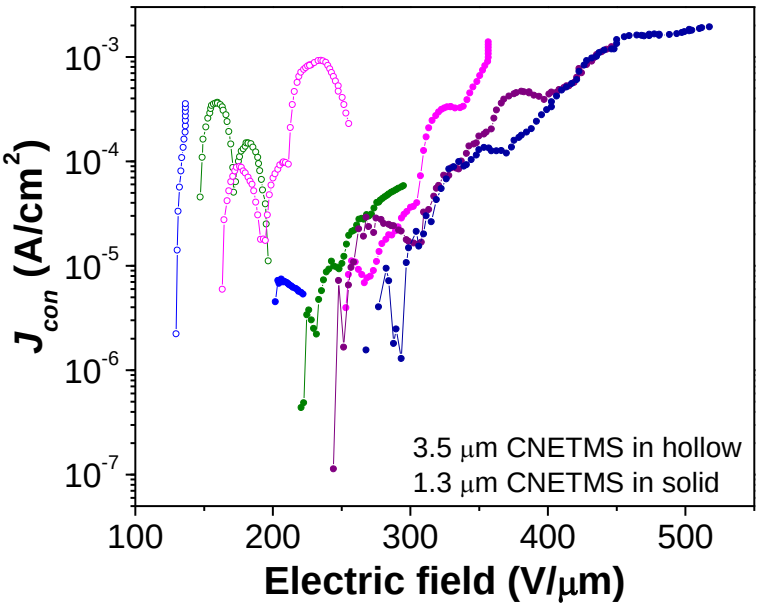

Figure 4.21 High-field J-E characteristic for CNETMS thin films of 1.3 and 3.5 μm thickness which shows some oscillatory variations in J, presumably due to the field activation of trapped charges. Conduction current density after correcting total current for the displacement current.

Table 4.1 summarizes U_{max}^{CD} , U_{max}^{PE} and the energy extraction efficiency for the 1.3 μm and 3.5 μm thick CNETMS films. To take extraction efficiency into account, the value of U_{max}^{PE} is chosen at a moderate electric field, 300 V/μm for the 1.3 μm and 200 V/μm for the 3.5 μm thick CNETMS film, respectively. U_{max}^{PE} of 3.5 μm thick CNETMS is ~2 J/cm^3 with extraction efficiency of 68%, whereas 1.3 μm CNETMS achieves 7 J/cm^3 of

U_{max}^{PE} with extraction efficiency of 91%. As shown in wide hysteresis loop at ~200 V/μm in Figure 4.19, the loss in 3.5 μm thick CNETMS significantly compromises the energy extraction efficiency even for moderate electric fields. On the contrary, 1.3 μm thick CNETMS maintains a high efficiency and large extractable energy at moderately high fields, as shown in both C-D and P-E measurements. Therefore, the suppression of electrical conduction possibly originating from charge carrier injection at high electric field is highly desirable to further enhance the energy storage and extraction capabilities and the device reliability of CNETMS dielectric film.

Table 4.1 U_{max}^{CD} , U_{max}^{PE} and the energy extraction efficiency of 1.3 μm and 3.5 μm thick CNETMS films.

CNETMS thickness (μm)	U_{max}^{CD} (J/cm^3)	U_{max}^{PE} (J/cm^3)	Energy extraction efficiency from P-E method
1.3	7±1 @ 300 V/μm	7.0 @ 300 V/μm	91%
3.5	4±1 @ 200 V/μm	2.1 @ 200 V/μm	68%

4.4 Effects of Moisture and Solvent

In this section, the effect of processing variables during and after sol-gel reaction will be discussed. Because of the porosity and the presence of hydroxyl groups in bulk and surface of CNETMS xerogels films, the dielectric and the electrical properties of CNETMS xerogels films are prone to be affected by moisture. In the first part of this section, therefore, the effect of moisture on the electrical property of CNETMS films will be discussed. Secondly, as mentioned in the Section 4.1, the microstructure and the porosity of sol-gel materials are known to be heavily dependent on processing variables such as the concentration of sols, pH of catalyst, ageing, etc. The later part of this section will focus on the effects of solvent and acidity on dielectric and electrical properties of CNETMS sol-gel films in order to find optimal processing variables to maximize energy storage capability of dielectric films thereof.

4.4.1 The effect of moisture

To investigate the effect of moisture on CNETMS films, the leakage current of sol-gel films was monitored daily up to seven days when sample films were kept in glove box purged with nitrogen. The effect of moisture on the current density of CNETMS films is readily seen in Figure 4.22. The current density of CNETMS film, which had been stored under ambient and tested just after being placed in a glove box, was reduced on the order of magnitude from 10^{-7} A/cm^2 to 10^{-6} A/cm^2 at the field strength of ± 75 V/μm after nitrogen treatment for three days. The reduction of leakage current can be attributed to the removal of physically adsorbed water molecules on CNETMS surfaces by nitrogen purging.

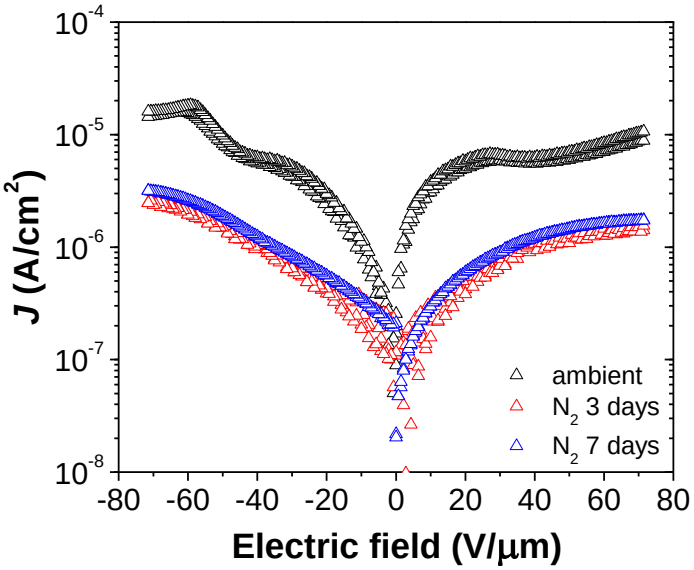

Figure 4.22 Leakage current profiles of CNETMS sol-gel films after being kept in a glove box purged with nitrogen.

To minimize the effect of moisture on leakage current, which would deteriorate the energy storage performance of dielectric materials by electrical conduction and associated premature dielectric breakdown events, all electrical and dielectric measurement in this thesis were performed in a glove box purged with nitrogen. In the case of P-E and C-D measurements in which such regulated condition was not achievable, measurements were conducted on samples particularly kept in a glove box or freeze dryer for at least two days before testing to minimize moisture contamination.

4.4.2 The effect of solvent

It was experimentally found that CNETMS sol-gel films synthesized with the presence of 2-methoxyethanol were thicker than those with methanol under the same processing conditions. This thickness difference is attributed to the higher boiling point of 2-methoxyethanol than methanol, whose boiling points and thicknesses are

summarized in Table 4.2.

Table 4.2 Boiling points of methanol and 2-methoxyethanol, and the thickness of CNETMS films with each solvent.

	Methanol	2-Methoxyethanol
Boiling point	65 ºC	124 ºC
Thickness of CNETMS film	1.3 μm	1.1 μm

Since the breakdown strength of dielectric film is inversely proportional to its thickness as discussed in the Section 4.3.2, it is worthwhile to investigate dielectric and energy storage properties of CNETMS films with 2-methoxyethanol, which is thinner than films with methanol.

Figure 4.23 compares indicates frequency dependent permittivity and loss tangent, and leakage current profile of CNETMS films synthesized with methanol or 2-methoxyethanol. There is a marginal decrease in permittivity and increase in loss tangent in all frequency range for CNETMS films with 2-methoxyethanol. However, CNETMS films with 2-methoxyethanol shows much stiffer initial rise in leakage current at fields below ±10 V/μm. Abrupt initial rise in leakage current may be ascribed to the presence of residual 2-methoxyethanol in CNETMS film because of high boiling point. It is worthwhile to note that current above ±50 V/μm is higher for CNETMS film with methanol than 2-methoxyethanol.

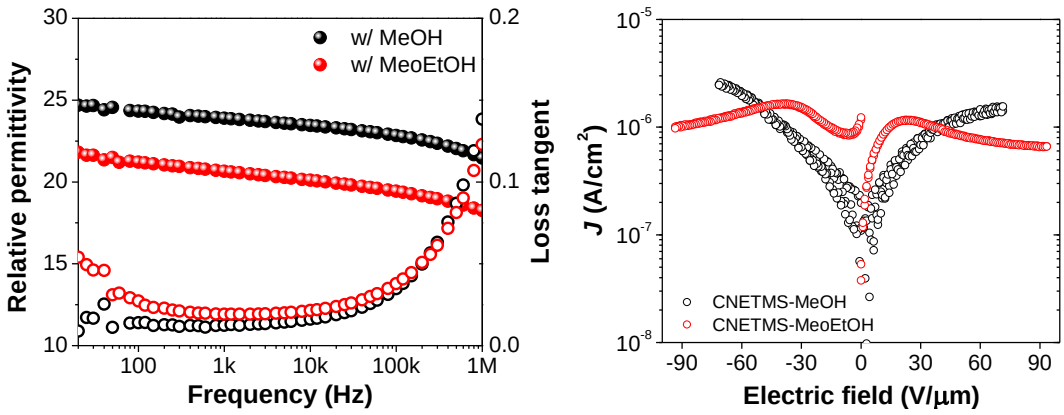

Figure 4.23 (left) Frequency dependent permittivity and loss tangent and (right) leakage current profile of CNETMS sol-gel films with methanol (1.3 μm thick) and 2-methoxyethanol (MeoEtOH) (1.1 μm thick)

CNETMS films with 2-methoxyethanol is further examined by P-E measurements, which is shown in Figure 4.24. Unlike slim hysteresis loop of CNETMS films with methanol shown in Figure 4.18, P-E loops of CNETMS films with 2-methoxyethanol exhibit roundish shape even at fields after ~200 V/μm, leading to lower energy density and extraction efficiency compared to CNETMS films with methanol (see Figure 4.20). Widening of P-E loops also indicate the contribution of electrical conduction becoming apparent at fields above ~200 V/μm, implying the structure of CNETMS films with 2-methoxyethanol is more susceptible to charge carrier injection from metal electrodes, as compared to CNETMS with methanol. Since there must be a channel for electrical conduction to occur, CNETMS films with 2-methoxyethanol could have more low-density domains than CNETMS with methanol, as proposed by Kao[9], or residual 2-methoxyethanol may contribute to electrical conduction.

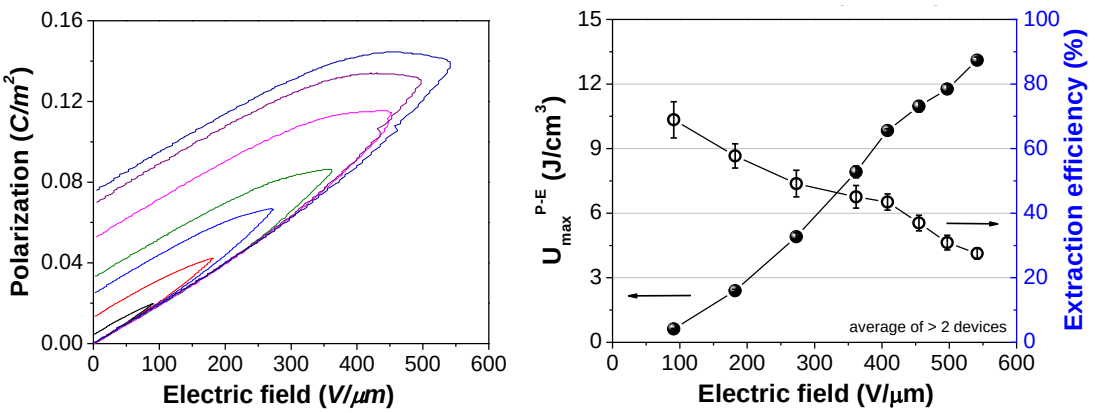

Figure 4.24 (left) P-E loops of CNETMS films with 2-methoxyethanol; (right) U_{max}^{PE} and extraction efficiency of the same sol-gel films.

4.5 Effect of Alkyl Chain Length of Sol-gel Precursors

The large permittivity and energy density of CNETMS films are attributed to the orientational polarization of dipolar cyano groups with linear dielectric-like polarization response, as supported by narrow hysteresis loops. It is hypothesized that the presence of alkyl spacer from siloxane backbone would provide rotational mobility to cyano groups to reorient themselves under the direction of electric field. In this section, to investigate this hypothesis, silicate sol-gel precursors with varying the length of alkyl spacer were prepared to form sol-gel films and their dielectric and energy storage properties are compared.

4.5.1 Dielectric and electrical properties

Sol-gel films from 3-cyanopropyltriethoxysilane (CNPTES), which has one more carbon spacer between siloxane backbone and cyano group than CNETMS, were prepared by the same protocol used for CNETMS sol-gel films. As shown in Figure 4.25, the dielectric relaxation of loss tangent in CNPTES films begins to show up at

30 Hz at 40ºC, which is 60 ºC lower temperature than that in CNETMS films (see Figure 4.12). At 100ºC, loss tangent peaks at around 1 kHz, while at the same temperature the dielectric relaxation peak of loss tangent in CNETMS films appears at ~30 Hz, indicating the relaxation time responsible for dielectric response in sol-gel films is much shorter in CNPTES films. Shorter relaxation time associated with orientational polarization in CNPTES sol-gel films must be related to the increased rotational freedom of polar cyano groups, indicating the contribution of longer alkyl spacer in CNPTES films.

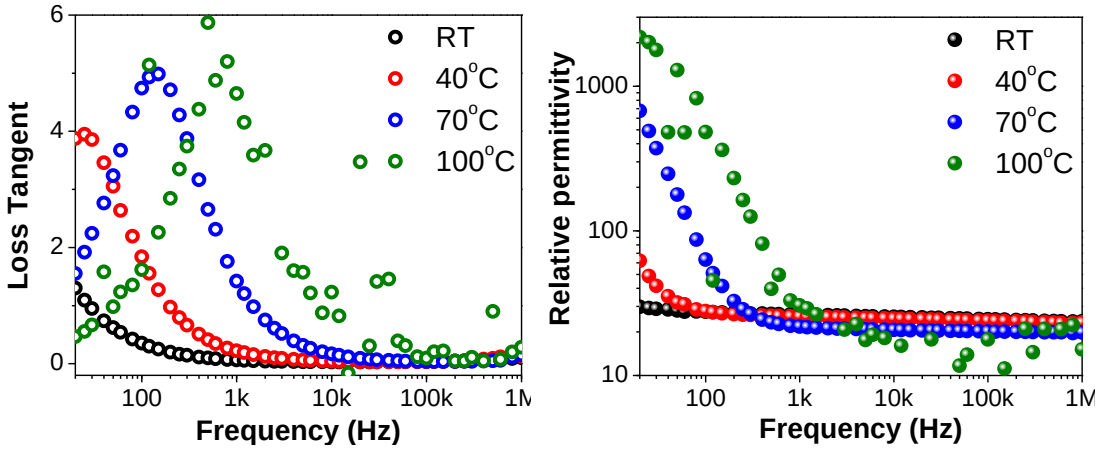

Figure 4.25 Temperature dependent (left) loss tangent and (right) permittivity of 1.7 μm thick CNPTES film with methanol.

It could be imagined that increased rotational freedom of polar groups in dielectric materials would enhance net polarizability of system if the cooperative motion of individual dipole moment does not cancel each other when external electric field is employed. Permittivities of CNPTES films with methanol or 2-methoxyethanol (shown in Figure 4.26) exhibit substantial increase compared to CNETMS films, 30 and 27 at 1 kHz, respectively. It is worthwhile to note that loss tangents of CNPTES films with both solvents indicate dielectric relaxation behavior at just below 20 Hz, which was not observed in CNETMS films at room temperature, suggesting shorter relaxation time for orientational or rotational polarization mechanisms. We believe

that 1) increased rotational freedom of cyano groups associated with longer alkyl spacer and 2) increased contribution of interfacial polarization between dipolar molecules and pores may account for shorter time scale of dielectric relaxation.

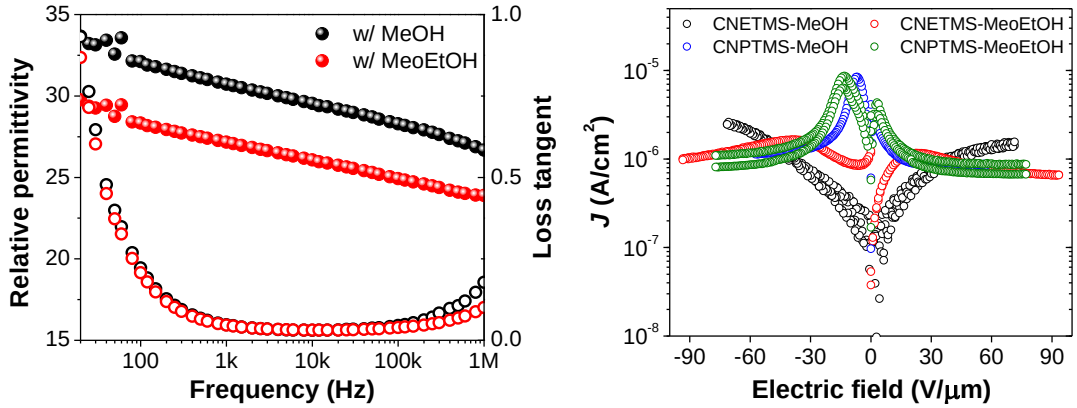

Figure 4.26 (left) Frequency dependent permittivity and loss tangent of CNPTES sol-gel films with methanol and 2-methoxyethanol (MeoEtOH); (right) leakage current profile of CNETMS and CNPTES sol-gel films with methanol and 2-methoxyethanol as solvents.

Although CNPTES sol-gel films showed increased permittivity, their leakage current profile exhibit much stiffer initial rise compared to CNETMS film with 2-methoxyethanol at fields below ±10 V/μm (see Figure 4.26). In the previous section, increased initial slope in current density of CNETMS-MeoEtOH films was attributed to residual solvent in sol-gel films. However, in CNPTES sol-gels, current densities of both films with methanol and 2-methoxyethanol exhibit very similar profile over all electric field range, indicating the presence of another mechanism for enhanced electrical conduction in low fields. One possible hypothesis is that longer alkyl spacer in CNPTES system would increase not only rotational freedom of polar cyano groups, but also free volume of three-dimensional sol-gel network, in other words the porosity of CNPTES sol-gel films. The larger thickness of CNPTES films than CNETMS prepared by the exact same protocol, which is summarized in Table 4.3, can also be ascribed to the larger porosity in CNPTES films. Since carrier mobility in pores is much larger than in SiO_2 in sol-gel materials, the increased electrical

conductivity, which is the slope in leakage current profile, of CNPTES may be rationalized.

Table 4.3 Thickness of sol-gel films from CNETMS and CNPTES precursors with methanol and 2-methoxyethanol.

	CNETMS	CNPTES
Methanol	1.3 μm	1.7 μm
2-Methoxyethanol	1.1 μm	1.3 μm

In summary, CNPTES sol-gel films containing longer alkyl chain spacer exhibit increased permittivity and shorter time scale of dielectric relaxation compared to CNETMS sol-gel films. However, larger conductivity in low field range suggests the increased charge carrier mobility, which may be due to increased free volume or porosity in CNPTES sol-gel films. In the next section, the energy storage performance of CNPTES sol-gel films will be investigated.

4.5.2 Energy storage characteristics

P-E loops of CNPTES sol-gel films with methanol and 2-methoxyethanol are shown in Figure 4.27. Wide hysteresis loops and large remnant polarization are easily observed, which is far from linear dielectric-like response from CNETMS-MeOH sol-gel films (see Figure 4.18), suggesting the significant contribution of electrical conduction inside sol-gel films. Due to large polarization hysteresis and remnant polarization, the energy densities of CNPTES sol-gel films from both P-E and C-D methods shown in Figure 4.28 are much reduced compared to the CNETMS films with both methanol and 2-methoxyethanol. Although the permittivity of CNPTES sol-gel films is larger than that

of CNETMS films, electrical conduction originate from possible free volume or porosity associated with longer alkyl spacer between siloxane backbone and cyano molecules eventually deteriorate the energy storage performance of sol-gel films from CNPTES precursor.

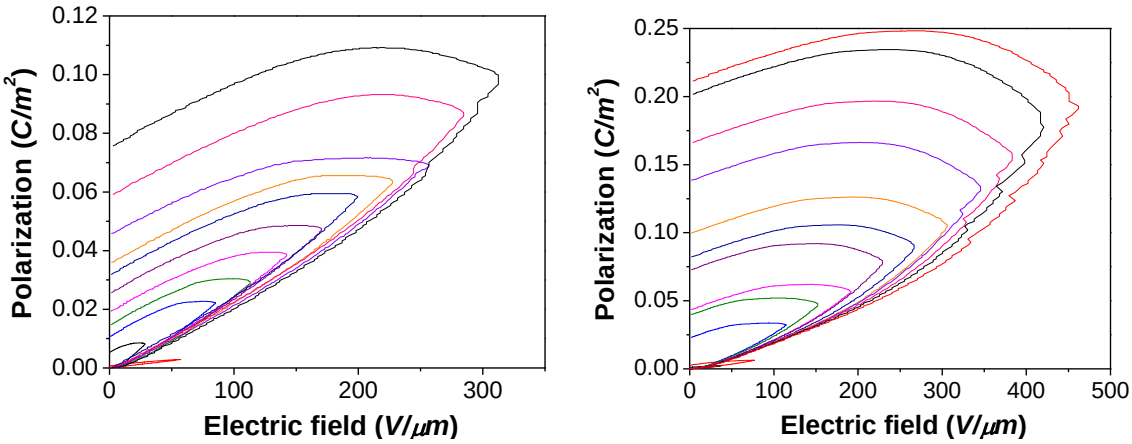

Figure 4.27 P-E loops of CNPTES sol-gel films with (left) methanol and (right) 2-methoxyethanol as a solvent.

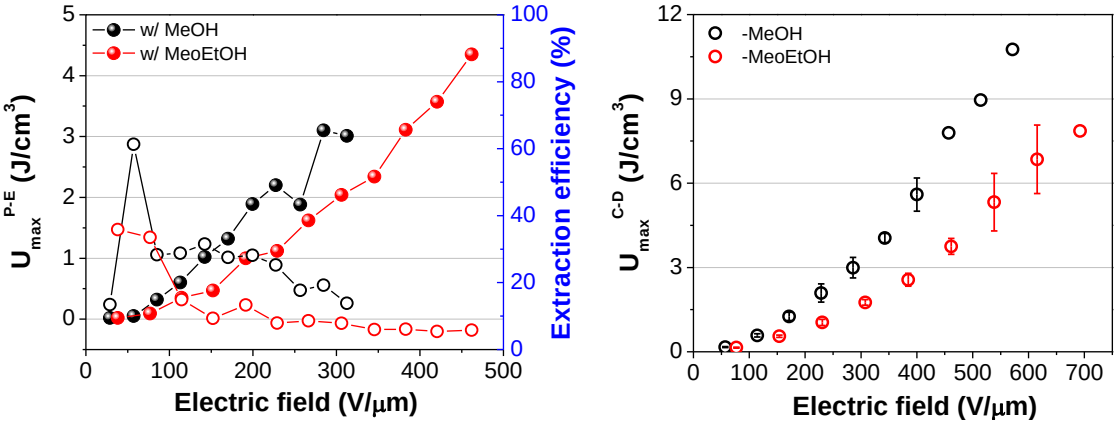

Figure 4.28 (left) U_{max}^{PE} and (right) $U_{max}^{CD}$of CNPTES sol-gel films. As a catalyst, 0.1 N hydrochloric solution was used. In left graph, U_{max}^{PE} is shown as solid dots and extraction efficiency shown as hollow dots.

4.6 Effect of Crosslinking Density

We have learned from the previous sections that electrical conduction associated with free volume or porosity in dielectric sol-gel films can substantially deteriorate energy storage performance of sol-gel films. Although it was proposed that the pore size of CNETMS-MeOH sol-gel is no greater than 1 nm via XRD and TEM measurements, the further reduction of pore size and free volume in the sol-gel is highly desirable because the presence of air in pores and voids in the sol-gel may lead to partial discharge and associated premature dielectric breakdown events.

Since three-dimensional SiO_2 sol-gel networks are generated *via* simultaneous hydrolysis and condensation of alkoxysilane moieties in sol-gel precursor, the number of hydrolysable and condensable alkoxy groups in sol-gel precursor could determine the crosslinking density and free volume or porosity of sol-gel networks.

In this section, two different sol-gel precursors, tetraethyl orthosilicate (TEOS) and 2-cyanoethylmethyldimethoxysilane (CNEMDMS), are blended with CNETMS precursor to form sol-gel dielectric films. Compared to three hydrolysable alkoxy moieties in CNETMS, each precursor has one more, for TEOS, or one less, for CNEMDMS, hydrolysable groups, which could lead to more or less crosslinkings in sol-gel networks, respectively. The absence of polar side groups in TEOS also could play a role in dielectric property of the sol-gel blend.

Sol-gel blends of CNETMS with TEOS and CNETMS with CNEMDMS were prepared by mixing precursors with 0.1 N hydrochloric solution and methanol and 2-methoxyethanol for TEOS and CNEMDMS, respectively. The mixed sols were subject to the same protocol for CNETMS for film fabrication.

4.6.1 CNETMS-TEOS blends

Since the relative permittivity of silica is ~4, the inclusion of TEOS to CNETMS is expected to lower permittivity of sol-gel blend compared to neat CNETMS films. Although 5 mol% of TEOS blend is an exception, the sol-gel blends containing more than 20 mol% of TEOS show gradual decrease in permittivity, as shown in Figure 4.29a and 30a, reaching ~ 19 at 30 mol% of TEOS, which is about 20% lower than neat CNETMS (~ 24). At 30 mol% of TEOS, permittivity and loss tangent show dramatic decrease and increase respectively at frequencies above 100 kHz, which can be attributed to the onset of dielectric relaxation. Thickness of the blends declines along with the addition of TEOS and shrinks to 0.84 μm at 30 mol% of TEOS, which is about 30% lower than neat CNETMS (1.34 μm) (shown in Figure 4.30a). The reduction of thickness in the blends may be attributed to the densification of sol-gel networks due to larger number of cross-linked sites.

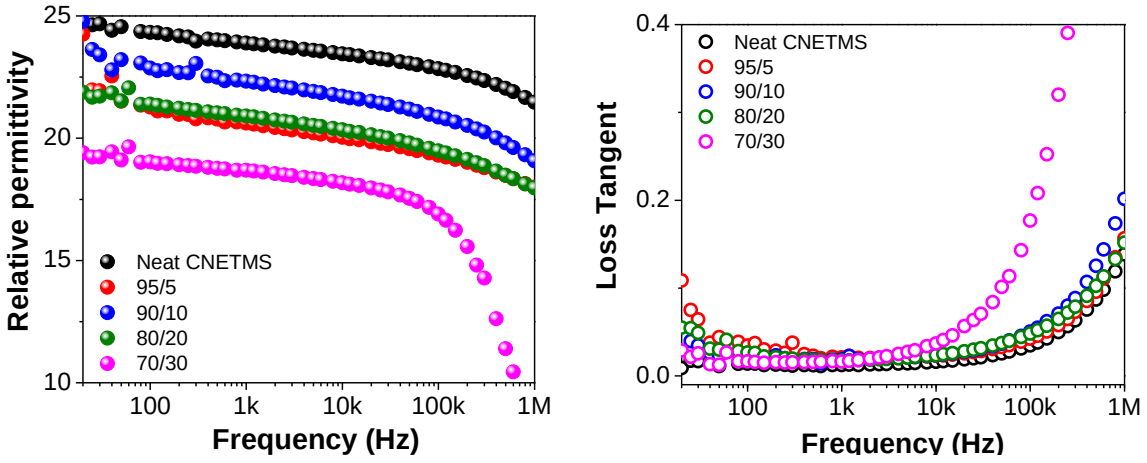

(a) (b)

Figure 4.29 Frequency dependent (a) relative permittivity and (b) loss tangent for the CNETMS-TEOS blends with molar percent of TEOS from 0 to 30.

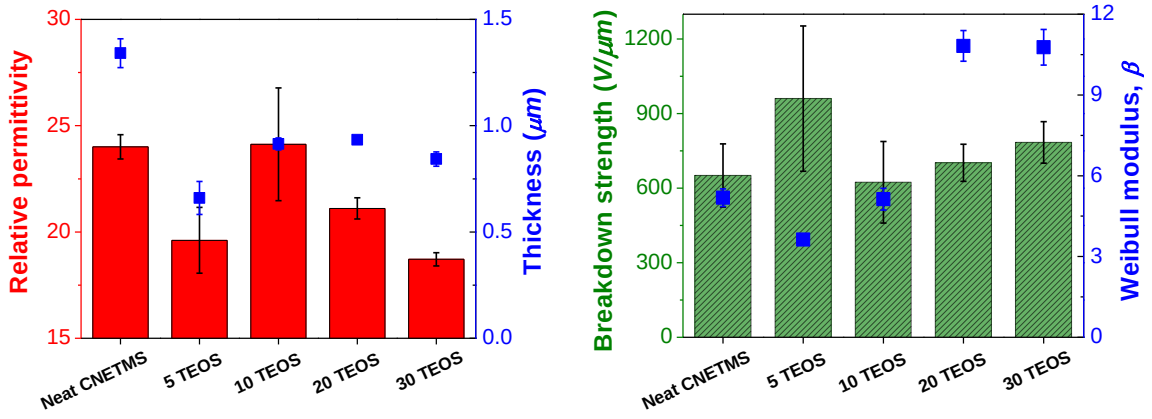

(a) (b)

Figure 4.30 (a) Relative permittivity (at 1 kHz) and thickness and (b) E_B and Weibull modulus including error bars (1σ) for the CNETMS-TEOS blends as a function of molar percent of TEOS.

Figure 4.30b summarizes breakdown strength, E_B and Weibull modulus of the blends, which is associated with the dispersion of E_B. In general, larger Weibull modulus translates into higher reliability in dielectric breakdown behavior, which is desirable in capacitor devices. With the exception of 5 mol% of TEOS, $E_B$of the blends are similar to neat CNETMS considering the error bars. The considerable rise of $E_B$in 5 mol% of TEOS can be ascribed to the thickness of the particular composition, which is half of neat CNETMS. It has been shown that the breakdown strength of CNETMS films follows an approximate inverse dependence on thickness.[102] It should be noted that Weibull modulus of the blends with more than 20 mol% of TEOS exhibit remarkable increase around 11. The densification of the films and the absence of polar side groups in TEOS may be attributed to the substantial growth in Weibull modulus.

In J-E curves for the blends shown in Figure 4.31a, the current density profiles of blends including neat CNETMS exhibit similar trend in which current density rises initially up to 50 V/μm, followed by saturation and a subsequent plateau. It is worth to note that the conductivity of the blends, which can be derived from the slope of initial rise in current density profile, decreases as the mol% of TEOS increases and returns to that of neat

CNETMS. Conduction current, J_{con}, in Figure 4.31b also shows similar trend with the conduction current level of ~ 10^{-6} A/cm^2. Higher conductivity of sol-gel films shown in the blends containing from 5 to 20 mol% of TEOS at low fields may be correlated with increased porosity possibly due to the phase separation of TEOS and CNETMS domains, thus leading to lower breakdown strength and Weibull modulus.

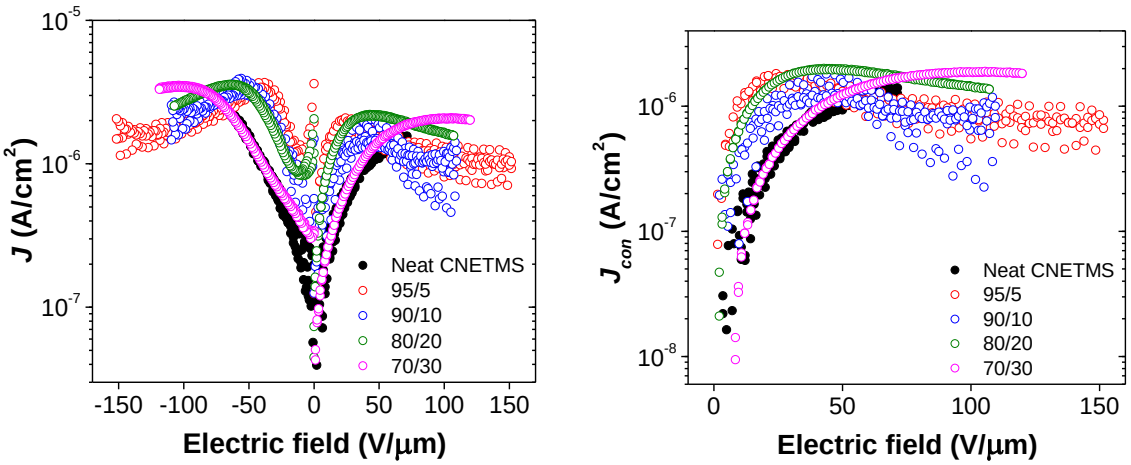

(a) (b)

Figure 4.31 (a) Current density-electric field (J-E) characteristics and (b) conduction current of CNETMS-TEOS blends as a function of electric field.

Figure 4.32 summarize extractable energy density, U_{max}, of CNETMS-TEOS blends up to 50 mol% of TEOS from P-E and C-D methods. For 5 and 10 mol% of TEOS blends, U_{max}^{PE} reached ~27 J/cm^3 and ~22 J/cm^3 respectively, which are much higher than that of neat CNETMS (shown as 0 TEOS in Figure 4.32). However, for higher mol% of TEOS blends, U_{max}^{PE} did not go above the level of neat CNETMS, presumably due to lowered permittivity of blends. For energy extraction efficiency, there is not much enhancement when TEOS is incorporated into CNETMS matrix, showing gradual decrease of efficiency with increasing electric field. When it comes to P-E loops of CNETMS-TEOS blends shown in Figure 4.33, there is a gradual widening in hysteresis as mol% of TEOS goes up, which can be associated with increased electrical conduction. It is not clear why CNETMS-TEOS blends with up to 10 mol% of TEOS maintain higher extraction

efficiency and U_{max}^{PE} than neat CNETMS, but we postulate that as volume of TEOS inclusion grows, TEOS inclusions might create separated domains from CNETMS, generating permittivity gradient in local scale. The phase separation consisting of low and high permittivity domains would increase electric field concentration in low-*k* regions, leading to premature breakdown events in those regions, as expected in the case of nanocomposite material containing high-*k* filler in low-*k* matrix.

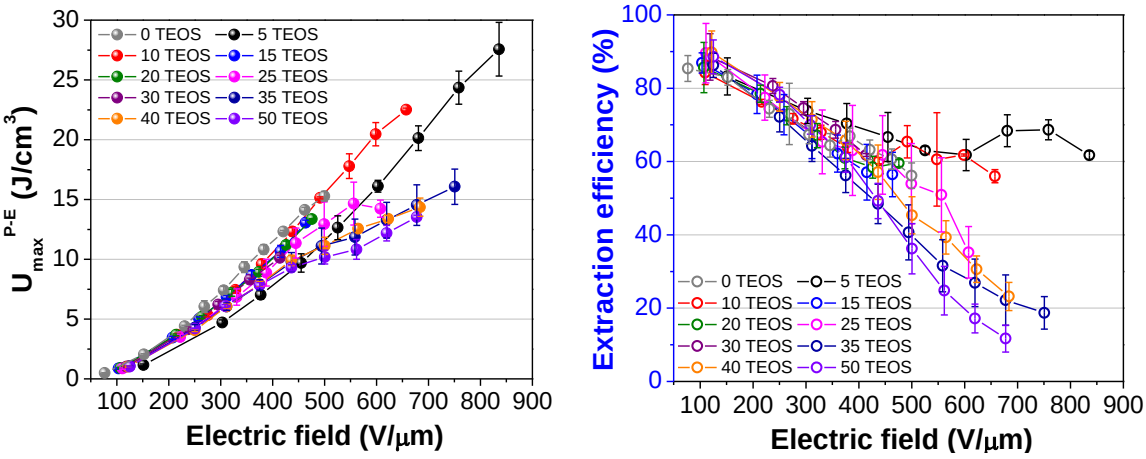

Figure 4.32 (left) U_{max}^{PE} and (right) Energy extraction efficiency of CNETMS-TEOS blends as a function of electric field.

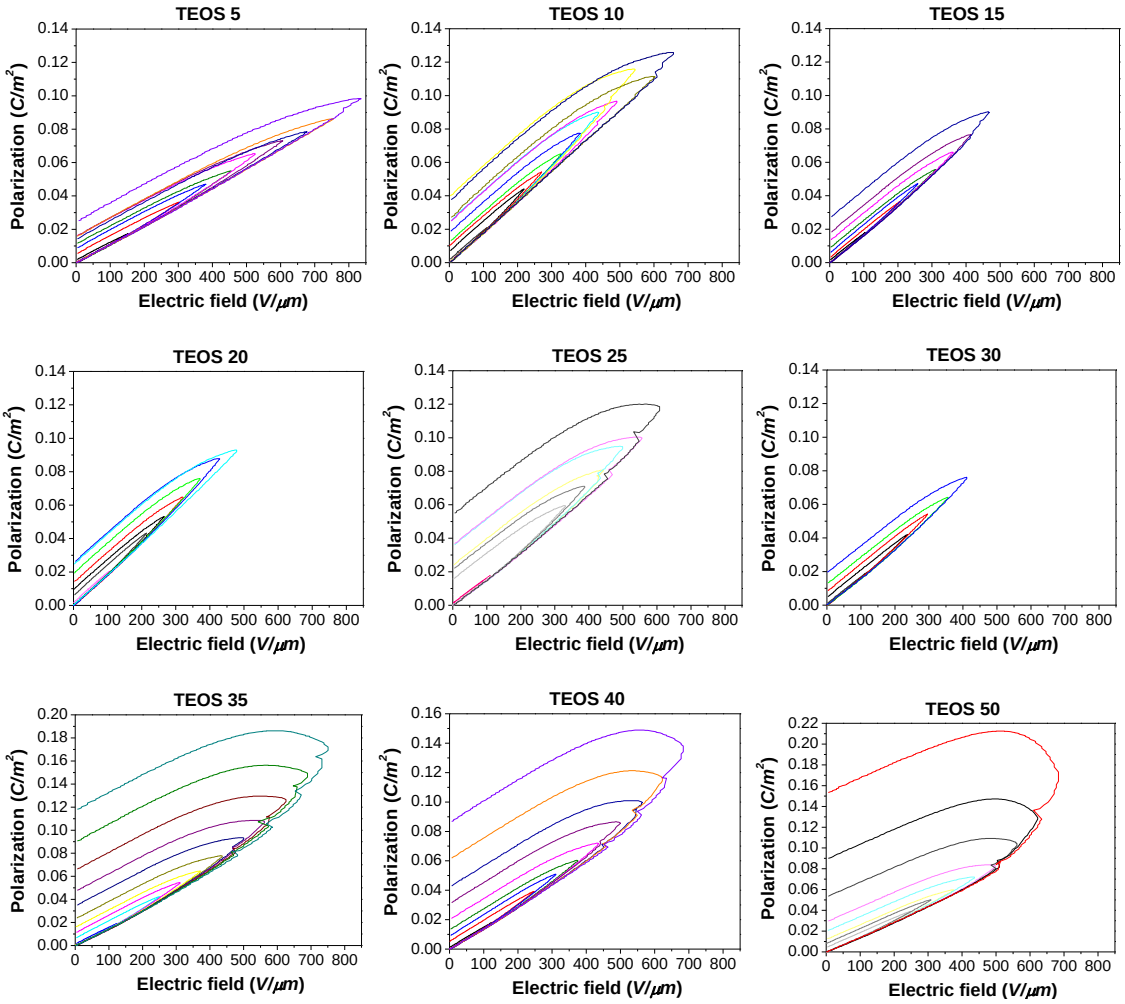

Figure 4.33 P-E loops of CNETMS-TEOS blends as a function of electric field. Numbers in labels on top of graph denote mol% of TEOS precursors.

4.6.2 CNETMS-CNEMDMS blends

The introduction of CNEMDMS into CNETMS would decrease the number of crosslinkings in sol-gel blends, as compared to neat CNETMS sol-gels, possibly providing more flexibility in crosslinked siloxanes networks and generating more free volumes in sol-gel matrix. Unlike TEOS inclusion, CNEMDMS sol-gel precursor has polar cyano moiety in its monomeric unit, so CNETMS-CNEMDMS blend system is free of decreasing polarizability because of the dilution of dipolar molecules.

Figure 4.34 summarizes frequency dependent dielectric properties of CNETMS-CNEMDMS sol-gel blends up to 34 mol% of CNEMDMS. Permittivities of blends exhibit marginal increase compared to neat CNETMS sol-gels, possibly due to increased rotational freedom of dipolar cyano groups because of loosened sol-gel networks. However, loss tangents of blends display the onset of dielectric relaxation even at room temperature, and the frequency of dielectric relaxation becomes higher with larger concentration of CNEMDMS. The dielectric relaxation behavior in loss tangent resembles that of CNPTES at elevated temperature (see Figure 4.25), which was ascribed to the increased rotational freedom of polar molecules due to longer alkyl chain spacer. In this regard, it can be postulated that the inclusion of CNEMDMS, which has less crosslinkable sites than CNETMS, decreases the total number of crosslinkings in CNETMS-CNEMDMS blend, increasing the flexibility of sol-gel networks in return. While the longer alkyl chain in CNPTES precursor would impart rotational mobility to polar cyano side groups, the inclusion of CNEMDMS would provide substantial structural flexibility in crosslinked siloxane backbone.

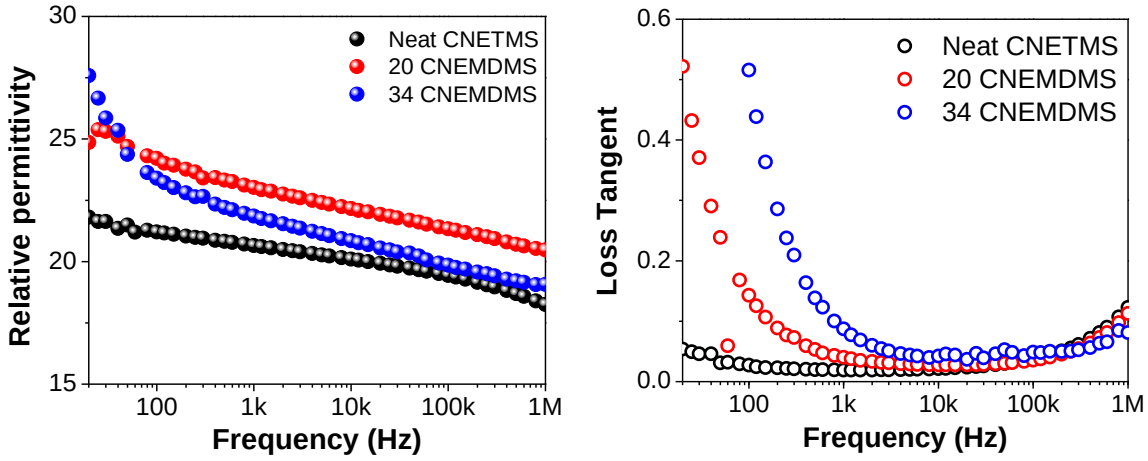

Figure 4.34 Field dependent (left) permittivity and (right) loss tangent of the sol-gel blends of CNETMS and CNEMDMS catalyzed with 0.1 N hydrochloride solution in 2-methoxyethanol as a solvent. Numbers in label represent the molar percent of CNEMDMS precursor.

It can be imagined that the structural flexibility in sol-gel networks provided by

CNEMDMS could result in the decrease of breakdown strength and reliability of breakdown failure. Indeed, the marginal decrease in E_B is observed as the mol% of CNEMDMS goes up, and more importantly, Weibull modulus drops from 8 to 4 when 34 mol% of CNEMDMS is incorporated, as compared to neat CNETMS. As already observed in CNPTES, in which increased rotational freedom resulted in high conductivity at low field region, the blend of CNEMDMS-CNETMS exhibit similar pattern with stiff initial rise below ± 10 V/μm followed by the saturation of current density as shown in Figure 4.36.

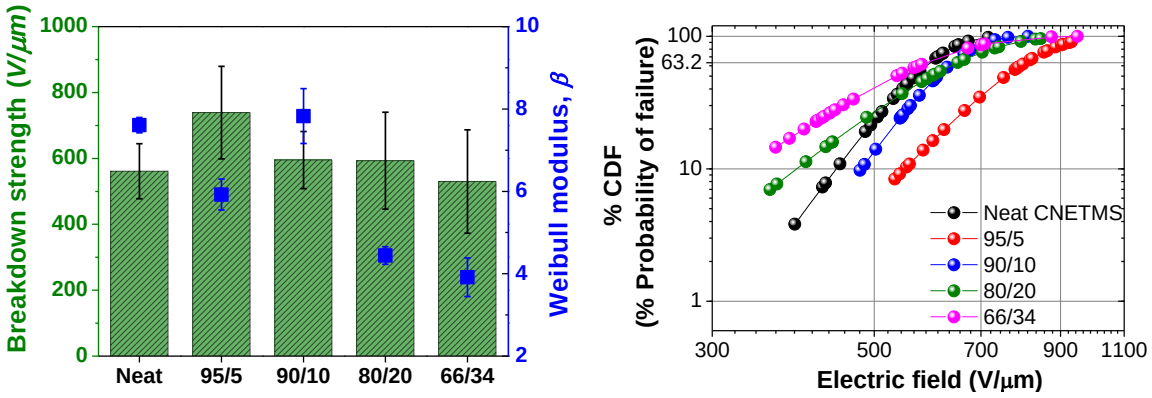

Figure 4.35 (left) Breakdown strength, E_B, and Weibull modulus including error bars (1σ) for the CNETMS-CNEMDMS blends as a function of molar percent of CNEMDMS; (right) Accumulated probability of failure of CNETMS-CNEMDMS blends as a function of electric field. All films are 1±0.05 μm thick.

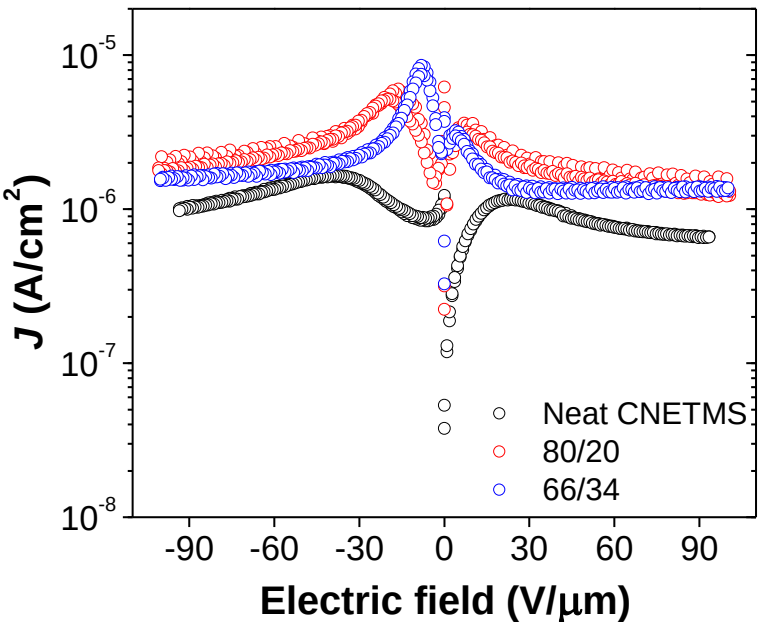

Figure 4.36 Leakage current profiles of CNETMS-CNEMDMS blends. Numbers in labels denote molar ratio of CNEMTMS to CNEMDMS precursors.

Energy storage performance of CNETMS-CNEMDMS blends exhibit gradual decrease in extraction efficiency as molar percent of CNEMDMS inclusion becomes larger (shown in Figure 4.37). Because of the substantially lowered efficiency, none of blends achieved $U_{max}^{PE}$of neat CNETMS films. As shown in Figure 4.38, P-E loops of blend films indicate significant electrical conduction with larger mol% of CNEMDMS precursor, eventually limiting energy storage performance of these blends. Although the energy storage performance of CNETMS-CNEMDMS blends is somewhat disappointing, it is worth noting that the flexibility of sol-gel networks can be enhanced by incorporating sol-gel precursor containing less crosslinkable sites into CNETMS. This approach would be potentially useful in the development of sol-gel materials containing mechanical flexibility while maintaining novel dielectric and electrical properties.

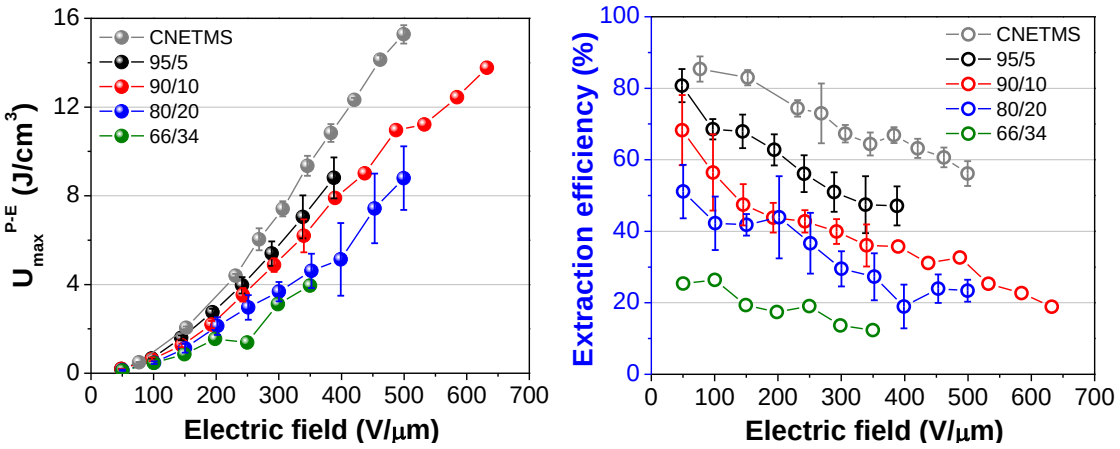

Figure 4.37 (left) U_{max}^{PE} and (right) energy extraction efficiency of CNETMS-CNEMDMS blend sol-gel films. Numbers in labels denote molar ratio of CNETMS to CNEMDMS precursors.

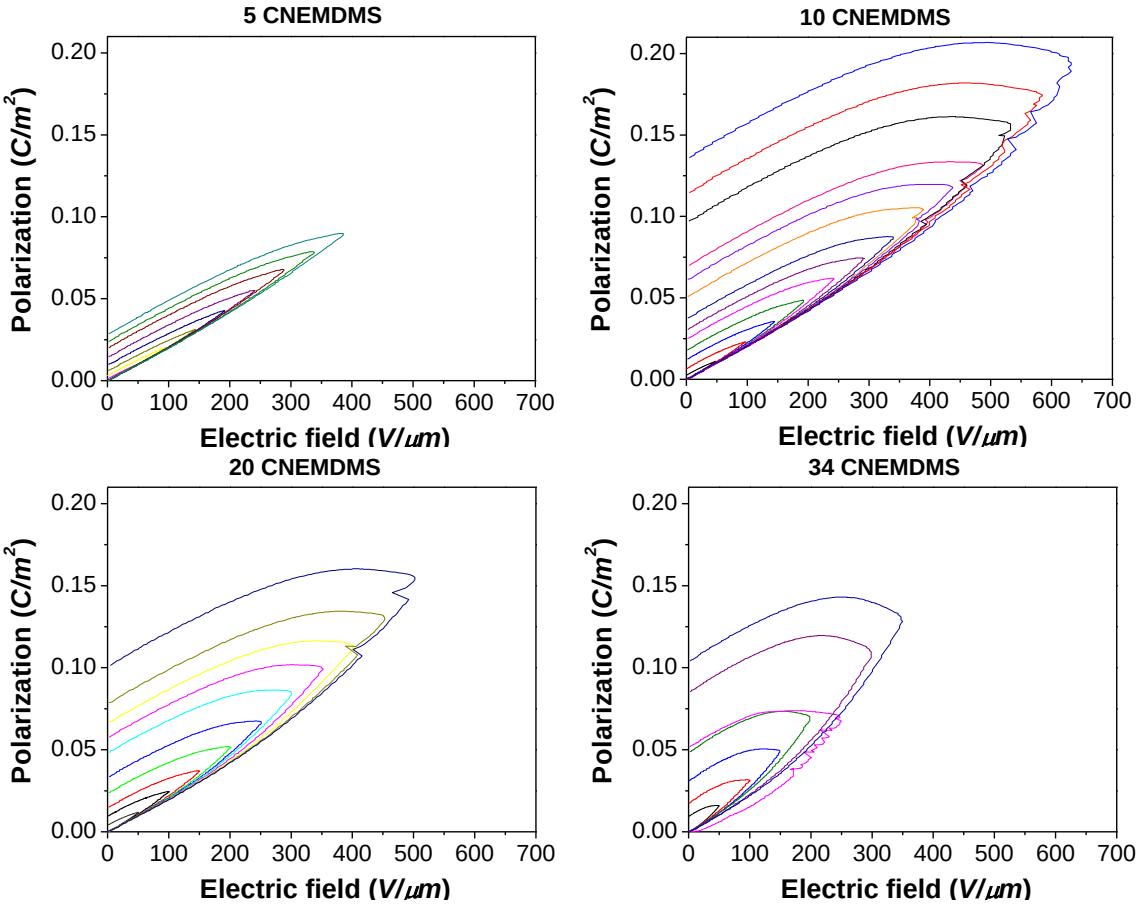

Figure 4.38 P-E loops of CNETMS-CNEMDMS blends. Numbers in labels on top of graph denote mol% of CNEMDMS precursors.

4.7 Conclusions

In this chapter, the fabrication of sol-gel dielectric films derived from a neat 2-cyanoethyltrimethoxysilane (CNETMS) precursor was demonstrated by using simple solution processing. The resultant sol-gel films exhibit a large relative permittivity of ~20 at 1 kHz and a relatively high dielectric strength of 650 V/μm for a 1.3 μm thick film. The large permittivity of CNETMS films is attributed to the orientational polarization of polar cyano groups, as supported by narrow loops and linear dielectric-like behavior in P-E measurements up to ~300 V/μm for CNETMS films. The combination of a dipole-reorientation polarization mechanism, sizeable permittivity, and moderately high dielectric strength has led to an extractable energy density of 7 J/cm^3 and an energy extraction efficiency of ~ 90% at 300 V/μm for CNETMS films. The polarization response of 1.3 μm thick CNETMS film departs from linear dielectric-like behavior at above 300 V/μm, as observed by widening of P-E loops and increased conduction current. This deviation from linear dielectric response compromises the potential for CNETMS sol-gel dielectric films for use in energy storage and pulsed power applications.

The later part of the chapter focused on the investigation of the effects of processing variables on the dielectric, electrical, and energy storage properties of resultant sol-gel films. The variables studied involve moisture, solvent during sol-gel reaction, the length of alkyl spacer between siloxane backbone and polar cyano molecules, and crosslinking density. It has been found that, 1) the physically adsorbed water molecules increased the leakage current of sol-gel films by an order of magnitude; 2) the use of high boiling point solvent in sol-gel reaction decreased the thickness of resultant sol-gel films, but seemed to make sol-gel films susceptible to charge carrier injection at fields above ~200 V/μm, leading to substantially decreased energy

storage density and extraction efficiency; 3) longer alkyl spacer attached to polar cyano groups provided more rotational freedom to polar molecules, which was reflected in increased permittivity and shorter relaxation time in temperature dependent dielectric spectroscopy; 4) varying crosslinking density of sol-gel materials resulted in substantial change in structural, dielectric and electrical properties such as thickness, permittivity, breakdown strength, leakage current, and polarization response.

In chapter 5, the tunneling barrier layer will be introduced in order to mitigate electrical conduction in CNETMS sol-gel films at high electric fields, which turned out to be the most critical factor that accounts for the compromise in the energy storage performance of sol-gel dielectrics.

CHAPTER 5

EFFECT OF TUNNELING BARRIER LAYER ON DIELECTRIC PROPERTIES OF SOL-GEL FILM CAPACITORS

5.1 Theory of Field-induced Thermionic and Field Emission

When an insulating film is brought between two metal electrodes, the equilibrium condition for the alignment of Fermi energy level requires that the top of the energy gap (conduction band bottom) of the insulator be positioned above the Fermi energy level of the metal electrodes, as shown in Figure 5.1. Therefore, the presence of insulating film naturally introduces a potential barrier that impedes the flow of charge carriers between the metal electrodes.

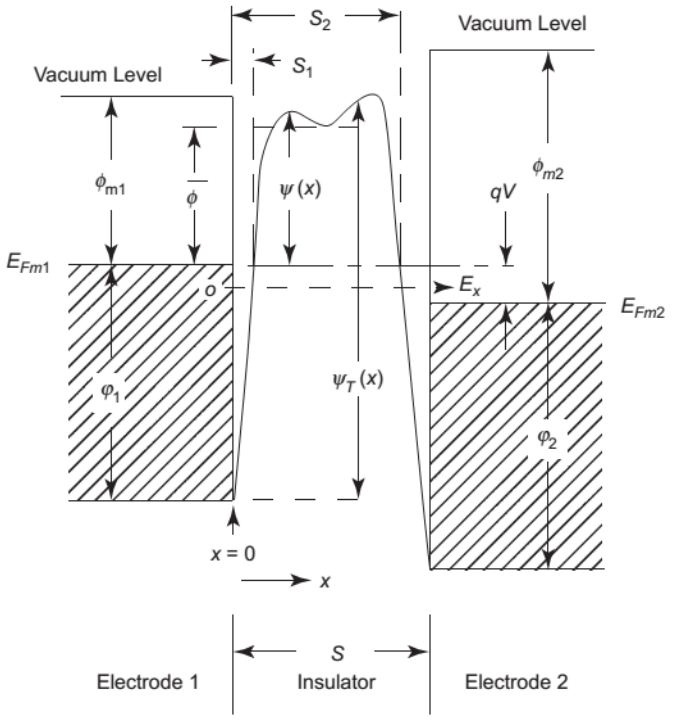

Figure 5.1 The schematic illustration of a potential energy barrier in insulating film between two metal electrodes. Reproduced with permission.[4] Copyright © 2004, Elsevier.

The electronic current can flow through the insulating region if 1) the electrons in the

electrodes have enough thermal energy to surmount the potential barrier and flow in the conduction band of the insulating film; 2) the barrier is thin enough to permit its penetration by the electric tunnel effect.[117] The first case refers to field-enhanced thermionic emission or Schottky effect, and the second refers to field emission or cold emission by quantum mechanical tunneling. The difference between the two mechanisms is whether thermal energy is involved in the emission or the injection process of charge carriers.

The first type of charge carrier emission, as the name implies, represents the flow of charge carriers over a potential energy barrier owing to thermal energy given to carriers. Particularly, in electron emission devices, the electron emitter is biased negatively relative to its surroundings, creating an electric field at the emitter surface. Under the application of electric field, the potential energy barrier is lowered by the combination of the electrostatic force originated from applied field and image charges. Figure 5.2 illustrates the lowering of potential barrier by the application of electric field and the image force, which is originated from images charges building up in the metal electrode as charge carriers approach the metal-insulator interface. The effect of the image force is to reduce the area of the potential energy barrier by rounding off the corners and reducing the width of the barrier and hence, increasing the flow of current between the electrodes.

The profile of a potential energy barrier, $\Psi(x)$, is expressed by

$$\Psi(x) = \phi_B - qEx - \frac{q^2}{16\varepsilon_r\varepsilon_o x} \qquad \text{Equation 5.1}$$

where ϕ_B is the potential barrier height under zero electric field, which is work function of metal electrode, *x* is the distance from the metal-insulator interface, and *E* is an applied electric field. The second term represents electrostatic force associated with an applied

electric field, and the third term refers to electrostatic force created by image charges building up in the metal electrode as charge carriers approach the metal-insulator interface. It is important to note that the permittivity of insulator, ε_r, which is in the third term, becomes nonlinear when an electric field increases.

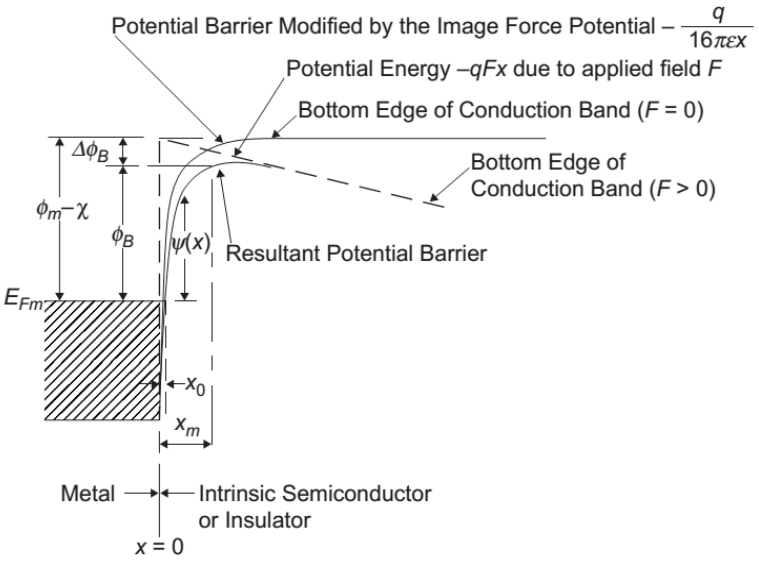

Figure 5.2 The schematic illustration of the lowering of a potential energy barrier by the combination of applied field and image force. Reproduced with permission.[4] Copyright © 2004, Elsevier.

The second type of emission or injection refers to a quantum mechanical tunneling effect, which deals with the probability of an electron penetrating a potential barrier $\Psi(x)$, which is assumed to be only in the x-direction as shown in Figure 5.1

For the arbitrary shape of a potential barrier instead of the rectangular shape of a potential barrier, the penetration probability or barrier transparency, $D(E_x)$, of an electron is given by the WBK (Wentzel, Kramers, and Brillouin) approximation,[4, 117]

$$D(E_x) = exp\left\{-\frac{4\pi}{h}\int_{x_1}^{x_2}[2m(\Psi(x) - E_x)]^{\frac{1}{2}}dx\right\} \qquad \text{Equation 5.2}$$

where m is mass of electron, h is Planck's constant, and $E_x = mv_x^2/2$, is the energy

component of the incident electron in the *x* direction. It can be seen in Equation 5.2 that the penetration probability decreases exponentially with the width of a potential barrier.

The number N_1 of electrons tunneling through a potential barrier from electrode 1 to 2 is given by,

$$N_1 = \int_0^{v_m} v_x n(v_x) D(E_x) dv_x = \frac{1}{m} \int_0^{E_m} n(v_x) D(E_x) dv_x \qquad \text{Equation 5.3}$$

where $E_m$is the maximum energy of the electrons in the electrode, and $n(v_x)dv_x$ is the number of electrons per unit volume with velocity between v_x and $v_x + dv_x$. For an isotropic velocity distribution, the number of electrons per unit volume with velocity between the infinitesimal limit is given by,

$$n(v)dv_x dv_y dv_z = \left(\frac{2m^4}{h^3}\right) f(E) dv_x dv_y dv_z \qquad \text{Equation 5.4}$$

where $f(E)$ is the Fermi-Dirac distribution function. From Equation 5.4,

$$n(v_x) = \frac{2m^4}{h^3} \int \int_{-\infty}^{\infty} f(E) dv_y dv_z = \frac{4\pi m^3}{h^3} \int_0^{\infty} f(E) dE_r \qquad \text{Equation 5.5}$$

Substituting Equation 5.5 in 5.3 yields,

$$N_1 = \frac{4\pi m^2}{h^3} \int_0^{E_m} D(E_x) dE_x \int_0^{\infty} f(E) dE_r \qquad \text{Equation 5.6}$$

note that Equation 5.6 is expressed in polar coordinates.

The number N_2 of electrons tunneling back from electrode 2 to 1 is also determined in a similar way. The penetration probability $D(E_x)$ is the same in either direction, and if electrode 2 is at a positive potential *V* with respect to electrode 1, the Fermi-Dirac distribution function should be $f(E + eV)$. Thus,

$$N_2 = \frac{4\pi m^2}{h^3}\int_0^{E_m} D(E_x)dE_x \int_0^{\infty} f(E+eV)dE_r \qquad \text{Equation 5.7}$$

The net flow of electrons, $N = N_1 - N_2$, through a potential barrier is,

$$N = \int_0^{E_m} D(E_x)dE_x \times \left\{\frac{4\pi m^2}{h^3}\int_0^{\infty}[f(E) - f(E+eV)]dE_r\right\} \qquad \text{Equation 5.8}$$

Let us denote,

$$\xi_1 = \frac{4\pi m^2}{h^3}\int_0^{\infty} f(E)dE_r,\ \xi_2 = \frac{4\pi m^2}{h^3}\int_0^{\infty} f(E+eV)dE_r \qquad \text{Equation 5.9}$$

Then Equation 5.8 becomes

$$J = \int_0^{E_m} D(E_x)\xi dE_x \qquad \text{Equation 5.10}$$

where $\xi = \xi_1 - \xi_2$. Equation 5.10 is the tunneling current through a potential barrier created by an insulating film placed between two metal electrodes.

Simmons derived a generalized formula for the tunneling current through arbitrary shape of a potential barrier, which can be written as,[117]

$$J = J_o\left\{\bar{\varphi}\exp\left(-A\bar{\varphi}^{\frac{1}{2}}\right) - (\bar{\varphi}+eV)exp\left[-A(\bar{\varphi}+eV)^{\frac{1}{2}}\right]\right\} \qquad \text{Equation 5.11}$$

where $\bar{\varphi}$ is the mean barrier height above Fermi level of the negatively biased electrode

$$\bar{\varphi} = \frac{1}{\Delta s}\int_{S_1}^{S_2}\varphi(x)dx \qquad \text{Equation 5.12}$$

and

$$J_o = e/2\pi h(\beta\Delta s)^2,\ A = (\frac{4\pi\beta\Delta s}{h})(2m)^{\frac{1}{2}} \qquad \text{Equation 5.13}$$

where β is defined as correction factor.

At low voltage range, since $\bar{\varphi} \gg eV$, Equation 5.11reduces to

$$J = J_L \bar{\varphi}^{\frac{1}{2}} V exp(-A\bar{\varphi}^{\frac{1}{2}}) \qquad \text{Equation 5.14}$$

where

$$J_L = \left[(2m)^{\frac{1}{2}}/\Delta s\right](\frac{e}{h})^2 \qquad \text{Equation 5.15}$$

Since eV is very small, $\bar{\varphi}$ approximates to be zero-voltage barrier height. Therefore, in the low voltage regime, tunneling current *J* is a linear function of *V* as shown in Equation 5.14.

At high voltage range, the Fermi energy level of electrode 2 is lower than the conduction band bottom of electrode 1. Under such conditions, there is no electron flow from electrode 2 into 1 due to the lack of empty states. Therefore, current is expressed as

$$J = \frac{2.2e^3F^2}{8\pi h\varphi_0} exp\left[-\frac{8\pi}{2.96heF}(2m)^{\frac{1}{2}}\varphi_0^{\frac{3}{2}}\right] \qquad \text{Equation 5.16}$$

In principle, tunneling current can be computed by using current equations (Equation 5.15 and 16) with given system parameters such as work function of electrode material, electric field, and contact area. However, it should be noted that these approximated equations for tunneling current assumes low temperatures, so that the contribution of thermal current is totally neglected.

In addition to the two mechanisms for charge carrier emission, field-enhanced thermionic emission and field emission, there are many sources that could affect the profile of a potential barrier, leading to the change of tunneling probability and leakage current profile of the insulating film. These sources involve space charge and impurity in the bulk of insulator, and chemi- or physisorbed dipoles on the surface of either metal or insulator.[118] It may be postulated that these sources could distort the

energy band structure near the interface, or could create localized states having energies distributed in the forbidden range within the energy band gap, as similar to the case of so called Fermi energy pinning by surface states in semiconductor.[119]

In summary, two cases of charge carrier emission are shown in which charge carriers could escape from a metal electrode to an insulating film through an arbitrary-shaped potential energy barrier *via* field-induced thermionic emission and field emission by means of purely quantum mechanical tunneling. Based on these theories, the approach of charge blocking layer or tunneling barrier layer is introduced to mitigate electrical conduction in dielectric films based on 2-cyanoethyltrimethoxysilane (CNETMS) sol-gel precursor. The emphasis will be on the selection of materials for tunneling barrier, and the engineering of the width and the height of such barrier in order to optimize the barrier property.

5.2 Materials and Deposition Method for a Barrier Layer

5.2.1 Materials

As indicated in Equation 5.1, the profile of a potential energy barrier is a function of work function of metal electrode, applied electric field, permittivity of barrier material, and the width of a barrier layer. The candidate material for a barrier layer is chosen considering these factors: processability, quality of resultant barrier layer, and permittivity. Table 5.1 summarizes materials used for a barrier layer involving their permittivity, the method of film processing, and thickness range of deposited layer.

The organic precursors and chemicals: amorphous fluoropolymer, CYTOP (CTL-809M, Bellex International Corporation), poly(*p*-phenylene oxide) (PPO, Sigma-Aldrich), methylphosphonic acid, propylphosphonic acid, hexylphosphonic acid, *n*-

octylphosphonic acid, octadecylphosphonic acid (all from Sigma-Aldrich), and 1-dodecylphosphonic acid (Alfa Aesar) were used as received.

Table 5.1 Permittivities, process methods, and thicknesses of materials utilized for a barrier layer on CNETMS sol-gel films.

	Material	Permittivity	Process	Thickness
Dielectric layer	CNETMS sol-gel	~20	Spin casting	1.0 to 1.3 μm
Oxide barrier layer	SiO_2	3.9 [44]	E-beam	20 to 50 nm
	Al_2O_3	9 [44]	ALD at 110ºC	
	ZrO_2	25 [44]	ALD at 130ºC	
Organic barrier layer	CYTOP	2.0 [120]	Spin casting	20 to 176 nm
	Poly(*p*-phenylene oxide)	2.8 [83]	Spin casting	50 to 200 nm
	Alkylphosphonic acid	2.5 [121, 122]	Dipping	up to 2.2 nm

Various oxide and organic materials were selected depending on process method, permittivity, and available thickness range. Figure 5.3 shows some of organic precursors utilized as a barrier layer.

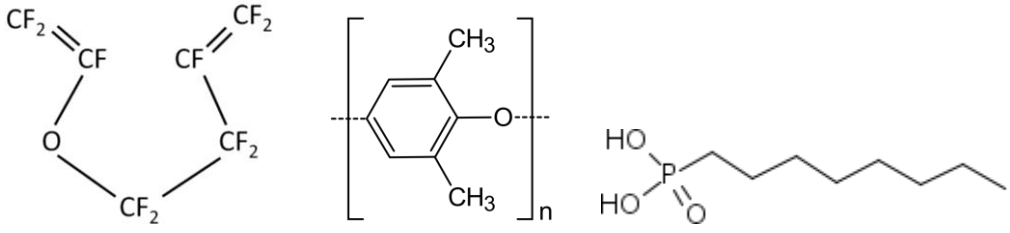

Figure 5.3 The chemical structure of (from left to right) amorphous fluoropolymer, CYTOP, poly(*p*-phenylene oxide) (PPO), and octylphosphonic acid (OPA).

5.2.2 Deposition methods

For SiO_2 barrier layer, electron beam physical vapor deposition technique was used. Atomic layer deposition method was utilized to grow Al_2O_3 and ZrO_2 oxide layers at 110 ºC and 130 ºC. All depositions followed the predetermined recipe for target thickness.

Organic barrier layers were spun on top of CNETMS sol-gel films from the solution casting method with predetermined concentration and spin speed for target thickness. CYTOP layers whose thicknesses ranging from 20 to 175 nm were produced by varying spin speeds and CYTOP concentrations.[120] PPO layer was prepared in a similar way. After PPO coating on CNETMS sol-gel films, bilayer films were subjected to thermal treatment at 120 ºC for three hours to remove residual toluene used as a solvent.

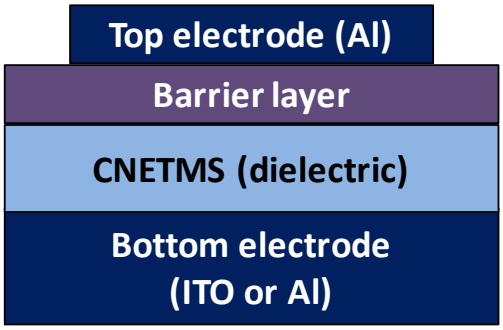

Figure 5.4 The geometry of sol-gel film capacitor containing a barrier layer.

5.3 Oxide Barrier Layer: SiO_2, Al_2O_3, ZrO_2

The introduction of a layer that exhibits an appreciable barrier to electrical conduction can lead to an increase in the breakdown strength of a material or multilayer film, by decreasing charge transport *via* large bandgaps, charge trapping sites and scattering centers.[31, 120, 123, 124] Furthermore, the presence of such a charge blocking layer may also lead to a decrease in the probability of electrical breakdown by partial filling and

covering of pores exposed at the surface of a sol-gel dielectric thin film.

In multi-layered dielectrics, electric field is distributed with respect to the relative permittivity and the thickness of each layer. When it comes to the design of multi-layered dielectrics, the magnitude of a local electric field is critical because the local field concentrated in one layer can bring about catastrophic breakdown.[125] To assess the effective permittivity and the local field distribution of the each layer in multi-layered dielectrics, a parallel-plate capacitor consisting of two layers with different the relative permittivity and thickness is depicted in Figure 5.5. Because the presence of free charges between the two layers can be neglected, the displacement vector D_1 and D_2 are equal. Using this condition, following Equations 5.17 and 18 are derived and these equations define the effective permittivity, ε_{eff}, the and local field distribution of the each layer in multi-layered dielectrics.

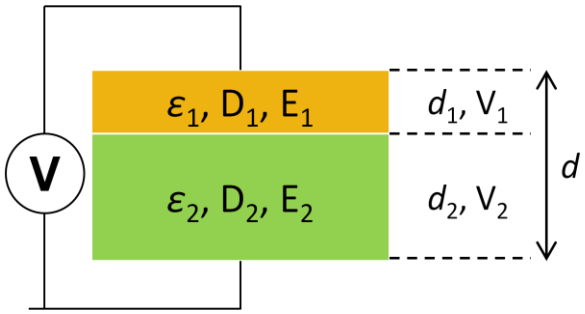

Figure 5.5 Schematic of parallel-plate capacitor consisting of two layers with different permittivity and thickness.[3]

$$E_1 = V/\varepsilon_1\left(\frac{d_1}{\varepsilon_1}+\frac{d_2}{\varepsilon_2}\right),\ E_2 = V/\varepsilon_2\left(\frac{d_1}{\varepsilon_1}+\frac{d_2}{\varepsilon_2}\right) \qquad \text{Equation 5.17}$$

$$\varepsilon_{eff} = 1/\left(\frac{d_1/d}{\varepsilon_1}+\frac{d_2/d}{\varepsilon_2}\right) \qquad \text{Equation 5.18}$$

Figure 5.6 shows measured and calculated $\varepsilon_{eff}$of oxide/CNETMS bilayer films. Although Al_2O_3/CNETMS bilayer films display a good agreement in measured and calculated values, in other two bilayer systems ε_{eff} measured larger than the one from

calculation. It could be attributed to the varied thickness of the barrier layer due to the deviated growth rate of deposited layer on top of CNETMS sol-gel film.

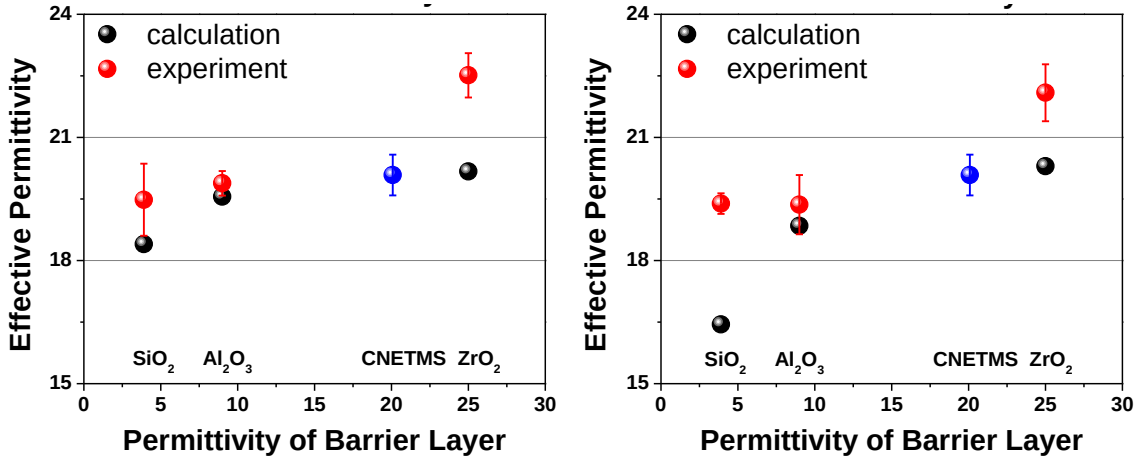

Figure 5.6 Effective permittivity, ε_{eff}, of oxide/CNETMS bilayer films for (left) 20 nm and (right) 50 nm of barrier layer. Calculated and measured ε_{eff} are shown in black and red dots, respectively.

Figure 5.7 shows the distribution of local electric field in each layer in bilayer dielectrics determined from Equation 5.17. It is readily seen that electric field is partitioned in such a way that thin barrier layer holds much higher local field than thicker CNETMS layer. This local field concentration could bring about premature breakdown events, leading to lowered failure reliability of film capacitor.

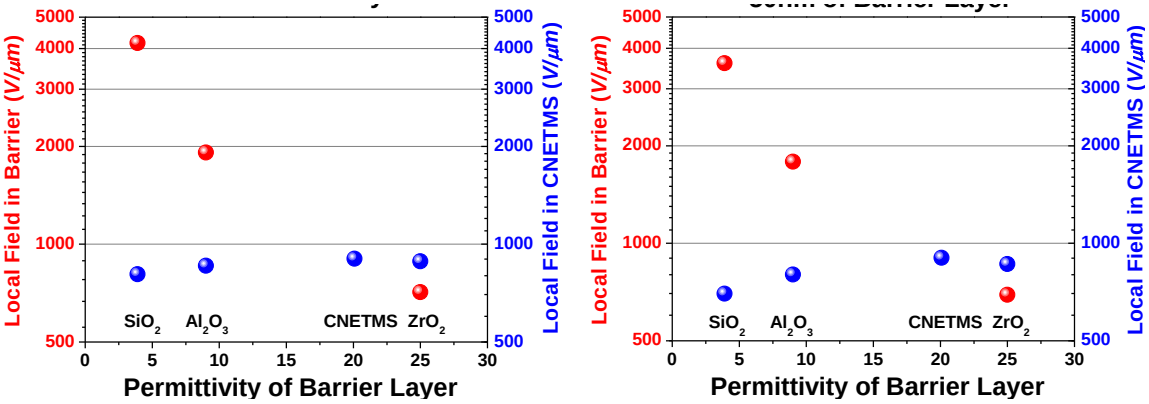

Figure 5.7 Calculated local electric field in a barrier layer (in red) and CNETMS film (in blue) for (left) 20 nm and (right) 50 nm of barrier layer when bilayer films are under the influence of an applied voltage of 850 V.

Figure 5.8 sums up dielectric properties of oxide/CNETMS bilayer dielectrics. Permittivity of bilayer films were only marginally affected by the inclusion of oxide barrier layer, ranging 19.4 to 22.5. E_B of bilayer films determined from Weibull analysis also shows marginal variation from neat CNETMS film. For Weibull modulus, which represents the scattering of breakdown strength of dielectric material, of bilayer films exhibit gradual increase with thicker barrier layer compared to neat CNETMS film. Although there is an exception with the 50 nm Al_2O_3 barrier layer, the gradual increase in Weibull modulus of bilayer films can be correlated with the reduced probability of premature breakdown events, possibly due to the decreased charge transport by the inclusion of barrier layer.

The effect of oxide barrier layer is more prominent when it comes to energy storage performance of bilayer films shown is Figure 5.9 and Table 5.2. First of all, U_{max}^{PE} of bilayer films with 20 nm of barrier layer exhibit much reduced extractable energy density compared to 13.1 J/cm^3 from neat CNETMS. However, as the barrier layer becomes thicker to 50 nm, U_{max}^{PE} increases substantially and reaches 20.6 J/cm^3 for ZrO_2/CNETMS bilayer films, which is around 60% larger than neat CNETMS.

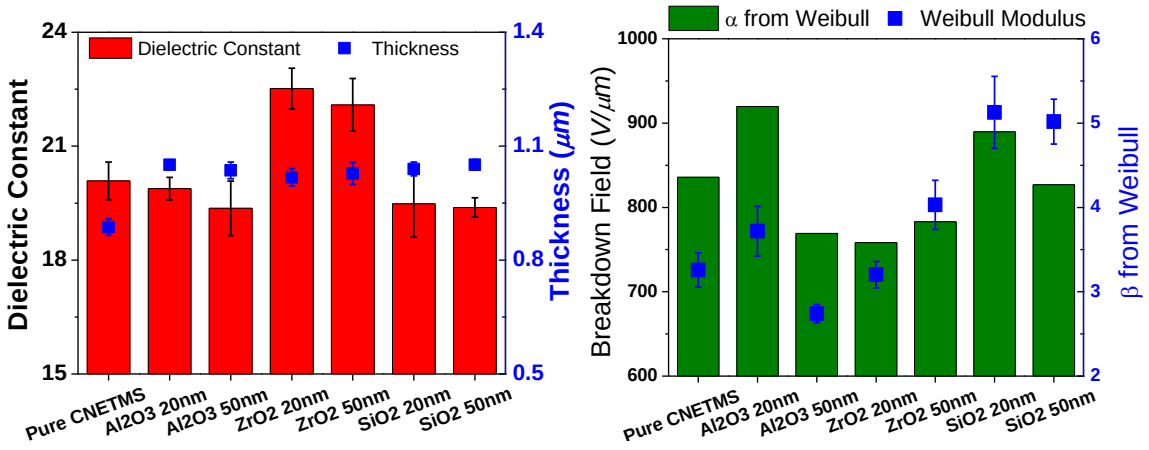

Figure 5.8 (left) Breakdown strength and Weibull modulus, (right) dielectric constant and thickness of CNETMS and oxide/CNETMS bilayer films.

For energy extraction efficiency, we compare all systems at ~300 V/μm because at this field strength CNETMS sol-gel films start to exhibit the contribution of electrical conduction, causing the widening of P-E loops. It should be noted that neat CNETMS utilized for this oxide barrier layer experiment was synthesized with 2-methoxyethanol. That is why the energy extraction efficiency of neat CNETMS in Table 5.2 is 49% (for detailed discussion about the effect of solvent on CNETMS films, see chapter 4.4). All bilayer films display enhanced extraction efficiency compared to neat CNETMS, and there is also a marginal increase in efficiency with thicker oxide barrier layer with the exception of 50 nm ZrO_2 layer. Along with the improvement of Weibull modulus, the increase in $U_{max}^{PE}$and extraction efficiency of bilayer films suggests that there must be a reduction of charge transport by oxide layers, which may be due to the reduced charge carrier injection from metal electrode to insulating CNETMS film through the potential energy barrier of oxide layers.

It is worthwhile to note that the lowering of potential energy barrier is inversely proportional to the permittivity of insulating film (see Equation 5.1), which is the oxide barrier layer in our bilayer configuration. Actually, U_{max}^{PE} of bilayer films scales with the permittivity of individual oxide layer, *i.e*., 3.9, 9, and 25 for the permittivity of SiO_2, Al_2O_3, and ZrO_2, respectively; 14.3, 16.2, and 20.6 J/cm^3 of U_{max}^{PE} for the bilayer films with respective oxide barrier layer. Therefore, 20.6 J/cm^3 of U_{max}^{PE} achieved in 50 nm ZrO_2/CNETMS bilayer films can be attributed to the mitigation of charge carrier injection or transport *via* the inclusion of potential barrier layer.

Table 5.2 The summary of dielectric properties of oxide/CNETMS bilayer films.

Material	Permittivity	E_B (V/μm) from Weibull analysis	Weibull modulus	U_{max}^{PE} (J/cm^3)	Energy extraction efficiency (at ~300 V/μm)
Neat CNETMS (MeoEtOH)	20.1	836	3.2	13.1	49%
20 nm SiO_2 / CNETMS	19.5	890	5.1	7.3	62%
50 nm SiO_2 / CNETMS	19.4	827	5.0	14.3	73%
20 nm Al_2O_3 / CNETMS	19.9	920	3.7	11.7	60%
50 nm Al_2O_3 / CNETMS	19.4	769	2.7	16.2	76%
20 nm ZrO_2 / CNETMS	22.5	758	3.2	5.9	65%
50 nm ZrO_2 / CNETMS	22.1	783	4.0	20.6	61%

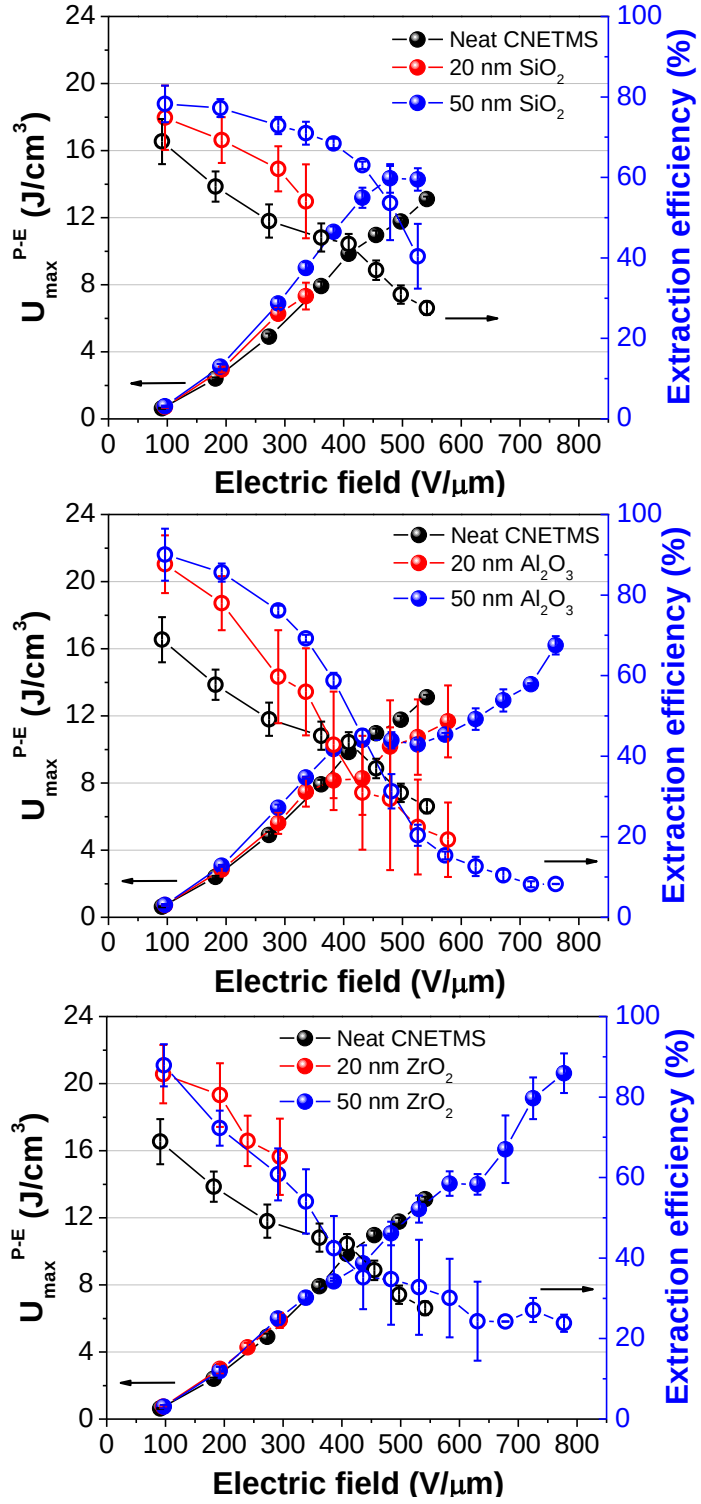

Figure 5.9 U_{max}^{PE}(left Y-axis) and energy extraction efficiency (right Y-axis) of (from top to bottom) SiO_2, Al_2O_3, ZrO_2 blocking layer with CNETMS films. Thickness of oxide layer in bilayer films ranges from 0 (neat CNETMS) to 50 nm.

5.4 Organic Barrier Layer: CYTOP and Poly(*p*-phenylene oxide)

Organic materials are easier to be processed into a barrier layer than inorganic oxide materials, which usually require vacuum deposition techniques. Additionally, the thickness of a barrier layer can be more easily controlled by changing the concentration of organic precursor and the speed of spin casting process.

5.4.1 CYTOP/CNETMS bilayer films

An amorphous fluoropolymer, CYTOP, has been shown by Granstrom *et al*., to prevent moisture absorption significantly.[124] In a bilayer structure utilizing CYTOP, one may accomplish the following: 1) by minimizing moisture absorption in the devices, the breakdown event by the partial discharge from moisture may be suppressed. 2) CYTOP (being a high work function insulator) may also reduce or prevent the injection of charge carriers from the top Al electrode into the dielectric, thus potentially decreasing the probability of electrical spurs.

The RMS roughness of the top surface of CYTOP/CNETMS bilayer structures obtained from AFM images varied from 1.44 nm, 1.01 nm, 0.81 nm, 0.65 nm, 0.63 nm for CYTOP thicknesses of 20 nm, 45 nm, 72 nm, 143 nm, and 176 nm, respectively (images shown in Figure 5.10). The surface roughness of CYTOP/CNETMS bilayer films shows a general trend of decreasing roughness with thicker CYTOP layer (summarized in Table 5.3).

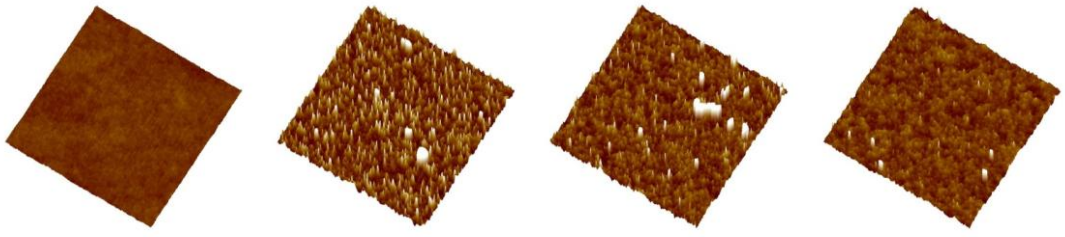

a) b) c) d)

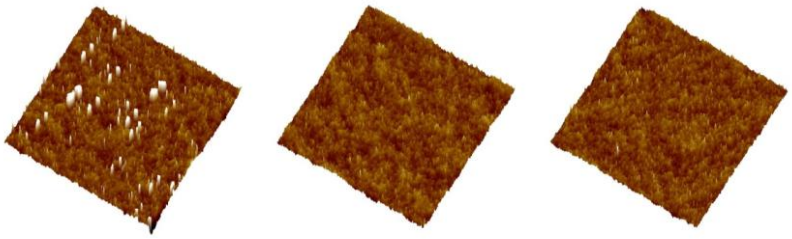

e) f) g)

Figure 5.10 AFM topographical images of CYTOP/CNETMS bilayer films: a) 0 nm, b) 20 nm, c) 45 nm, d) 72 nm, e) 126 nm, f) 143 nm, and g) 176 nm of CYTOP layer on 3.5μm thick CNETMS (z scale and scan size is 10 nm and 5μm by 5μm, respectively).

Table 5.3 Root mean squared roughness of CYTOP/CNETMS bilayer films determined from AFM images shown in Figure 5.10.

Thickness of CYTOP (nm)	Roughness (nm)	Thickness of CYTOP (nm)	Roughness (nm)
0	0.27	126	1.69
20	1.44	143	0.65
45	1.01	176	0.63
72	0.81		

The measured permittivity, ε_r, and loss tangent as a function of frequency for CNETMS films and CYTOP/CNEMTS bilayer films are shown in Figure 5.11. The effective permittivity of the CYTOP/CNETMS bilayer film is expected to decrease compared to that of neat CNETMS films due to the low ε_r of CYTOP (~2.0)[120]. Indeed, the measured ε_r of the CYTOP/CNETMS bilayer films decreased with increasing thickness of the CYTOP (see Figure 5.12 for the comparison of measured and calculated $\varepsilon_r$of bilayer films). The decrease in ε_r would reduce the energy density of the bilayer films especially with thicker CYTOP layer, unless this effect is well compensated through the enhancement of breakdown strength of the bilayer.

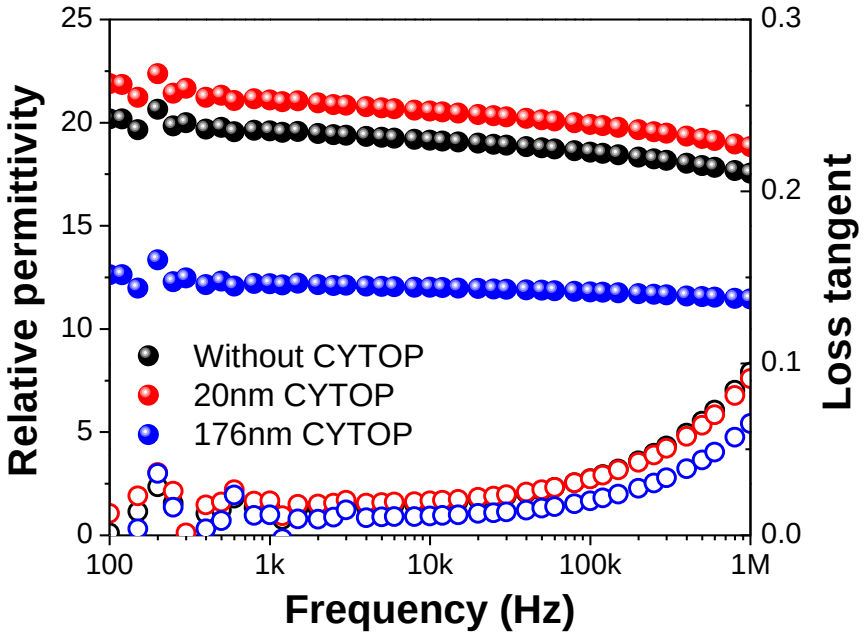

Figure 5.11 Frequency dependence of relative permittivity (solid points) and loss tangent (hollow points) of CNETMS (black symbols) and CYTOP/CNETMS bilayer films with 20 nm (red symbols) and 176 nm (blue symbols) thick CYTOP layers. The thickness of neat CNETMS film is 1.3 μm.

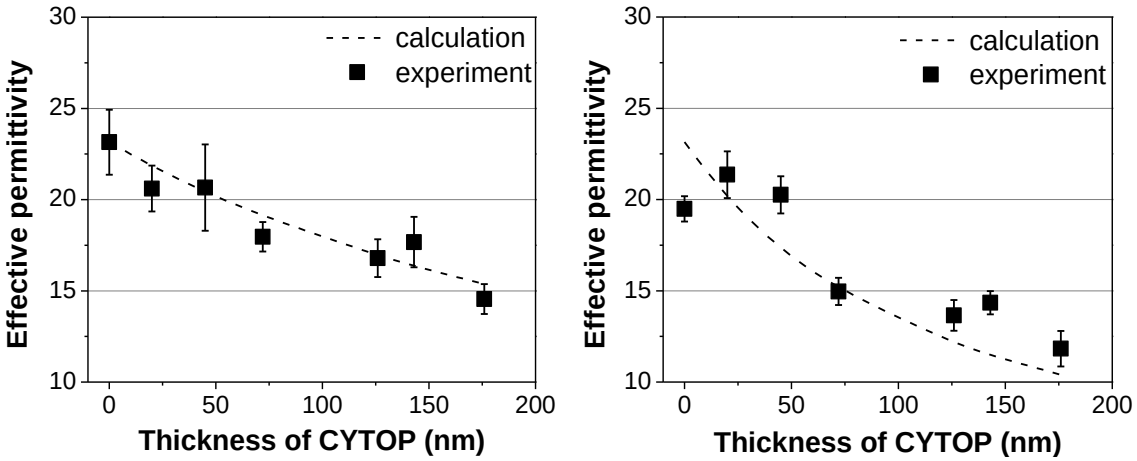

Figure 5.12 Comparison of calculated and measured effective permittivity of CYTOP/CNETMS bilayer films. (left) for 3.5 μm thick CNETMS and (right) for 1.3 μm thick CNETMS films.

The effect of CYTOP layer thickness on E_B and Weibull modulus of CYTOP/CNETMS bilayer films is summarized in Figure 5.13. We have learned that CNETMS sol-gel films have thickness dependence on its breakdown strength (see Figures 4.14 and 15). For this

reason, the overall E_B of CYTOP/CNETMS bilayer films with 1.3 μm thick CNETMS (Figure 5.13b) are much higher than those with 3.5 μm thick CNETMS (Figure 5.13a). For both cases, Weibull modulus of the bilayer films indicate a clear trend that exhibits initial drop when the thickness of CYTOP layer is below 50 nm, followed by gradual increase with thicker CYTOP layer, which reaches values up to ~11 with 176 nm CYTOP on 1.3 μm thick CNETMS. The initial drop of Weibull modulus with the CYTOP thickness below 50 nm can be rationalized in that charges at the interface of thinner porous films are more likely to participate in electrical conduction that can facilitate catastrophic breakdown events. The increase of Weibull modulus with CYTOP layer thicker than 50 nm can be attributed to the improved surface roughness of the bilayer films as observed by AFM images (Figure 5.10). In CYTOP/CNETMS bilayer films, the CYTOP coating may serve to scatter and trap charges in the bilayer films, which may facilitate the reduction of the failure probability and improve the breakdown statistics.[31, 123]

Unlike Weibull modulus, E_B of the bilayer films with 1.3 μm thick CNETMS (shown in right Figure 5.13b) does not seem to highly depend on the thickness of CYTOP. However, the gradual increase of E_B in the bilayer films with 3.5 μm thick CNETMS, which is displayed in Figure 5.13a, suggests that the charge blocking action of the CYTOP layer could limit charge injection into the CNETMS and thereby increasing the breakdown strength of the bilayer films. These results are consistent with the reported trend of reduced leakage current with an increase in the thickness of CYTOP films,[120] which would lead to a lower probability of catastrophic breakdown events.

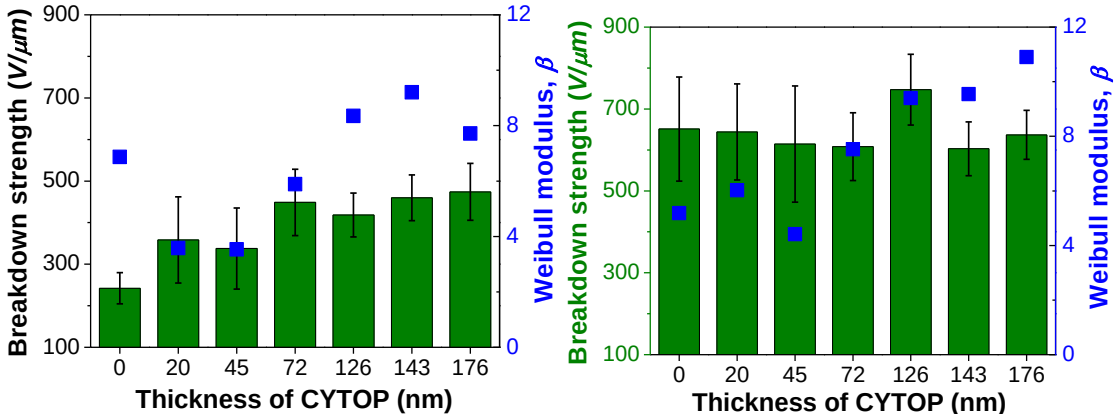

Figure 5.13 Breakdown strength (E_B) and Weibull modulus of CYTOP/CNETMS bilayer films (a) from 3.5 μm thick and (b) from 1.3 μm thick CNETMS films. The error bars represent the standard deviation (1σ) of the average breakdown strength obtained from 12-20 devices.

Accordingly, the influence of the CYTOP layer is more pronounced for the thicker CNETMS film. We would expect the charge-blocking properties of CYTOP to be more effective at the lower fields where the thick CNETMS films undergo breakdown, thus leading to an increase in the bilayer breakdown strength. On the other hand, for the thinner CNETMS films the breakdown strength is sufficiently large that, on the path to breakdown, fields are reached where CYTOP no longer functions well as a charge blocking layer. AFM images show that CYTOP/CNETMS bilayers (Figure 5.10) with a thicker CYTOP layer possesses lower surface roughness on CNETMS films, leading to more effective charge blocking effect by CYTOP. Granstrom *et al*., have previously shown that the surface roughness of CYTOP thin films increased by an order of magnitude as the thickness decreased from 400 to 100 nm.[126] They attributed the increase of roughness to flow instability during drying of spin-cast perfluorinated polymer films, which tends to cause high surface roughness and the formation of "pinholes".

To determine the maximum extractable energy density (U_{max}^{CD}) under pulsed conditions of CYTOP/CNETMS bilayer films, charge-discharge (C-D) measurements were performed. As shown in Figure 5.14a, the single layer, 3.5 μm thick CNETMS film gave a U_{max}^{CD} of ~ 4 J/cm^3, whereas the corresponding CYTOP/CNETMS bilayer films showed significantly larger U_{max}^{CD} values in the range of ~ 7 to 8.5 J/cm^3, for CYTOP thickness ranging from 20 to 176 nm. The U_{max}^{CD} for the 1.3 μm thick CNETMS was determined to be ~7.5 J/cm^3 (shown in Figure 5.14b), which is higher than for the thicker CNETMS film as a result of the higher E_B for the thinner film. However, the increase in energy density is substantially lower than that of a linear dielectric response, which we will address below. In the bilayer films with 1.3 μm thick CNETMS, the maximum extractable energy density reaches values of ~ 9.5 J/cm^3. It is interesting to note that for the thicker CNETMS film, increasing the CYTOP thickness leads to an increase of the energy density, whereas for the thinner CNETMS film the trend of the energy density decreases with increasing CYTOP thickness.

In addition to extractable energy density, C-D measurements can also determine the E_B of CYTOP/CNETMS bilayer films by taking the maximum electric field associated with the maximum energy density for each set of devices. In Figure 5.14a, the E_B of CYTOP/CNETMS bilayer films (total 3.5 μm thick) acquired from C-D qualitatively presents the increase of E_B as the thickness of CYTOP increases. Although the E_B acquired by this method is lower than that from breakdown testing (shown in Figure 5.13), the trend of increasing E_B as CYTOP thickness increases is consistent. The solid lines in Figure 5.14a correspond to a quadratic fit to the experimentally measured data shown in solid circles (average value and error bar are shown when two or three devices were measured at the same electric field). Although there are some deviations, the fit qualitatively presents the quadratic increase of the extractable energy density as electric field increases.

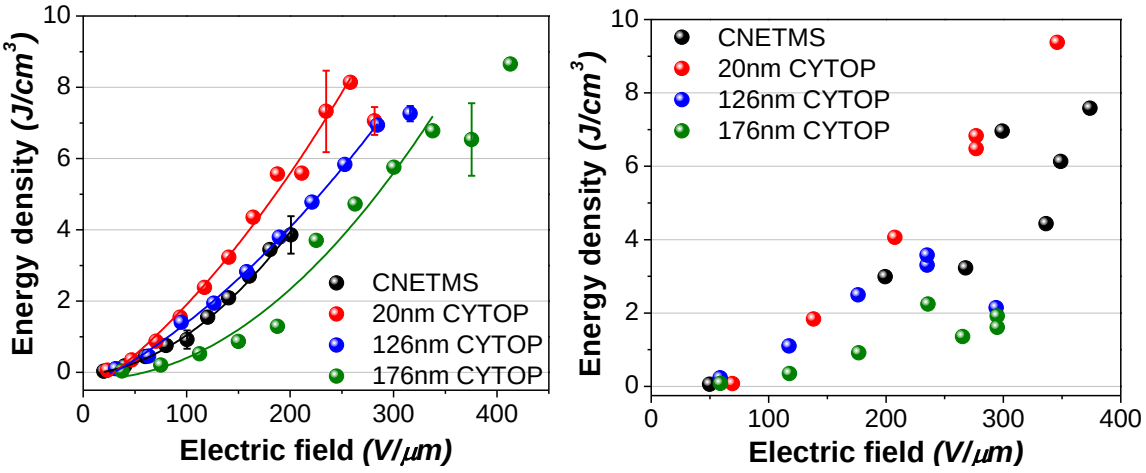

Figure 5.14 U_{max}^{CD} of CYTOP/CNETMS bilayer films (a) with 3.5 μm thick CNETMS and (b) with 1.3 μm thick CNETMS films. The error bars were obtained from measurements of 2-5 devices at the given electric field strength whereas the data points without an error bar were obtained from a single measurement at the applied electric field.

Figure 5.15 shows the representative P-E hysteresis loops of CYTOP/CNETMS bilayer films with 1.3 μm thick CNETMS with 20 and 176 nm CYTOP layers. Unlike linear dielectric-like response of neat CNETMS films (see Figure 4.18), CYTOP/CNETMS bilayer films depart from linear dielectric response in low electric field (below 200 V/μm) and shows pronounced rounding of P-E loops with increased remnant polarization. This tendency is more significant when the thickness of CYTOP layer increases from 20 nm to 176 nm. Particularly, for the bilayer with 176 nm CYTOP, a transition from linear to lossy dielectric seems to exist at the field strength of ~250 V/μm. We attribute the increased hysteresis in P-E loops and so-called linear-lossy transition of CYTOP/CNETMS bilayer to trapped charges in CYTOP layer.[127] In particular, trapped charges in CYTOP layer easily contribute to conduction behavior in P-E loops (round shape) and eventually result in loss. The more rounded shape and fatter loops of CYTOP/CNETMS bilayer with 176 nm CYTOP indicates the increased loss qualitatively.

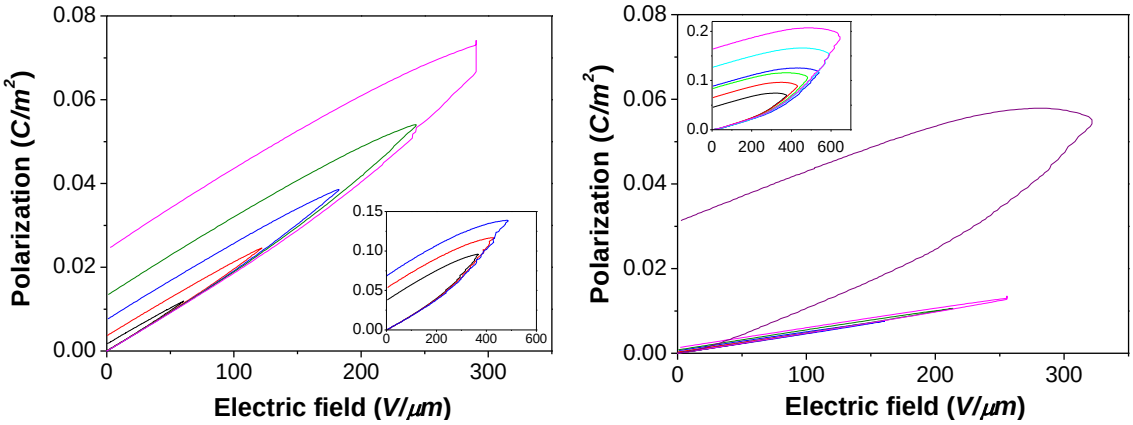

Figure 5.15 P-E hysteresis loops of CYTOP/CNETMS bilayer films with (left) 20 nm and (right) 176 nm CYTOP layer. 1.3 μm thick CNETMS (field strength above ~300 V/μm is shown in inset).

Figure 5.16 sums up U_{max}^{PE} and energy extraction efficiency of CYTOP/CNETMS bilayer films for 1.3 μm thick CNETMS. Due to the increased loss associated with charge trapping possibly arising from CYTOP layer, which is reflected in pronounced widening of hysteresis loops, CYTOP/CNETMS bilayer films could not outperform neat CNETMS films in terms of energy storage density. Thicker CYTOP layer substantially decreases the extraction efficiency of CYTOP/CNETMS bilayer films, leading to poor U_{max}^{PE}.

On the contrary, the improvement of energy storage performance by CYTOP layer does not hold for CYTOP/CNETMS bilayer films with 1.3 μm thick CNETMS. We are not certain for the reason of this difference, but it might be due to the field concentration in CYTOP layer, which is much larger in bilayer film with 1.3 μm thick CNETMS than 3.5 μm thick CNEMTS because of field partitioning.

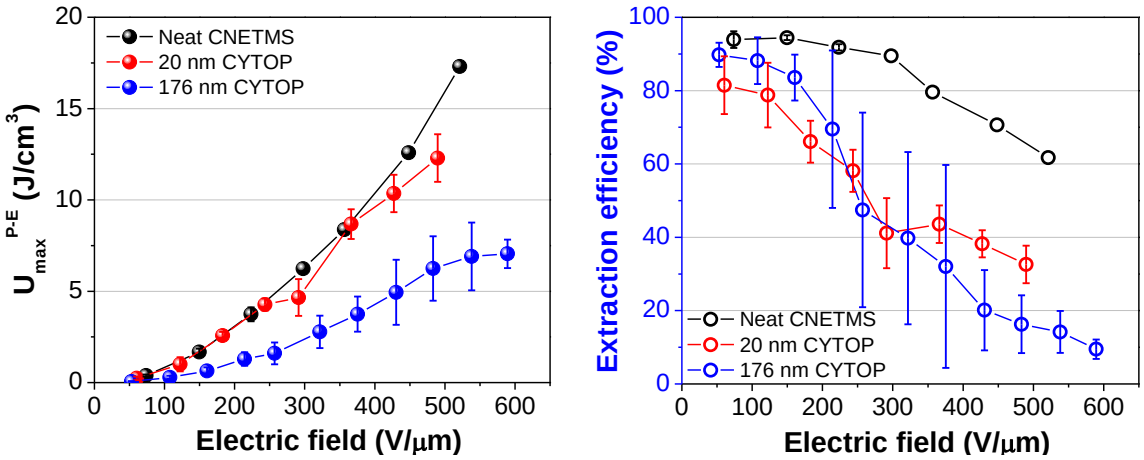

Figure 5.16 (left) U_{max}^{PE} and (left) the energy extraction efficiency of CYTOP/CNETMS bilayer films up to 176 nm of CYTOP layer (1.3 μm thick CNETMS).

Table 5.4 summarizes U_{max}^{CD}, U_{max}^{PE}, and energy extraction efficiency of CYTOP/CNETMS bilayer films. For CYTOP/CNETMS bilayer films with 3.5 μm thick CNETMS exhibit increased energy densities and efficiency compared to neat CNETMS films. This improvement can be correlated with the increase of E_B, which is shown in Figure 5.13, which is ascribed to the trapping and scattering of injected charge carriers in CYTOP barrier layer. It is important to note that the improvement of energy storage performance of bilayer films gradually decreases with thicker CYTOP layer, which might be due to the transition of dielectric response of CYTOP from linear to lossy dielectrics because of too many trapped charges.

Table 5.4 The summary of U_{max}^{CD}, U_{max}^{PE}, and energy extraction efficiency of CYTOP/CNETMS bilayer films. Extraction efficiency is determined at the field strength of 300 V/μm.

	CNETMS thickness (μm)	Neat CNETMS	20nm CYTOP	126nm CYTOP	176nm CYTOP
U_{max}^{CD}(J/cm^3)	1.3	7.0	9.4	3.6	2.3
U_{max}^{PE}(J/cm^3)		17.3	13.8	n/a	9.1
Extraction efficiency (at 300 V/μm)		89%	48%	n/a	27%
U_{max}^{CD}(J/cm^3)	3.5	4.2	8.1	7.5	8.7
U_{max}^{PE}(J/cm^3)		4.2	8.9	n/a	5.2
Extraction efficiency (at 300 V/μm)		41%	50%	n/a	30%

5.4.2 PPO/CNETMS bilayer films

Poly(*p*-phenylene oxide), PPO, was selected for a barrier layer because of its low loss tangent[128] and linear dielectric response at electric field above 600 V/μm[83] unlike CYTOP, which becomes lossy when fields go above 300 V/μm. PPO also has slightly higher permittivity than that of CYTOP (2.8 vs 2.0). Additionally, it can readily be coated on top of CNETMS sol-gel films by typical spin casting method.

In this section, PPO barrier layer with varying thickness is coated on top of CNETMS

sol-gel films, and its impact on dielectric, electrical, and energy storage properties is investigated. As discussed in the Section 5.1, the width of potential barrier can become larger with thicker PPO barrier layer, lowering the probability of carrier transmission through the potential barrier. PPO layer would provide a good comparison to CYTOP in terms of the effect of the permittivity of barrier layer on the energy potential profile between the interface of metal electrode and dielectric, as shown in Equation 5.1 and Figure 5.2.

As PPO layer goes thicker, the $\varepsilon_r$of bilayer films decreases because of low ε_r of PPO compared to neat CNETMS. Figure 5.17a shows the gradual decrease in ε_r of PPO/CNETMS bilayer films with thicker PPO, leading to ~16 of ε_r with 100 nm of PPO layer. Despite of decreased ε_r, it is still higher than PVDF-based copolymers, whose ε_r remains around ~10.[2] Leakage current profile of dielectric films at moderate electric field would provide physical representation inside dielectric materials, *i.e.*, how many intrinsic charge carriers are present? Are there enough number of channels for the migration of charge carriers? PPO/CNETMS bilayer films show the reduction of leakage current on the order of magnitude, from 10^{-6} to 10^{-7} J/cm^3, shown in Figure 5.17b. Although the maximum field strength of leakage current measurement was ± 80 V/μm, the reduction of current density still suggests the mitigation of charge carrier conduction inside bilayer films *via* the inclusion of PPO barrier layer.

To investigate the effect of PPO inclusion on the polarization response on bilayer films, P-E measurements were performed. Figure 5.18 sums up P-E hysteresis loops of bilayer films along with conduction current profile extracted from P-E loops. For better comparison, P-E loops and conduction current profile of the same bilayer films are placed side by side. Please note that neat CNETMS films shown in this section underwent the same thermal treatment to PPO/CNETMS bilayer films, so they were baked additionally for three hours at 120ºC after normal baking.

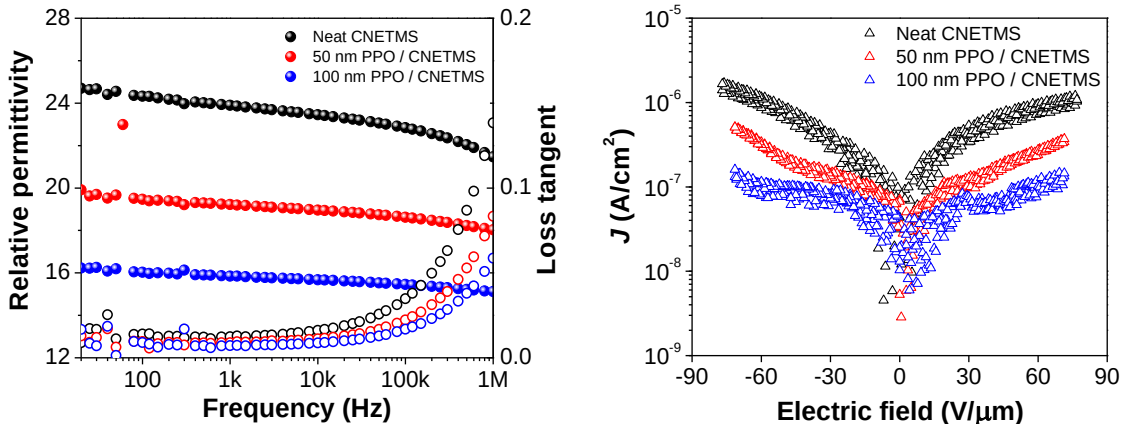

Figure 5.17 (a) Field dependent permittivity and loss tangent and (b) leakage current profiles of PPO/CNETMS bilayer films. Thickness of PPO top layer varies from 0 to 100 nm.

It can be seen that the hysteresis loops at fields below 300 V/μm become slimmer than neat CNEMTS with thicker PPO barrier layer. However, when it comes to high field range, which is shown in inset of polarization plot, the widening of hysteresis loops becomes apparent when the thickness of PPO grows. This tendency can be more accurately analyzed in conduction current profile since conduction current arises only from the contribution of electrical conduction component, separating the contribution of displacement current. At the electric field range below 300 V/μm, neat CNETMS films exhibit conduction current profile with oscillatory behavior, probability arising from trapping and detrapping of charge carriers by the applied electric field.[9, 114] As the electric field grows above 300 V/μm, the magnitude of conduction current saturates at ~10^{-4} J/cm^3, indicating the channel-limited conduction mechanism just before dielectric breakdown. For PPO/CNETMS bilayer films containing 50 and 100 nm PPO layers, the profile below 300 V/μm shows significant reduction in conduction current. Moreover, the threshold for the appearance of conduction current moves toward higher electric field when PPO becomes thicker, delaying the onset of electrical conduction of PPO/CNETMS bilayer films. It is important to note that the saturation point of current density is

increased by the order of magnitude in PPO/CNETMS bilayer films than neat CNETMS, indicating increased number of channels for electrical conduction at high fields.

On the contrary, in PPO/CNETMS bilayer films with PPO layers of 150 and 200 nm, the conduction current reappears at field range below 300 V/μm and current density at saturation point increases. Indeed, the conduction currents of bilayer films with 200 nm PPO are so much more prominent than other bilayer films and neat CNETMS, PPO layer itself seems to become lossy at this point.

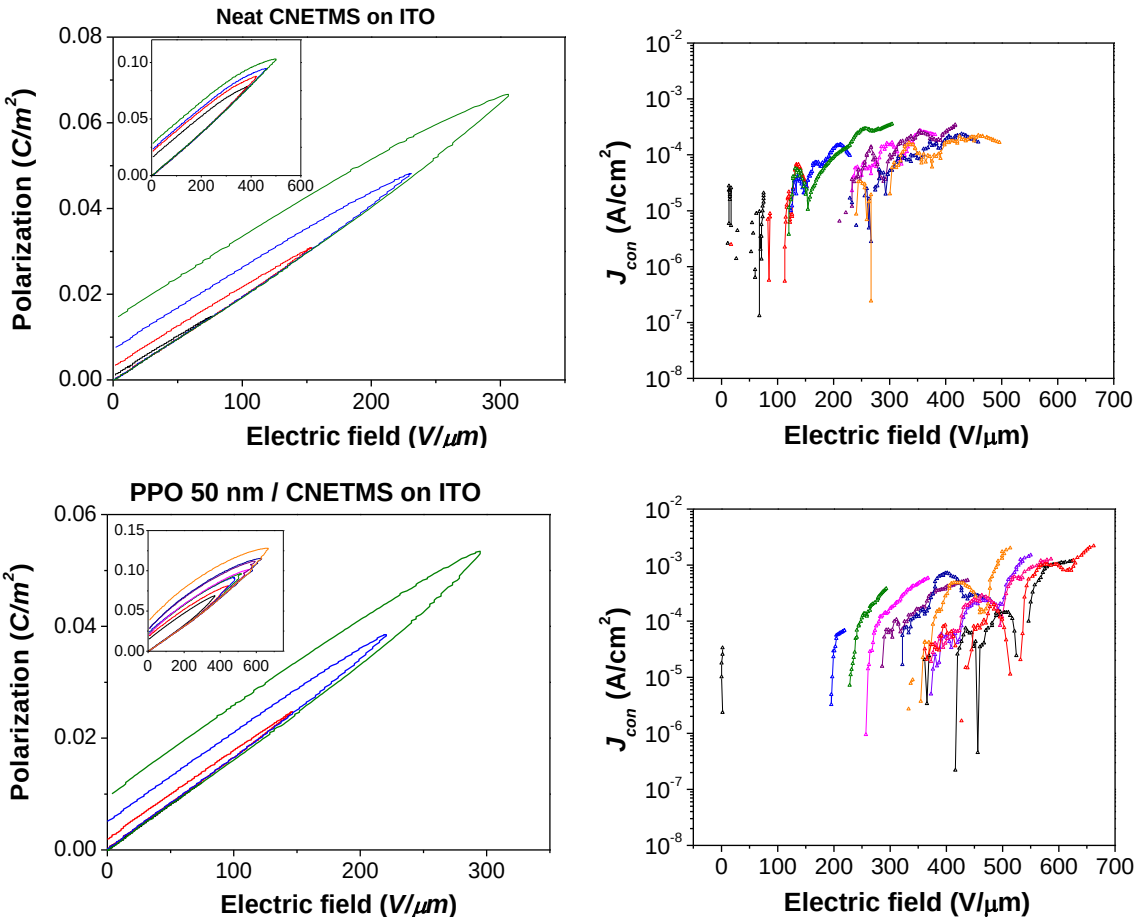

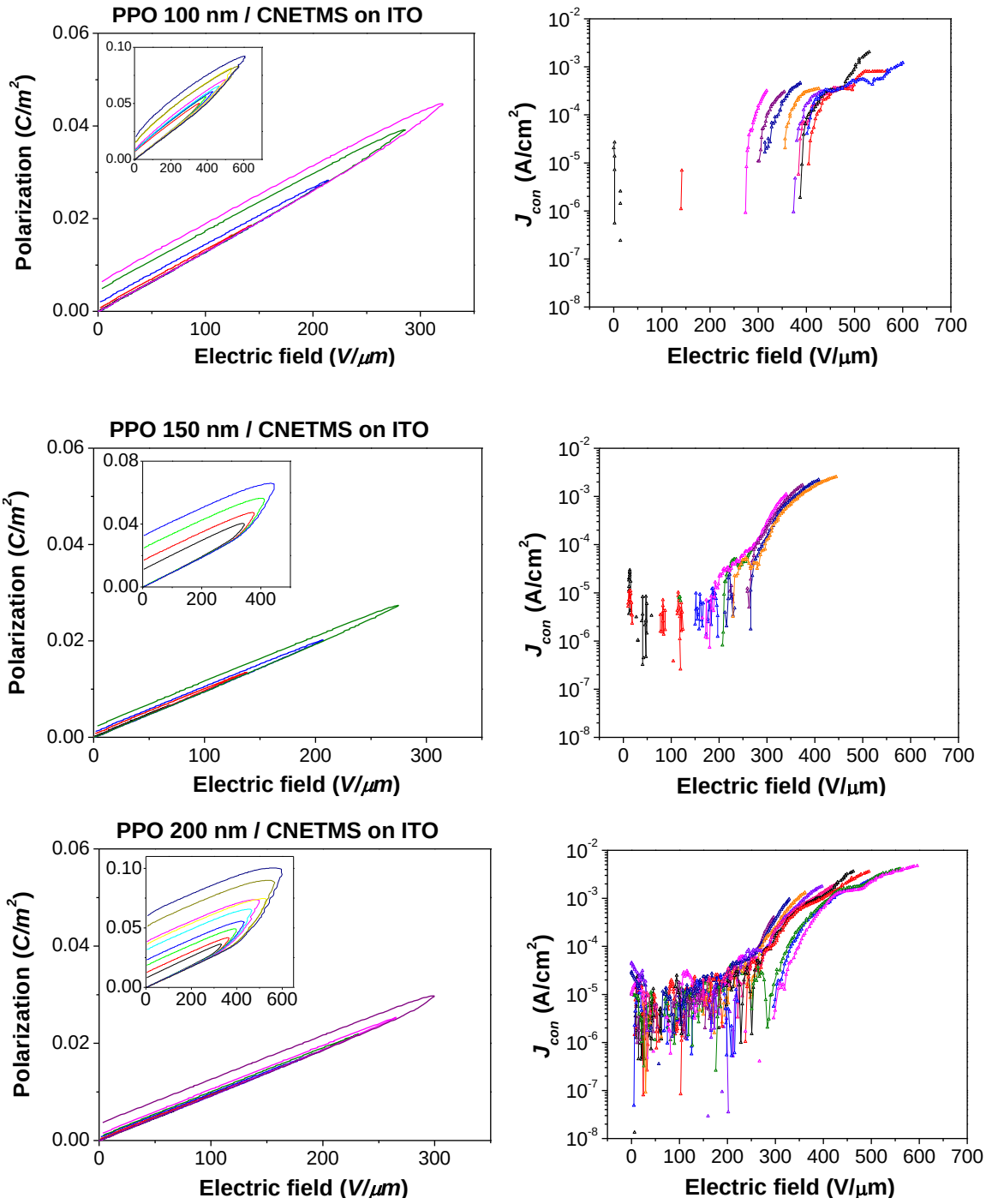

Figure 5.18 (left) P-E loops and (right) conduction current profile of PPO/CNETMS bilayer films. From top to bottom: 50, 100, 150, 200 nm PPO layer on top of CNETMS films.

With the aid of PPO barrier layer, energy storage performance of PPO/CNETMS bilayer

films is enhanced substantially. As shown in Figure 5.19, bilayer films containing 50 and 100 nm PPO layers displays increase in E_B, U_{max}^{PE}, U_{max}^{CD}, and extraction efficiency for compared to neat CNETMS. The increase in U_{max}^{PE} and E_B is more than 25%, probably due to trapping of charge carriers and decreased probability of carrier transmission *via* the PPO barrier layer. For the bilayer film with 50 nm PPO, U_{max}^{PE} and U_{max}^{CD} reach 20 and 30 J/cm^3, respectively. The difference of maximum energy density from each method is ascribed to the difference in charging time, during which C-D method used a few hundred milliseconds instead of 10 ms for P-E method. Typically, electrical conduction in sol-gel films is promoted when the device is under charging state for a longer time, causing increased probability of partial discharge, premature breakdown events, and eventually lowered energy storage capability. This applies also to the energy density of neat CNETMS films from both P-E and C-D methods, which marks 16 J/cm^3 and 8 J/cm^3, respectively. It is important to note that all PPO/CNETMS bilayer films perform well in C-D method, showing $U_{max}^{CD}$of 30 J/cm^3 with 50 nm PPO and comparable U_{max}^{CD} for 150 and 200 nm PPO bilayer films compared to neat CNETMS. The fact that these bilayer films with 150 and 200 nm PPO layer underperformed in P-E method indicates the effectiveness of PPO barrier layer in mitigating electrical conduction in bilayer sol-gel films.

Energy extraction efficiencies of bilayer films are presented in Figure 5.20. By adding 50 and 100 nm PPO layer, the extraction efficiency of bilayer films is enhanced marginally. The increase of efficiency is larger in 100 nm PPO than 50 nm PPO, which pairs with the most delayed onset of conduction shown in Figure 5.19. However, for PPO layers of 150 and 200 nm, the extraction efficiency drops below that of neat CNETMS films as the field strength goes above ~300 V/μm. We are not certain the origin of such transition, *i.e.*, linear to lossy dielectric transition of PPO/CNETMS bilayer films, it may be due to the trapped charges in PPO layer itself, as discussed in CYTOP/CNETMS bilayer films.

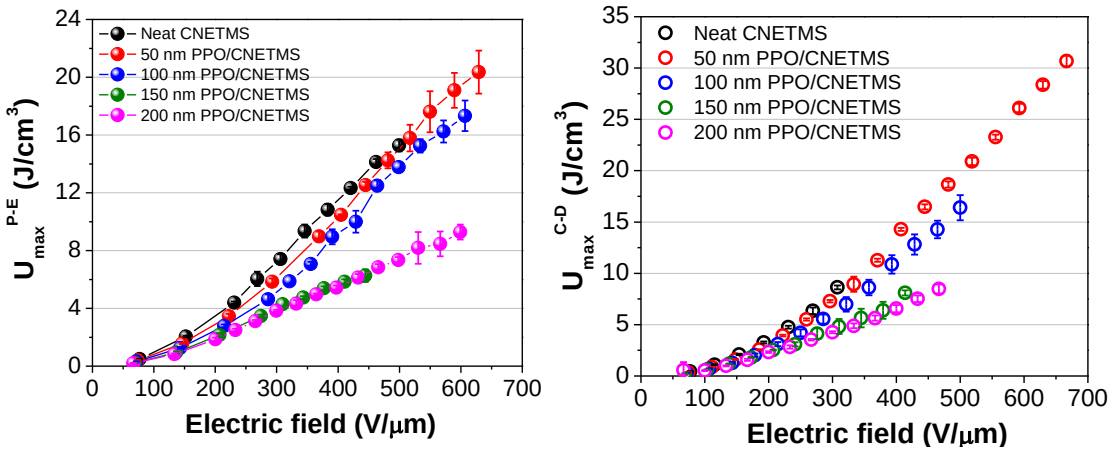

Figure 5.19 (left) U_{max}^{PE} and (right) $U_{max}^{CD}$of PPO/CNETMS bilayer films with PPO thickness from 0 nm (neat CNETMS) to 200 nm.

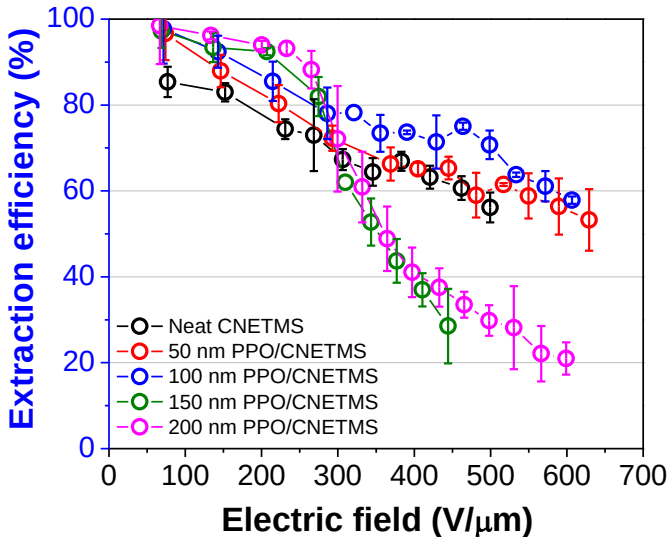

Figure 5.20 The energy extraction efficiency of PPO/CNETMS bilayer films with PPO thickness from 0 nm (neat CNETMS) to 200 nm.

5.4.3 Alkylphosphonic acid monolayer/CNETMS bilayer films

The self-assembled monolayers of alkylphosphonic acid on top of CNETMS sol-gel films were immediately prepared by immersing CNETMS sol-gel films into the solution of 0.1 mM of alkylphosphonic acid in ethanol at 70 ºC for 19 hours. After the 19 hours of

treatment in ethanol, bilayer films were rinsed by ultrasonication in absolute ethanol for ten minutes, blown dry with nitrogen, and kept in desiccator. The thicknesses of alkylphosphonic acid monolayers were determined by ellipsometry with averaging multiple measurements in different spots.

The total three of phosphonic acids (PAs) varying the length of alkyl spacer were tested for the barrier layer on CNETMS sol-gel films: propylphosphonic acid (PPA), octylphosphonic acid (OPA), and octadecylphosphonic acid (ODPA). As summarized in Figure 5.21a, the energy extraction efficiencies of PA/CNETMS bilayer films are greatly enhanced in all ranges of electric field compared to neat CNETMS. Increased extraction efficiency of PA/CNETMS bilayer films results in the enhancements in both breakdown strength and $U_{max}^{PE}$with the exception of the ODPA/CNETMS bilayer film. In particular, OPA/CNETMS bilayer films exhibit U_{max}^{PE} of 40 J/cm^3 at the field strength of 850 V/μm.

The increased extraction efficiency is readily observed in P-E loops, which is shown in Figure 5.21b for OPA/CNETMS bilayer films. P-E loops of OPA/CNETMS bilayer films maintain linear-like dielectric response up to ~600 V/μm with more than 85% of extraction efficiency. It is worthwhile to note that the onset of dielectric saturation in OPA/CNETMS bilayer films is observed at fields above ~600 V/μm, which was not seen in neat CNETMS films due to the electrical conduction at high fields. It is believed that the presence of self-assembled phosphonic acid monolayer effectively mitigates charge carrier injection and associated electrical conduction, so that the dielectric saturation in CNETMS sol-gel films is now able to be observed.

The improvements in energy extraction efficiency and U_{max}^{PE} of PA/CNETMS bilayer films are attributed to densely packed monolayer that effectively suppresses carrier tunneling *via* highly ordered aliphatic chains.[129, 130] It is interesting to note that the effectiveness of PA barrier layer is maximized with OPA/CNEMTS and decreased when

ODPA is utilized, which is reflected in lower breakdown strength and U_{max}^{PE} of ODPA/CNETMS bilayer films in Figure 5.21a. Since the thicknesses of OPA and ODPA layers are 0.3 and 2.2 nm respectively, we believe that ODPA barrier layer may not have densely packed monolayer or lower coverage on the surface of CNETMS sol-gel film as compared to PPA and OPA barrier layers. Further research is aimed at the optimization of phosphonic acid monolayer in the length of alkyl chain and packing density by means of thermal annealing.

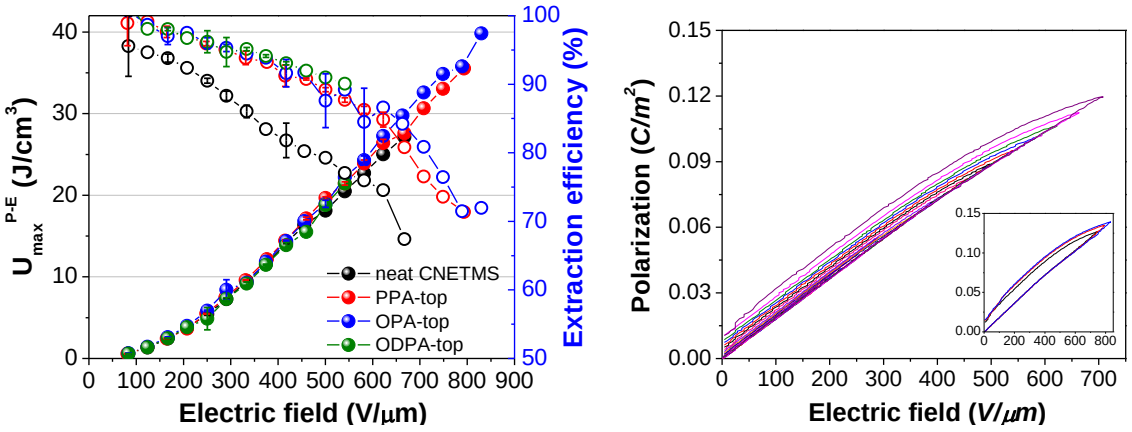

(a) (b)

Figure 5.21 (a) U_{max}^{PE} and energy extraction efficiency of PA/CNETMS bilayer films. (b) P-E loops of OPA/CNETMS bilayer films.

5.5 Conclusions

In this chapter, the effect of tunneling barrier layer on dielectric and energy storage properties of dielectric films based on 2-cyanoethyltrimethoxysilane sol-gel precursor was investigated. A potential energy barrier layer naturally emerges in metal-insulator-metal (MIM) system arising from the alignment of Fermi energy levels at the interface of metal electrode and insulating film. Such a potential barrier prohibits the flow of charge carriers *via* either field-induced thermionic emission or field emission (or cold emission) from electrodes to insulating film.

As discussed in Chapter 4, the electrical conduction in CNETMS sol-gel films at fields above 300 V/μm substantially deteriorates the energy storage performance of the capacitor devices from the sol-gel films. Since there are not many intrinsic carriers in the dielectric sol-gel films, the primary reason for electrical conduction is ascribed to injected charge carriers from metal electrodes at high electric fields. The introduction of inorganic or organic tunneling barrier layer between metal electrode and dielectric sol-gel film is expected to lower the probability of charge carrier transmission and to increase trapping of charge carriers, thereby mitigating electrical conduction in CNETMS sol-gel films.

Among inorganic and organic barrier layers investigated for this purpose, atomic layer deposition (ALD)-processed ZrO_2, spin-coated poly(*p*-phenylene oxide), and self-assembled phosphonic acid monolayers are found to be effective in increasing breakdown strength, failure reliability, energy storage density and extraction efficiency of CNETMS sol-gel films. In particular, OPA/CNETMS bilayer films exhibit U_{max}^{PE} of 40 J/cm^3 at 850 V/μm, which is attributed to densely packed monolayer that effectively suppresses carrier tunneling and associated electrical conduction. To the best of our knowledge, this is the largest energy density achieved in dielectric film capacitor for pulsed power applications.

CHAPTER 6

CONCLUSIONS AND OUTLOOK

The development of dielectric materials for electrical energy storage applications requires multidisciplinary research efforts including materials science, polymer physics, organic and inorganic chemistry, electrical engineering, device physics, etc. Many interesting results have been put forward for this topic, which involves high permittivity ferroelectric polymers, ceramic/polymer nanocomposites, relaxor ferroelectric polymers, and polar hybrid sol-gel materials. Recently, more work has taken a close look at the morphology of dielectric materials and the improvement of energy extraction efficiency *via* the control of material morphology. It is my belief that the research for optimizing the morphology of dielectric materials to enhance the efficiency of energy extraction will intrigue more interests.

Two classes of dielectric materials were investigated in this thesis. In ceramic/polymer nanocomposite materials, thin film processing was improved to achieve more uniform morphology at the material level, leading to higher breakdown strength and energy density. In silica-based sol-gel materials bearing dipolar side groups, linear dielectric-like response arising from suppressed cooperative motion of polar domains has been found to be beneficial for decreasing loss in energy extraction process, resulting in high energy storage capability with moderate permittivity.

Moreover, the formation of self-assembled phosphonic acid monolayer on the sol-gel hybrid films based on 2-cyanoethyltrimethoxysilane (CNETMS) precursor is shown to be successful in mitigating carrier injection and associated electrical conduction. Particularly, CNETMS sol-gel films with octylphosphonic acid monolayer as a barrier layer exhibit 40 J/cm3 of extractable energy density, which is the largest energy density obtained in dielectric film capacitors for pulsed power applications.

However, much remains to be explored. For example, compared to normal ferroelectric polymers, much less is known about the potential of relaxor ferroelectric polymers and their composite systems. Polar hybrid sol-gel material is the least investigated class of materials for pulsed power applications. There must be ways to increase permittivity of sol-gel material without compromising the extraction efficiency (for example, by tuning crosslinking density and incorporating highly polarizable molecules into sol-gel matrix *via* physical or chemical entrapment). Surface engineering of the interface between metal electrode and insulating film will be another big topic for this field as a way to control charge transport through the interface to optimize energy storage performance of dielectric materials. Future work will undoubtedly tackle these technical challenges and, with some luck, provide novel dielectric materials with practically useful and valuable properties.

REFERENCES

1. Nalwa, H. S. *Ferroelectric polymers: chemistry, physics, and applications*. CRC Press: 1995.
2. Lovinger, A. J. Ferroelectric polymers. *Science* **1983**, *220*, 1115-1121.
3. Von Hippel, A. R. *Dielectrics and waves*. John Wiley & Sons, New York: Boston; London, 1954.
4. Kao, K. C. *Dielectric Phenomena in Solids*. Academic Press: 2004; p 602.
5. Jonscher, A. K. Dielectric relaxation in solids. *J. Phys. D: Appl. Phys.* **1999**, *32*, R57-R70.
6. Tanuma, S.; Powell, C. J.; Penn, D. R. Calculations of electron inelastic mean free paths. V. Data for 14 organic compounds over the 50-2000 eV range. *Surf. Interface Anal.* **1994**, *21*, 165-176.
7. O'Dwyer, J. J. *The theory of electrical conduction and breakdown in solid dielectrics*. Clarendon Press: Oxford, 1973; p 317.
8. Dissado, L. A. *Electrical degradation and breakdown in polymers*. P. Peregrinus: London, 1992; p 601.
9. Kao, K. C. New theory of electrical discharge and breakdown in low-mobility condensed insulators. *J. Appl. Phys.* **1984**, *55*, 752-755.
10. Goodenough, J. B.; Abruna, H. D.; Buchanan, M. V. *Basic Research Needs for Electrical Energy Storage. Report of the Basic Energy Sciences Workshop on Electrical Energy Storage*; U.S. Department of Energy (DOE) Office of Science (SC): 2007.
11. Kötz, R.; Carlen, M. Principles and applications of electrochemical capacitors. *Electrochim. Acta* **2000**, *45*, 2483-2498.
12. Rabuffi, M.; Picci, G. Status quo and future prospects for metallized polypropylene energy storage capacitors. *IEEE Trans. Plasma Sci.* **2002**, *30*, 1939-1942.
13. Yao, K.; Chen, S.; Rahimabady, M.; Mirshekarloo, M. S.; Yu, S.; Tay, F. E. H.; Sritharan, T.; Lu, L. Nonlinear dielectric thin films for high-power electric storage with energy density comparable with electrochemical supercapacitors. *IEEE Trans. Ultrason., Ferroelect., Freq. Contr.* **2011**, *58*, 1968-1974.

14. Kawai, H. The piezoelectricity of poly (vinylidene fluoride). *Jpn. J. Appl. Phys.* **1969**, *8*, 975-976.

15. Bergman, J. G. Pyroelectricity and optical second harmonic generation in polyvinylidene fluoride films. *Appl. Phys. Lett.* **1971**, *18*.

16. Zhang, Q. M.; Bharti, V.; Zhao, X. Giant electrostriction and relaxor ferroelectric behavior in electron-irradiated poly(vinylidene fluoride-trifluoroethylene) copolymer. *Science* **1998**, *280*, 2101-2104.

17. Chu, B.; Zhou, X.; Ren, K.; Neese, B.; Lin, M.; Wang, Q.; Bauer, F.; Zhang, Q. M. A dielectric polymer with high electric energy density and fast discharge speed. *Science* **2006**, *313*, 334-336.

18. Zhu, L.; Wang, Q. Novel ferroelectric polymers for high energy density and low loss dielectrics. *Macromolecules* **2012**, *45*, 2937-2954.

19. Yang, L.; Li, X.; Allahyarov, E.; Taylor, P. L.; Zhang, Q. M.; Zhu, L. Novel polymer ferroelectric behavior via crystal isomorphism and the nanoconfinement effect. *Polymer* **2013**, *54*, 1709-1728.

20. Guan, F.; Pan, J.; Wang, J.; Wang, Q.; Zhu, L. Crystal orientation effect on electric energy storage in poly(vinylidene fluoride-co-hexafluoropropylene) copolymers. *Macromolecules* **2010**, *43*, 384-392.

21. Guan, F.; Wang, J.; Pan, J.; Wang, Q.; Zhu, L. Effects of polymorphism and crystallite size on dipole reorientation in poly(vinylidene fluoride) and its random copolymers. *Macromolecules* **2010**, *43*, 6739-6748.

22. Guan, F.; Wang, J.; Zhu, L.; Pan, J.; Wang, Q. Effects of film processing conditions on electric energy storage for pulsed power applications. *IEEE Trans. Dielectr. Electr. Insul.* **2011**, *18*, 1293-1300.

23. Khanchaitit, P.; Han, K.; Gadinski, M. R.; Li, Q.; Wang, Q. Ferroelectric polymer networks with high energy density and improved discharged efficiency for dielectric energy storage. *Nat. Commun.* **2013**, *4*.

24. Yuan, X.; Chung, T. C. M. Cross-linking effect on dielectric properties of polypropylene thin films and applications in electric energy storage. *Appl. Phys. Lett.* **2011**, *98*, 062901-062901.

25. Lu, Y.; Claude, J.; Neese, B.; Zhang, Q.; Wang, Q. A Modular Approach to Ferroelectric Polymers with Chemically Tunable Curie Temperatures and Dielectric Constants. *J. Am. Chem. Soc.* **2006**, *128*, 8120-8121.

26. Guan, F.; Yang, L.; Wang, J.; Guan, B.; Han, K.; Wang, Q.; Zhu, L. Confined ferroelectric properties in poly(vinylidene fluoride-co-chlorotrifluoroethylene)-graft-polystyrene graft copolymers for electric energy storage applications. *Adv. Funct. Mater.* **2011**, *21*, 3176-3188.

27. Li, J.; Tan, S.; Ding, S.; Li, H.; Yang, L.; Zhang, Z. High-field antiferroelectric behaviour and minimized energy loss in poly(vinylidene-co-trifluoroethylene)-graft-poly(ethyl methacrylate) for energy storage application. *J. Mater. Chem.* **2012**, *22*, 23468.

28. Rahimabady, M.; Chen, S.; Yao, K.; Eng Hock Tay, F.; Lu, L. High electric breakdown strength and energy density in vinylidene fluoride oligomer/poly(vinylidene fluoride) blend thin films. *Appl. Phys. Lett.* **2011**, *99*, 142901-142901-3..

29. Rahimabady, M.; Yao, K.; Arabnejad, S.; Lu, L.; Shim, V. P. W.; Cheong Wun Chet, D. Intermolecular interactions and high dielectric energy storage density in poly(vinylidene fluoride-hexafluoropropylene)/poly(vinylidene fluoride) blend thin films. *Appl. Phys. Lett.* **2012**, *100*, 252907-252907-4.

30. Wu, S.; Lin, M.; Lu, S. G.; Zhu, L.; Zhang, Q. M. Polar-fluoropolymer blends with tailored nanostructures for high energy density low loss capacitor applications. *Appl. Phys. Lett.* **2011**, *99*, 132901-132901.

31. Wolak, M. A.; Pan, M.-J.; Wan, A.; Shirk, J. S.; Mackey, M.; Hiltner, A.; Baer, E.; Flandin, L. Dielectric response of structured multilayered polymer films fabricated by forced assembly. *Appl. Phys. Lett.* **2008**, *92*, 113301-113301.

32. Mackey, M.; Hiltner, A.; Baer, E.; Flandin, L.; Wolak, M. A.; Shirk, J. S. Enhanced breakdown strength of multilayered films fabricated by forced assembly microlayer coextrusion. *J. Phys. D: Appl. Phys.* **2009**, *42*, 175304-175304.

33. Wolak, M. A.; Wan, A. S.; Shirk, J. S.; Mackey, M.; Hiltner, A.; Baer, E. Imaging the effect of dielectric breakdown in a multilayered polymer film. *J. Appl. Polym. Sci.* **2011**, *123*, 2548-2557

34. Mackey, M.; Schuele, D. E.; Zhu, L.; Flandin, L.; Wolak, M. A.; Shirk, J. S.; Hiltner, A.; Baer, E. Reduction of dielectric hysteresis in multilayered films via nanoconfinement. *Macromolecules* **2012**, *45*, 1954-1962.

35. Zhou, Z.; Mackey, M.; Carr, J.; Zhu, L.; Flandin, L.; Baer, E. Multilayered polycarbonate/poly(vinylidene fluoride-co-hexafluoropropylene) for high energy density capacitors with enhanced lifetime. *J. Polym. Sci., Part B: Polym. Phys.* **2012**, *50*, 993-1003.

36. Carr, J. M.; Mackey, M.; Flandin, L.; Schuele, D.; Zhu, L.; Baer, E. Effect of biaxial orientation on dielectric and breakdown properties of poly(ethylene terephthalate)/poly(vinylidene fluoride-co-tetrafluoroethylene) multilayer films. *J. Polym. Sci., Part B: Polym. Phys.* **2013**, *51*, 882-896.

37. Zhou, Z.; Carr, J.; Mackey, M.; Yin, K.; Schuele, D.; Zhu, L.; Baer, E. Interphase/interface modification on the dielectric properties of polycarbonate/poly(vinylidene fluoride-co-hexafluoropropylene) multilayer films for high-energy density capacitors. *J. Polym. Sci., Part B: Polym. Phys.* **2013**, *51*, 978-991.

38. Burlingame, Q.; Wu, S.; Lin, M.; Zhang, Q. M. Conduction mechanisms and structure–property relationships in high energy density aromatic polythiourea dielectric films. *Adv. Energy Mater.* **2013**, *3*, 1051-1055.

39. Wu, S.; Li, W.; Lin, M.; Burlingame, Q.; Chen, Q.; Payzant, A.; Xiao, K.; Zhang, Q. M. Aromatic polythiourea dielectrics with ultrahigh breakdown field strength, low dielectric loss, and high electric energy density. *Adv. Mater.* **2013**, *25*, 1734-1738.

40. Gupta, A. K.; Chand, N. Glass transition in polyacrylonitrile: Analysis of dielectric relaxation data. *Journal of Polymer Science: Polymer Physics Edition* **1980**, *18*, 1125-1136.

41. Poulsen, M.; Ducharme, S. Why ferroelectric polyvinylidene fluoride is special. *IEEE Trans. Dielectr. Electr. Insul.* **2010**, *17*, 1028-1035.

42. Tasaka, S.; Nakamura, T.; Inagaki, N. Ferroelectric behavior in copolymers of acrylonitrile and allylcyanide. *Jpn. J. Appl. Phys.* **1992**, *31*, 2492-2494.

43. Dang, Z.-M.; Yuan, J.-K.; Yao, S.-H.; Liao, R.-J. Flexible nanodielectric materials with high permittivity for power energy storage. *Adv. Mater.* **2013**, *25*, 6334-6365.

44. Barber, P.; Balasubramanian, S.; Anguchamy, Y.; Gong, S.; Wibowo, A.; Gao, H.; Ploehn, H. J.; zur Loye, H.-C. Polymer composite and nanocomposite dielectric materials for pulse power energy storage. *Materials* **2009**, *2*, 1697-1733.

45. Wang, Q.; Zhu, L. Polymer nanocomposites for electrical energy storage. *J. Polym. Sci., Part B: Polym. Phys.* **2011**, *49*, 1421-1429.

46. Dang, Z.-M.; Yuan, J.-K.; Zha, J.-W.; Zhou, T.; Li, S.-T.; Hu, G.-H. Fundamentals, processes and applications of high-permittivity polymer–matrix composites. *Prog. Mater Sci.* **2012**, *57*, 660-723.

47. Kim, P.; Jones, S. C.; Hotchkiss, P. J.; Haddock, J. N.; Kippelen, B.; Marder, S. R.; Perry, J. W. Phosphonic acid-modified barium titanate polymer nanocomposites with high permittivity and dielectric strength. *Adv. Mater.* **2007**, *19*, 1001-1005.

48. Kim, P.; Doss, N. M.; Tillotson, J. P.; Hotchkiss, P. J.; Pan, M.-J.; Marder, S. R.; Li, J.; Calame, J. P.; Perry, J. W. High energy density nanocomposites based on surface-modified batio3 and a ferroelectric polymer. *ACS Nano* **2009**, *3*, 2581-2592.

49. Li, J.; Claude, J.; Norena-Franco, L. E.; Seok, S. I.; Wang, Q. Electrical energy storage in ferroelectric polymer nanocomposites containing surface-functionalized batio3 nanoparticles. *Chem. Mater.* **2008**, *20*, 6304-6306.

50. Li, J.; Seok, S. I.; Chu, B.; Dogan, F.; Zhang, Q.; Wang, Q. Nanocomposites of ferroelectric polymers with tio2 nanoparticles exhibiting significantly enhanced electrical energy density. *Adv. Mater.* **2009**, *21*, 217-221.

51. Li, J.; Khanchaitit, P.; Han, K.; Wang, Q. New route toward high-energy-density nanocomposites based on chain-end functionalized ferroelectric polymers. *Chem. Mater.* **2010**, *22*, 5350-5357.

52. Cao, W.; Randall, C. A. Grain size and domain size relations in bulk ceramic ferroelectric materials. *J. Phys. Chem. Solids* **1996**, *57*, 1499-1505.

53. Frey, M.; Payne, D. Grain-size effect on structure and phase transformations for barium titanate. *Phys. Rev. B* **1996**, *54*, 3158-3168.

54. Mao, Y. P.; Mao, S. Y.; Ye, Z. G.; Xie, Z. X.; Zheng, L. S. Size-dependences of the dielectric and ferroelectric properties of BaTiO[sub 3]/polyvinylidene fluoride nanocomposites. *J. Appl. Phys.* **2010**, *108*, 014102-014102.

55. Tang, H.; Sodano, H. A. Ultra high energy density nanocomposite capacitors with fast discharge using $Ba_{0.2}Sr_{0.8}TiO_3$ nanowires. *Nano Lett.* **2013**.

56. Tang, H.; Lin, Y.; Sodano, H. A. Enhanced energy storage in nanocomposite capacitors through aligned pzt nanowires by uniaxial strain assembly. *Adv. Energy Mater.* **2012**, *2*, 469-476.

57. Xie, L.; Huang, X.; Huang, Y.; Yang, K.; Jiang, P. Core-shell structured hyperbranched aromatic polyamide/$BaTiO_3$ hybrid filler for poly(vinylidene fluoride-trifluoroethylene-chlorofluoroethylene) nanocomposites with the dielectric constant comparable to that of percolative composites. *ACS Appl. Mater. Interfaces* **2013**.

58. Xie, L.; Huang, X.; Huang, Y.; Yang, K.; Jiang, P. Core@Double-Shell Structured $BaTiO_3$–Polymer Nanocomposites with High Dielectric Constant and Low Dielectric Loss for Energy Storage Application. *J. Phys. Chem. C* **2013**, *117*, 22525-22537.

59. Yu, K.; Niu, Y.; Bai, Y.; Zhou, Y.; Wang, H. Poly(vinylidene fluoride) polymer based nanocomposites with significantly reduced energy loss by filling with core-shell structured BaTiO3/SiO2 nanoparticles. *Appl. Phys. Lett.* **2013**, *102*, 102903-102903-5.

60. Maliakal, A.; Katz, H.; Cotts, P. M.; Subramoney, S.; Mirau, P. Inorganic Oxide Core, Polymer Shell Nanocomposite as a High K Gate Dielectric for Flexible Electronics Applications. *J. Am. Chem. Soc.* **2005**, *127*, 14655-14662.

61. Tchoul, M. N.; Fillery, S. P.; Koerner, H.; Drummy, L. F.; Oyerokun, F. T.; Mirau, P. A.; Durstock, M. F.; Vaia, R. A. Assemblies of Titanium Dioxide-Polystyrene Hybrid Nanoparticles for Dielectric Applications. *Chem. Mater.* **2010**, *22*, 1749-1759.

62. Guo, N.; DiBenedetto, S. A.; Kwon, D.-K.; Wang, L.; Russell, M. T.; Lanagan, M. T.; Facchetti, A.; Marks, T. J. Supported Metallocene Catalysis for In Situ Synthesis of High Energy Density Metal Oxide Nanocomposites. *J. Am. Chem. Soc.* **2007**, *129*, 766-767.

63. Fredin, L. A.; Li, Z.; Ratner, M. A.; Lanagan, M. T.; Marks, T. J. Enhanced Energy Storage and Suppressed Dielectric Loss in Oxide Core-Shell-Polyolefin Nanocomposites by Moderating Internal Surface Area and Increasing Shell Thickness. *Adv. Mater.* **2012**, *24*, 5946-5953.

64. Guo, N.; DiBenedetto, S. A.; Tewari, P.; Lanagan, M. T.; Ratner, M. A.; Marks, T. J. Nanoparticle, Size, Shape, and Interfacial Effects on Leakage Current Density, Permittivity, and Breakdown Strength of Metal Oxide−Polyolefin Nanocomposites: Experiment and Theory. *Chem. Mater.* **2010**, *22*, 1567-1578.

65. Li, Z.; Fredin, L. A.; Tewari, P.; DiBenedetto, S. A.; Lanagan, M. T.; Ratner, M. A.; Marks, T. J. In Situ Catalytic Encapsulation of Core-Shell Nanoparticles Having Variable Shell Thickness: Dielectric and Energy Storage Properties of High-Permittivity Metal Oxide Nanocomposites. *Chem. Mater.* **2010**, *22*, 5154-5164.

66. Jung, H. M.; Kang, J.-H.; Yang, S. Y.; Won, J. C.; Kim, Y. S. Barium Titanate Nanoparticles with Diblock Copolymer Shielding Layers for High-Energy Density Nanocomposites. *Chem. Mater.* **2010**, *22*, 450-456.

67. Xie, L.; Huang, X.; Wu, C.; Jiang, P. Core-shell structured poly(methyl methacrylate)/$BaTiO_3$ nanocomposites prepared by in situ atom transfer radical polymerization: a route to high dielectric constant materials with the inherent low loss of the base polymer. *J. Mater. Chem.* **2011**, *21*, 5897-5906.

68. Balasubramanian, B.; Kraemer, K. L.; Reding, N. A.; Skomski, R.; Ducharme, S.; Sellmyer, D. J. Synthesis of Monodisperse TiO_2−Paraffin Core−Shell Nanoparticles for Improved Dielectric Properties. *ACS Nano* **2010**, *4*, 1893-1900.

69. Tomer, V.; Polizos, G.; Randall, C. A.; Manias, E. Polyethylene nanocomposite dielectrics: Implications of nanofiller orientation on high field properties and energy storage. *J. Appl. Phys.* **2011**, *109*, 074113-074113.

70. Fillery, S. P.; Koerner, H.; Drummy, L.; Dunkerley, E.; Durstock, M. F.; Schmidt, D. F.; Vaia, R. A. Nanolaminates: Increasing Dielectric Breakdown Strength of Composites. *ACS Appl. Mater. Interfaces* **2012**.

71. Dang, Z. M.; Lin, Y. H.; Nan, C. W. Novel Ferroelectric Polymer Composites with High Dielectric Constants. *Adv. Mater.* **2003**, *15*, 1625-1629.

72. Dang, Z. M.; Wang, L.; Yin, Y.; Zhang, Q.; Lei, Q. Q. Giant Dielectric Permittivities in Functionalized Carbon-Nanotube/ Electroactive-Polymer Nanocomposites. *Adv. Mater.* **2007**, *19*, 852-857.

73. Calame, J. P. Simulation of polarization, energy storage, and hysteresis in composite dielectrics containing nonlinear inclusions. *J. Appl. Phys.* **2011**, *110*, 054107-054107.

74. Hench, L. L.; West, J. K. The sol-gel process. *Chem. Rev.* **1990**, *90*, 33-72.

75. Chon, J.; Ye, S.; Cha, K. J.; Lee, S. C.; Koo, Y. S.; Jung, J. H.; Kwon, Y. K. High-k Dielectric Sol−Gel Hybrid Materials Containing Barium Titanate Nanoparticles. *Chem. Mater.* **2010**, *22*, 5445-5452.

76. Maruyama, K.; Chiba, T.; Takamizawa, M. Film capacitor. U.S.Patent 4,843,517, June 27, 1989.

77. Avnir, D. Organic Chemistry within Ceramic Matrixes: Doped Sol-Gel Materials. *Acc. Chem. Res.* **1995**, *28*, 328-334.

78. Naik, R. R.; Tomczak, M. M.; Luckarift, H. R.; Spain, J. C.; Stone, M. O. Entrapment of enzymes and nanoparticles using biomimetically synthesized silica. *Chem. Commun.* **2004**, *15*, 1684

79. Flack, W. W.; Soong, D. S.; Bell, A. T.; Hess, D. W. A mathematical model for spin coating of polymer resists. *J. Appl. Phys.* **1984**, *56*, 1199-1199.

80. Krebs, F. C. Fabrication and processing of polymer solar cells: A review of printing and coating techniques. *Sol. Energy Mater. Sol. Cells* **2009**, *93*, 394-412.

81. Chou, Y. T.; Ko, Y. T.; Yan, M. F. Fluid Flow Model for Ceramic Tape Casting. *J. Am. Ceram. Soc.* **1987**, *70*, C-280-C-282.

82. Watanabe, H.; Kimura, T.; Yamaguchi, T. Particle Orientation During Tape Casting in the Fabrication of Grain-Oriented Bismuth Titanate. *J. Am. Ceram. Soc.* **1989**, *72*, 289-293.

83. Chen, Q.; Wang, Y.; Zhou, X.; Zhang, Q. M.; Zhang, S. High field tunneling as a limiting factor of maximum energy density in dielectric energy storage capacitors. *Appl. Phys. Lett.* **2008**, *92*, 142909-142909-3.

84. *IEEE Standard Definitions of Primary Ferroelectric Terms 180-1986*; IEEE: New York, 1986.

85. Sarjeant, W. J.; Zirnheld, J.; MacDougall, F. W. Capacitors. *IEEE Trans. Plasma Sci.* **1998**, *26*, 1368-1392.

86. Peet, J.; Senatore, M. L.; Heeger, A. J.; Bazan, G. C. The Role of Processing in the Fabrication and Optimization of Plastic Solar Cells. *Adv. Mater.* **2009**, *21*, 1521-1527.

87. Mittal, M.; Niles, R. K.; Furst, E. M. Flow-directed assembly of nanostructured thin films from suspensions of anisotropic titania particles. *Nanoscale* **2010**, *2*, 2237-2243.

88. Bodnarchuk, M. I.; Kovalenko, M. V.; Pichler, S.; Fritz-Popovski, G.; Hesser, G. n.; Heiss, W. Large-Area Ordered Superlattices from Magnetic Wüstite/Cobalt Ferrite Core/Shell Nanocrystals by Doctor Blade Casting. *ACS Nano* **2011**, *4*, 423-431.

89. Gao, W.; Dickinson, L.; Grozinger, C.; Morin, F. G.; Reven, L. Self-Assembled Monolayers of Alkylphosphonic Acids on Metal Oxides. *Langmuir* **1996**, *12*, 6429-6435.

90. Lewis, T. J. Nanometric dielectrics. *IEEE Trans. Dielectr. Electr. Insul.* **1994**, *1*, 812-825.

91. Lewis, T. J. Interfaces: nanometric dielectrics. *J. Phys. D: Appl. Phys.* **2005**, *38*, 202-212.

92. Roy, M.; Nelson, J. K.; MacCrone, R. K.; Schadler, L. S.; Reed, C. W.; Keefe, R.; Zenger, W. Polymer nanocomposite dielectrics - the role of the interface. *IEEE Trans. Dielectr. Electr. Insul.* **2005**, *12*, 629-643.

93. Tanaka, T.; Kozako, M.; Fuse, N.; Ohki, Y. Proposal of a multi-core model for polymer nanocomposite dielectrics. *IEEE Trans. Dielectr. Electr. Insul.* **2005**, *12*, 669-681.

94. Kim, K. M.; Park, N.-G.; Ryu, K. S.; Chang, S. H. Characterization of poly(vinylidenefluoride-co-hexafluoropropylene)-based polymer electrolyte filled with TiO_2 nanoparticles. *Polymer* **2002**, *43*, 3951-3957.

95. Buckley, J.; Cebe, P.; Cherdack, D.; Crawford, J.; Ince, B. S.; Jenkins, M.; Pan, J.; Reveley, M.; Washington, N.; Wolchover, N. Nanocomposites of poly(vinylidene fluoride) with organically modified silicate. *Polymer* **2006**, *47*, 2411-2422.

96. Li, W.; Meng, Q.; Zheng, Y.; Zhang, Z.; Xia, W.; Xu, Z. Electric energy storage properties of poly(vinylidene fluoride). *Appl. Phys. Lett.* **2010**, *96*, 192905.

97. Kitagawa, K.; Sawa, G.; Ieda, M. Observation of Dielectric Breakdown Sites in Polyethylene Thin Film. *Jpn. J. Appl. Phys.* **1980**, *19*, 389-390.

98. Ieda, M. Dielectric Breakdown Process of Polymers. *IEEE Trans. Electr. Insul.* **1980**, *EI-15*, 206-224.

99. Ieda, M. Electrical Conduction and Carrier Traps in Polymeric Materials. *IEEE Trans. Electr. Insul.* **1984**, *EI-19*, 162-178.

100. Tanaka, T. Dielectric nanocomposites with insulating properties. *IEEE Trans. Dielectr. Electr. Insul.* **2005**, *12*, 914-928.

101. Kim, H. K.; Shi, F. G. Thickness dependent dielectric strength of a low-permittivity dielectric film. *IEEE Trans. Dielectr. Electr. Insul.* **2001**, *8*, 248-252.

102. Kim, Y.; Kathaperumal, M.; Smith, O. N. L.; Pan, M.-J.; Cai, Y.; Sandhage, K. H.; Perry, J. W. High-Energy-Density Sol–Gel Thin Film Based on Neat 2-Cyanoethyltrimethoxysilane. *ACS Appl. Mater. Interfaces* **2013**, *5*, 1544-1547.

103. Smith, M. B.; Page, K.; Siegrist, T.; Redmond, P. L.; Walter, E. C.; Seshadri, R.; Brus, L. E.; Steigerwald, M. L. Crystal Structure and the Paraelectric-to-Ferroelectric Phase Transition of Nanoscale BaTiO3. *J. Am. Chem. Soc.* **2008**, *130*, 6955-6963.

104. Choi, K. J. Enhancement of Ferroelectricity in Strained $BaTiO_3$ Thin Films. *Science* **2004**, *306*, 1005-1009.

105. Wright, J. D.; Sommerdijk, N. A. J. M. *Sol-Gel Materials: Chemistry and Applications*. CRC Press: 2000; p 142.

106. Brinker, C. J. Hydrolysis and condensation of silicates: Effects on structure. *J. Non-Cryst. Solids* **1988**, *100*, 31-50.

107. Novak, B. M. Hybrid Nanocomposite Materials—between inorganic glasses and organic polymers. *Adv. Mater.* **1993**, *5*, 422-433.

108. Brinker, C. J.; Sehgal, R.; Hietala, S. L.; Deshpande, R.; Smith, D. M.; Loy, D.; Ashley, C. S. Sol-gel strategies for controlled porosity inorganic materials. *J. Membr. Sci.* **1994**, *94*, 85-102.

109. Brinker, C. J.; Hurd, A. J.; Schunk, P. R.; Frye, G. C.; Ashley, C. S. Review of sol-gel thin film formation. *J. Non-Cryst. Solids* **1992**, *147–148*, 424-436.

110. Nitta, S. V.; Pisupatti, V.; Jain, A.; P. C. Wayner, Jr.; Gill, W. N.; Plawsky, J. L. Surface modified spin-on xerogel films as interlayer dielectrics. *J. Vac. Sci. Technol. B* **1999**, *17*, 205-212.

111. Prakash, S. S.; Brinker, C. J.; Hurd, A. J.; Rao, S. M. Silica aerogel films prepared at ambient pressure by using surface derivatization to induce reversible drying shrinkage. *Nature* **1995**, *374*, 439-443.

112. Socrates, G. *Infrared and raman characteristic group frequencies : tables and charts*. John Wiley & Sons: West Sussex, 2007.

113. Lee, H.; Smith, N. J.; Pantano, C. G.; Furman, E.; Lanagan, M. T. Dielectric Breakdown of Thinned $BaO–Al_2O_3–B_2O_3–SiO_2$ Glass. *J. Am. Ceram. Soc.* **2010**, *93*, 2346-2351.

114. Zhou, H.; Shi, F. G.; Zhao, B. Thickness dependent dielectric breakdown of PECVD low-k carbon doped silicon dioxide dielectric thin films: modeling and experiments. *Microelectronics Journal* **2003**, *34*, 259-264.

115. IEEE Standard Definitions of Primary Ferroelectric Terms 180-1986. IEEE, New York, USA: **1986**.

116. Sodolski, H.; Kozłowski, M. DC conductivity of silica xerogels. *J. Non-Cryst. Solids* **1996**, *194*, 241-255.

117. Simmons, J. G. Generalized Formula for the Electric Tunnel Effect between Similar Electrodes Separated by a Thin Insulating Film. *J. Appl. Phys.* **1963**, *34*, 1793.

118. Zhou, Y.; Fuentes-Hernandez, C.; Shim, J.; Meyer, J.; Giordano, A. J.; Li, H.; Winget, P.; Papadopoulos, T.; Cheun, H.; Kim, J.; Fenoll, M.; Dindar, A.; Haske, W.; Najafabadi, E.; Khan, T. M.; Sojoudi, H.; Barlow, S.; Graham, S.; Brédas, J.-L.; Marder, S. R.; Kahn, A.; Kippelen, B. A Universal Method to Produce Low–Work Function Electrodes for Organic Electronics. *Science* **2012**, *336*, 327-332.

119. Bardeen, J. Surface States and Rectification at a Metal Semi-Conductor Contact. *Phys. Rev.* **1947**, *71*, 717-727.

120. Hwang, D. K.; Fuentes-Hernandez, C.; Kim, J.; Potscavage Jr, W. J.; Kim, S. J.; Kippelen, B. Top-Gate Organic Field-Effect Transistors with High Environmental and Operational Stability. *Adv. Mater.* **2011**, *23*, 1293-1298.

121. Acton, B. O.; Ting, G. G.; Shamberger, P. J.; Ohuchi, F. S.; Ma, H.; Jen, A. K. Y. Dielectric Surface-Controlled Low-Voltage Organic Transistors via *n*-Alkyl Phosphonic Acid Self-Assembled Monolayers on High-*k* Metal Oxide. *ACS Appl. Mater. Interfaces* **2010**, *2*, 511-520.

122. Fontaine, P.; Goguenheim, D.; Deresmes, D.; Vuillaume, D.; Garet, M.; Rondelez, F. Octadecyltrichlorosilane monolayers as ultrathin gate insulating films in metal-insulator-semiconductor devices. *Appl. Phys. Lett.* **1993**, *62*, 2256.

123. Vogelsang, R.; Farr, T.; Frohlich, K. The effect of barriers on electrical tree propagation in composite insulation materials. *IEEE Trans. Dielectr. Electr. Insul.* **2006**, *13*, 373-382.

124. Granstrom, J.; Swensen, J. S.; Moon, J. S.; Rowell, G.; Yuen, J.; Heeger, A. J. Encapsulation of organic light-emitting devices using a perfluorinated polymer. *Appl. Phys. Lett.* **2008**, *93*, 193304-193304-3.

125. Xin, Z.; Qin, C.; Zhang, Q. M.; Shihai, Z. Dielectric behavior of bilayer films of P(VDF-CTFE) and low temperature PECVD fabricated Si3N4. *IEEE Trans. Dielectr. Electr. Insul.* **2011**, *18*, 463-470.

126. Granstrom, J.; Roy, A.; Rowell, G.; Moon, J. S.; Jerkunica, E.; Heeger, A. J. Improvements in barrier performance of perfluorinated polymer films through suppression of instability during film formation. *Thin Solid Films* **2010**, *518*, 3767-3771.

127. Berry, S.; Kedzierski, J.; Abedian, B. Irreversible Electrowetting on Thin Fluoropolymer Films. *Langmuir* **2007**, *23*, 12429-12435.

128. Karasz, F. E. Dielectric Properties of Poly(2, 6-Dimethyl Phenylene Oxide). *J. Appl. Phys.* **1970**, *41*, 4357.

129. Boulas, C.; Davidovits, J.; Rondelez, F.; Vuillaume, D. Suppression of Charge Carrier Tunneling through Organic Self-Assembled Monolayers. *Phys. Rev. Lett.* **1996**, *76*, 4797-4800.

130. Acton, O.; Ting, G.; Ma, H.; Ka, J. W.; Yip, H.-L.; Tucker, N. M.; Jen, A. K. Y. π-σ-Phosphonic Acid Organic Monolayer/Sol-Gel Hafnium Oxide Hybrid Dielectrics for Low-Voltage Organic Transistors. *Adv. Mater.* **2008**, *20*, 3697-3701.